Interaction of iLID Optogenetic Proteins Characterized using 3D Single-Molecule Tracking in Live *E. coli*

Alecia Marie Achimovich
Harrisburg, PA

Biochemistry and Molecular Biology B.S.,
Gettysburg College, 2016

A Dissertation presented to the Graduate Faculty of the University of Virginia in Candidacy for the Degree of Doctor of Philosophy

Interdisciplinary Graduate Program of Biophysics

University of Virginia
August, 2022

Andreas Gahlmann
Robert Nakamoto
Alison Criss
Rebecca Pompano
Lukas Tamm

ACKNOWLEDGEMENTS

What a journey it has been. The culmination of my academic career is 28 years in the making, and it could not have come to pass without the support of many people in my life. The least of which I owe them is my thanks.

In Andreas, I have found a PhD mentor who matches my pace. I have come to admire his willingness to explore new scientific territories, and try new protocols or techniques, though this does not reflect on his attitude towards spicy foods. So, I would like to thank Andreas for taking in a, perhaps over-enthusiastic, student, and allowing her to explore the unseen world with microscopy and join the resolution revolution. He has provided patient support over the years, for which I am very grateful. I wish him all the best as he pursues tenure this coming year.

My committee has provided much needed advice and support throughout my graduate career. I would like to thank them for all of their help, and for their dedication to the pursuit of knowledge and mentorship.

Next, I would like to thank the past lab members on whose shoulders the Gahlmann lab was built. The first postdoctoral scholar to join the lab was Dr. Charles Richardson. Charles is an excellent scientist, mentor, and friend. He was both a driving and grounding force in the lab. I always appreciated the extra time and effort he put into providing support for the graduate students in the lab, including myself. I am very fortunate that our time overlapped within the Gahlmann lab. Thank you, Charles. The first graduate students to join the Gahlmann lab were Drs. Mingxing Zhang, and Julian Rocha. Starting a lab practically from scratch is no easy feat, especially as newly minted graduate students. I

admire your determination and tenacity that guided you during your time in graduate school. I thank both of them for all of their help learning and understanding single-molecule microscopy. Thank you to Mingxing, who provided help many times in managing the microscope, and adapting code to help with my experiments. A big thanks to Julian, whose work laid the foundation for imaging and data analysis that we all use today. The next graduate student that I must thank is Dr. Ting Yan. Ting has grown from a lab mate to a great friend in whom I can confide. Thank you for countless walks and advice, post cards, and art. I greatly enjoy your sarcasm and sassiness, and look forward to it for years to come. Dr. Ji Zhang and I both joined the lab in the 2016 academic year. During our time working together, Ji has shown me a great deal of patience and kindness, especially when training me to operate the lattice light sheet microscope. I have greatly appreciated his willingness to answer my questions and entertain my chattiness from time-to-time.

As I make my way towards my defense, the Gahlmann lab is entering a new era with a second generation of graduate students who I am confident will push the lab to new and exciting ventures. First, I must thank Josh who has been unerringly supportive since he has joined the lab. Not only has he helped me talk through my project, but he has also advocated for me when I had trouble pushing forward. He has also provided some good music recommendations along the way. Yibo joined our lab partway through his first year at UVa, and I could not be more grateful. Since he has joined, Yibo has always been willing to provide a helping hand with statistical or coding questions. I would be hard-pressed to find a more kind and helpful lab mate. Thank you to Eric, who has been supportive of all of my endeavors both inside and outside of the lab. Olivia is a great labmate and conference roommate. She is a master cloner, coder, and confidant with sharp wit and intuition. I am

excited to see her progress, and hope someday it might feel like Thursday, or even Friday. I have also had the opportunity to work with a few undergraduate students. Thank you to Arshiya, Patrick, Alma, and Jacob who kept me grounded. All of these lab members are superstars, and I wish them all the best as they continue on their journeys.

I have found incredible strength in my family of friends outside of the lab. First, an enthusiastic thank you to the community at City Clay, especially Meagan, and Carol. Thanks for being an oasis outside of lab, and a place where failure is routine and expected. Thank you to the LD gang, Katie and Caroline, for always having my back and being excellent hype-women. To my friends from Gettysburg, Katherine and Miranda, I love you both to the moon and back. Thank you for your love and encouragement. Thank you to Dakota and Emily who provide the best support in the form of laughter and great book recommendations. To my grandfather, who has always kindled and fed my curiosity. A huge thank you to my cats Darwin, and Vi who are an incredible source of comfort and joy. “Thank you” cannot fully encompass the gratitude I have for my partner, Mat. He has been with me through the darkest and lightest times over the past 10 years. You make me feel seen and heard, and have helped me to tap into my inner-strength. Plus, you always make sure to point out when the cats are being especially cute, which is beyond helpful.

ABSTRACT

Single-molecule fluorescence microscopy is a powerful tool that can be used to resolve cellular structures with nanometers of resolution. By localizing molecules with high precision over time, protein motion can be measured and used to resolve different diffusive states. Diffusive states are assigned to protein complexes using computational models with significant statistical power, and require biological validation which is often deliberatively perturbative to cellular function. In the work presented in this dissertation, I explore incorporating a non-invasive, transient method for disrupting protein localization and prospective diffusive states. I utilize light-induced dimerization domains to transiently sequester proteins to non-native cellular compartments upon light stimulation. To test the feasibility of this method, I have characterized the optical response of the improved Light Induced Dimerization (iLID) optogenetic system using conventional imaging methods in addition to single-molecule tracking experiments. To carefully examine the iLID system dynamics, I have extended our single-molecule analysis workflow to incorporate trajectory simulations of membrane-associated molecules. Further, I have added a full-trajectory analysis module that identifies changes in diffusion rate to quantify residence times of single-molecules at binding sites, and the kinetics of the interaction. Through these analyses, I have shown that the iLID system can be activated by longer wavelengths that are minimally absorbed in *in vitro* conditions. Further, I have identified transient interactions of the iLID optogenetic proteins that are not detectable in diffraction-limited imaging. This analysis highlights areas for characterization and improvement of the iLID optical response.

Table of Contents

CHAPTER 1: INTRODUCTION

Overview

To begin, I will state a broad and obvious fact: life is complex. Both multicellular and unicellular organisms live due to complex macroscopic processes such as metabolism, and immunity, that are governed by complex biochemical principles such as cellular signaling, and more fundamentally, protein-protein interactions (PPIs). Each process, each interaction is regulated on the cellular level to respond dynamically to the environment: e.g. nutrient availability, and pathogen recognition. Therefore, it is important from a fundamental, basic science perspective to probe mechanisms underlying systems and the key PPIs which guide them. My work presented here brings an important perspective of non-perturbative experimental validation of high-resolution imaging required for probing dynamic complex formation *in vivo*.

1.1 Mapping protein-protein interaction networks

As discussed above, PPIs are fundamental for cellular function. As such, there are many techniques that can be used to identify and characterize potential PPIs. The ideal method is highly specific, probe-free, quantitative, minimally invasive, and has live specimen compatibility with both high spatial and temporal resolution. However, no single method can meet all of these demands. Well-established *in vitro* biochemical and biophysical methods for probing protein interactions, such as co-immunoprecipitation and Western blot detection, are well suited for analyzing high affinity interactions. Transient, low-affinity interactions are often missed when using these methods due to dissociation before detection[1,2]. Alternative methods such as protein NMR, X-ray crystallography, and small angle X-ray scattering (SAXS) utilize purified proteins for characterizing the structure of proteins, and their binding interfaces[3,4]. While offering atomic-level

information, these techniques each come with a set of caveats. Current state-of-the-art protein NMR allows for solution state structural prediction with an upper limit for molecular weight of 100 kDa, while typical experiments are performed on complexes that are less than 35 kDa in molecular weight[5-7]. Alternatively, X-ray crystallography requires extensive optimization of buffer conditions for achieving crystallization. These conditions may preclude or induce non-native interactions[8]. For example, non-neutral pH may create charged patches on protein surfaces. Thus, interactions which are dependent on electrostatics will likely be altered. SAXS allows for structural prediction of protein complex quarternary structure in solution, but interactions mediated by an adaptor protein(s) may not be captured in solutions that do not accurately recapitulate the cellular environment. Isothermal titration calorimetry (ITC) can provide information about the thermodynamics and stoichiometry of a given interaction[9], but similarly requires purified proteins and a buffer system that fall short of environmental replication. In response, developments in cryo-electron tomography (cryo-ET) have allowed for structural imaging *in situ*, with the stipulation that all samples must be fixed using plunge freezing. For example, Park et al. (2018)[10] utilized a mini-cell producing *Salmonella* strain and achieved high resolution imaging of the type III secretion system, which had not been achieved before despite previous attempts. It is important to note that high resolution structural determination requires thousands of subtomograms for averaging, after which it is still possible to miss transient interactions or dynamic structures with fast protein turnover and exchange. Further, the full volume of thick samples cannot be effectively imaged due to extensive scattering. This can be overcome through the use of focused ion beam milling

(FIB) combined with cryo-ET imaging. In FIB-SEM material is milled away, and a "window" is opened for imaging, though ultimately destroys the sample[11-13].

Fluorescence microscopy overcomes many of the aforementioned obstacles, allowing for *in vivo* visualization of fluorescently tagged molecules. Many fluorescence microscopy-based techniques have been developed over the past decades to detect and quantify interactions between biomolecules *in vitro* and *in vivo*. Improvements of fluorescent probes and biomolecular labeling technologies, in conjunction with instrumental improvements have enabled measurements that provide critical insights into cellular organization and the biochemical interactions occurring within them[14]. Spatial co-localization of emitters through multi-color imaging is now widely utilized to gauge whether biomolecules are close enough to interact. The power of such measurements depends critically on the achievable spatial resolution of the instrument used. Diffraction-limited imaging provides a resolution on the order of 200-300 nm, which is much larger than the size of a typical protein (~2 nm) or the size of small protein complexes (~20 nm). Diffraction-limited resolution is thus too low to determine whether two proteins interact directly in a given complex or whether their interaction is mediated by a third protein[15]. Super-resolution microscopy approaches enabling precise single-molecule localization, such as PALM/STORM and MINFLUX, have been successful in addressing this challenge. For example, Symborska et al. determined radial positions of protein subunits of the nuclear pore complex (NPC) with subnanometer precison,[16] and more recently, Ries and co-workers used MINFLUX microscopy to pinpoint the position of subunits within the NPC with single nanometer precision without the need for radial averaging[17]. Single-molecule microscopy techniques overcome the resolution barrier, providing tens of

nanometers of resolution and thus, accurate co-localization analysis of static structures[18-20].

Detecting protein interactions within freely-diffusing complexes cannot be accomplished by fluorescence co-localization, and thus requires different approaches. Live cell analysis of protein oligomerization state is possible using fluorescence microscopy techniques such as Fluorescence recovery after photobleaching (FRAP), and Fluorescence correlation spectroscopy (FCS). These measurements rely on cellular or compartmental measurements of fluorescence intensity, either recovery of fluorescence as with FRAP, or fluctuations over a small imaging volume as with FCS. Thus, these techniques offer ensemble averaged data from which it is difficult to identify transient binding events[21]. Estimation of binding parameters is performed using kinetic model fitting[22]. Alternatively, Forster resonance energy transfer (FRET), measures the efficiency of non-radiative energy transfer from an excited donor fluorophore to an acceptor fluorophore in the ground state, which becomes excited and emits photons. For energy transfer to occur, the donor and acceptor fluorophores must be within a few nanometers of each other and be oriented correctly. Thus, FRET efficiency serves as a measurement of spatial proximity and can be detected between tagged proteins of interest to infer the existence of protein-protein interactions[23,24]. FRET measurements have been extended to Fluorescence Lifetime Imaging Microscopy (FLIM) techniques. Non-radiative energy transfer shortens the lifetime of the donor fluorophore, and, therefore, spatial proximity of fluorophores can be determined. Due to the nature of the measurement, the lifetime signal is fluorophore concentration independent, and there is limited spectral bleed-through from acceptor fluorescence. These features make FLIM particularly advantageous compared to FRET[25].

Despite the nanometer-level distance sensitivity of FRET and FLIM-FRET, the data derived from these measurements are also ensemble-averaged, and cannot efficiently detect transient interactions. The extension of single-molecule microscopy to FRET (smFRET) allows FRET measurements to be made on single proteins, and can be used to detect heterogeneity within a sample. However, this technique requires the studied proteins to be immobile or very slowly diffusing, and thus cannot detect interactions between freely diffusing proteins within the cytosol[25]. For an exhaustive review of protein oligomerization determination using fluorescence techniques in live cells, please refer to the following review[26].

1.2 Single-molecule tracking analysis for protein complex determination

Single-molecule localization microscopy has led to a resolution revolution in optical, fluorescence imaging. Photo-Activation Light Microscopy (PALM) and STochastic Optical Reconstruction Microscopy (STORM) routinely achieve ~10 nm lateral resolution and ~50 nm axial resolution. The ability to precisely localize single proteins has led to more accurate co-localization analysis of static structures, as described in a previous section, in addition to tracking and diffusive analyses. In such analyses, single proteins are imaged over time to measure how quickly they diffuse in a given environment, whether it be in solution or within live cells. Diffusion rate (*D*) in a given medium can be described by the Stokes-Einstein relationship:

$$D = \frac{k_b T}{6\pi\eta \mathrm{R}}$$

Where k_b refers to the Boltzmann constant, T to temperature, η to viscosity of the medium, and R to the hydrodynamic radius of the protein or biomolecule being measured[27,28]. Using

this equation, it is clear that the diffusion rate of the protein is inversely correlated with its size. Thus, it is possible to infer the oligomerization state of a protein by how quickly it diffuses through a given medium. It is important to note that while the Stokes-Einstein equation holds well for globular proteins or protein complexes, further modifications of the equation are necessary for non-globular protein complexes like microtubule or actin filamentous fibers[29].

Diffusion measurements are made *in vivo* by localizing single fluorescently labeled proteins and following their movement over time. The amount of distance that a molecule moves between each time point, called the displacement (r) of the molecule, is used in subsequent analyses. Just by calculating the mean squared displacement (MSD or $<r^2>$) over increasing time intervals (τ), one can get significant information about their system[30]. A molecule with true random diffusion, also called Brownian diffusion, exhibits a linear MSD over time ($<r^2> \propto D\tau$) for the full length of the molecule's trajectory. On the other hand, a molecule that is not a true Brownian diffuser will exhibit a different relationship where ($<r^2> \propto \tau^{\alpha}$). When α is greater than one, it suggests that the molecule is moving more quickly than expected for a Brownian diffuser, and exhibits super-diffusive behavior. This is a common feature of proteins that are associated with vesicular transport, for example[31]. When α is less than one, it suggests that the molecule is moving more slowly or not as far as expected for a Brownian diffuser, and is likely confined in space. This is most common for *in vivo* measurements where there are many levels of confinement. Membranes serve as physical boundaries which confine molecules to subcellular compartments, resulting in sub-diffusive behavior. Indeed, recent diffusion measurements in bacteria support that confinement contributes to subdiffusive behavior of proteins, estimating the alpha

exponent is between 0.6 and 0.8.[32-34] Further, the cytosol of the cell is very crowded, containing a myriad of biomolecules which may serve as a barrier to random diffusion, especially for large molecules. In this way the cytosol can act as a sieve. This is particularly true for bacterial cells where the nucleoid displaces large proteins to the cell pole as they cannot diffuse freely through the dense DNA-protein meshwork[35-37].

Anomalous diffusion within the cytosol precludes facile analysis of diffusion measurements. This is particularly true within the extremely confined space of a bacterial cell. The volume of an average *E. coli* cell is approximately 8 μm^3. This leads to interesting questions about how bacterial cells are able to differentially regulate reactions without the high degree of compartmentalization that is apparent in eukaryotic cells[35]. Many labs within the microbiological imaging realm are working on understanding protein-protein interactions within bacteria, and how these interactions contribute to macromolecular assembly within the cytosol. With each lab comes a slightly different single-molecule imaging set-up, and another data analysis pipeline to accompany it[38]. Here, I will outline a few of the predominate features that are pervasive in the field.

1.2.1 Diffusive state assignments to protein complex populations

After image analysis and identification of single molecules and their trajectories, the data output is a distribution of apparent diffusion coefficients. Using these distributions, further analyses are performed to distinguish protein complexes and modes of binding that molecules existed in during the time of measurement. These so-called "state-fitting models" are used to assign diffusive states (quantitatively, Diffusion Coefficient = x $\mu m^2/s$) to protein complexes (DNA-bound, e.g.). A common method for estimating the diffusion

coefficient, which describes a given state, is by fitting the experimental distribution to an analytical equation that describes the probability or likelihood of observing the experimental distribution if the molecule exists within said diffusive state. Curves generated from the analytical equation are then fit to the experimental distribution, and evaluated using statistical analyses such as linear least squares and maximum likelihood estimation (MLE). To describe more complex, multi-state systems, the probability function can be expanded to include more diffusive states, at varying fractions of the population as a linear combination of terms. This method has been modified and used extensively both in bacteria and eukaryotic cells[39-44].

Other methods utilize Hidden Markov Models (HMM) which describe not only the diffusive states that protein exists in, but also the kinetics of switching between multiple diffusive states[45,46]. It is important to note that the methods which utilize HMM fitting, as well as analytical equation fitting as described above, invoke a fixed number of states. The analyses can be performed multiple times to find the best number of states to include in the model. However, this leads to an issue which is inherent to parameter fitting. Using more parameters in a model equation will lead to better fits, especially for complex curves. This can lead to over-fitting of your experimental data, where each added state marginally decreases the error of the fit, though there may be no biological significance of the added states[47]. To incorporate model flexibility and remove bias, Persson et al.[48] applied variational Bayesian statistics to their HMM modeling of diffusive state and kinetic parameter selection, which objectively weighs the goodness of fit of the model against the complexity of the fit.

Another feature of the abovementioned fitting methods is that they do not address levels of complexity that exist from the cells themselves. As mentioned previously, both the cell membrane and cytosol are extremely crowded and impose barriers for diffusing molecules, resulting in anomalous diffusive behavior. This effect is exacerbated within the small volume of the bacterial cell. Therefore, some groups have focused on directly incorporating considerations for cell geometry and confinement imposed by membranes in the diffusion state fitting models. This has been achieved by direct simulation of single-molecule trajectories within confined volumes that reflect the cell geometry of bacterial cells. In this way, the experimentally derived "apparent" diffusion coefficient (D^*) distributions, are fit with simulated diffusion coefficient distributions to derive the theoretical, unconfined diffusion coefficient (D) state[49-53].

To ensure the accuracy of state-fitting models, extensive statistical validation is required. The gold standard for validation and reproducibility is using simulated data as a benchmark for model accuracy and applicability. However, experimental validation of assigned states is a non-trivial task. Mutation or deletion of putative interacting partners is the most often utilized control. This is not possible for proteins which are required for maintaining cell viability including cell wall synthesis and DNA replicating factors. Therefore, there is a need for assays that transiently disrupt protein interactions, do not reduce cell viability, and can be easily incorporated into single-molecule tracking experiments. An attractive solution is optogenetics, which can transiently perturb spatial localization of proteins using a light signal. The technology will be discussed hence.

1.3 Optogenetics

Optogenetics is a broad term that is applied widely to describe light-induced cellular reactions. Since the first implementation of optogenetics just under 20 years ago, synthetic biologists have developed a large array of tools to control or engineer cellular functions by utilizing proteins which contain light-sensing domains. By heterologously expressing light sensing domains in non-native contexts, new or manipulated functionalities can be introduced to previously "blind" systems. Moreover, light-driven responses are transient and allow for temporary manipulation of the cellular environment. The following sections will describe different form factors that optogenetic systems often take and a brief overview of how they have been applied. **Overview of photoreceptors**

Photoreceptors are classified as any protein that integrates a light input to a signaling response. There are six type types of photosensory proteins which have been well-characterized including: rhodopsins[54], phytochromes[55], cryptochromes[56], blue-light using flavin (BLUF) proteins[57], photoactive yellow proteins (PYPs), and light oxygen voltage (LOV) proteins[58,59]. It is important to note that this is not an all-inclusive list, as there are photoreceptors that have been discovered recently, such as CarH in myxobacteria which regulates carotenoid biosynthesis[60], that have not been extensively characterized. Despite the breadth in sequence and structure of these photoreceptors, there are apparent emergent properties in their mechanisms of action. Firstly, each protein module utilizes a chromophore which absorbs photons and converts the light signal to some physical change in the protein. There are four chromophores utilized by photoreceptors including, retinal (rhodopsins), bilin (phytochromes), p-coumaric acid (photoactivated yellow proteins), and

flavin (cryptochromes, BLUF proteins, and LOV proteins)[61] which all are characterized by extended conjugated pi-orbitals.

The mechanism of signal transfer is dependent on the conjugated chromophore, but the outcome is typically proton transfer to the protein, which results in a conformational change, and subsequent signal activation[62]. The following sections will discuss the ways in which these photoreceptors have been used to manipulate cell biology using light signals.

1.3.2 Ion channels and transporters

Light-regulated ion transporters were among the first optogenetic tools developed. These transporters largely consist of a family of proteins called rhodopsins which utilize a retinal chromophore[54]. Retinal is covalently bound to the rhodopsin protein and undergoes isomerization after light absorption. For animal rhodopsins (type II), isomerization of retinal initiates signaling pathways via activation of signaling enzymes, serving as photo-activated G-protein coupled receptors[63]. Alternatively, bacterial rhodopsins (type I) change conformation due to isomerization of retinal, resulting in pore opening and pumping, or passive diffusion of ions through the transporter pore[64]. Ion-transporting rhodopsins are classified as light-gated channels (also referred to as channel rhodopsins), including both cation and anion channels, or light-driven pumps, including sodium, chloride, and proton pumps. These varieties of ion-transporters have been extensively utilized to selectively hyper- and de-polarize membranes, especially in neuroscience[65-67] and cardiology fields[68,69].

1.3.3 Opsin-independent photoreceptors

Non-rhodopsin photosensory proteins have been used to modulate a broad variety of cellular processes by acting as optogenetic switches. This has been possible due to the modular nature of light sensing domains which can be used to label proteins of interest much like an affinity or fluorescent tag. Despite the diversity in available switches, they operate similarly. Much like rhodopsin photoreceptors, non-opsin photoreceptors utilize a chromophore (e.g. flavin, bilin, or p-coumaric acid) which undergo some conformational change due to wavelength-dependent photon absorption as described in a previous subsection. These conformational changes lead to: 1) change in the oligomerization state of the protein through dissociation or association of homo- or hetero- oligomers, or 2) uncaging of a small peptide for targeting to different cell compartments or binding a known interaction partner **(Figure 1.1)**[70]. By tagging proteins of interest with light sensing domains, one can control both protein localization and oligomerization-dependent activity state of enzymes. Thus, by modifying signaling molecules with optogenetic switches, unprecedented spatio-temporal control of signaling can be achieved by integrating light- rather than chemical- signals[70,71].

Because of the modularity of optogenetic switches, they have been used to attenuate the activity of a wide variety of processes including, but not limited to, directed lamellar, membrane ruffling of cultured epithelial cells[72], secretion of virulence factors by bacteria[73], and tyrosine kinase signaling for high-throughput identification of small-molecule inhibitors[74].

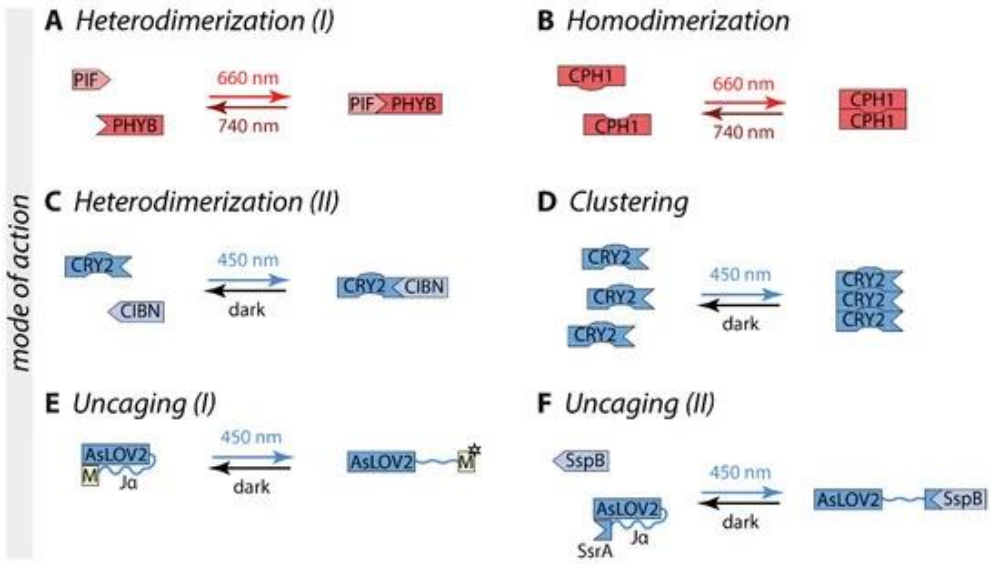

Figure 1.1. Action mechanism of optogenetic switches with examples. There are many other examples of switches which utilize these modes of action. For an exhaustive discussion of optogenetic switches and their modifications for increasing efficiency and usability, please refer to Khamo et al. (2017)[75]. Figure reproduced from Kramer et al. (2021)[70].

1.4 Optogenetic knocksideways assays for validating single-molecule state assignments

An overview of statistical methods used to resolve different diffusive states and assign them to protein complexes was outlined in detail in section 1.3. A clear method for verifying different diffusive state assignments to protein complexes has yet to be developed. We propose to disrupt the spatial distribution of proteins to non-native cellular compartments, using transient, non-invasive and reversible light signals[76]. We refer to this method as a "knocksideways" assay for the remainder of the dissertation. In this assay, cytosolic proteins are tagged with an optogenetic dimerization partner while the dimer

complement is targeted to a non-native cellular compartment (e.g. the cell membrane). Optical activation of dimerization results in sequestration of proteins of interest to the non-native cellular compartment, and interacting proteins can be sequestered to the same compartment as a result. We hypothesize that changing the spatial distribution of interacting proteins will aid in the assignment of diffusive states to protein complexes with distinct compositions. In the simplest scenario, we expect to observe depletion of the cytosolic diffusive state assigned to the suspected oligomer when either interacting partner is sequestered to the membrane. Here, we test the possibility of combining optogenetic manipulation with 3D single-molecule tracking microscopy in live *Escherichia coli*. The improved Light Induced Dimerization (iLID) system[77] was selected because it has been extensively characterized and engineered for optimized performance in different model systems. Thus, a considerably large toolbox of iLID variants with different affinities, and reversion times are available for implementation[73,77,78]. The iLID protein contains the light-sensing light oxygen voltage (LOV2) domain derived from *Avena sativa* which incorporates a flavin cofactor during folding. The flavin cofactor acts as a chromophore, and forms a cysteine adduct with the LOV2 domain after illumination with blue light. As a result, the iLID protein changes conformation and exposes a binding site for the interacting partner, SspB[79,80].

1.5 Overview of dissertation

In the remainder of the dissertation, I will discuss my efforts to use the improved light induced dimerization (iLID) optogenetics system in single-molecule tracking experiments. In Chapter 2, I will discuss single-molecule microscopy, the instrument used, and the modifications that were made to acquire measurements for optogenetic

experiments. Next, I will discuss the experimental and computational methods employed to acquire and analyze the data in Chapter 3. This chapter will highlight where I have extended our computational toolbox to include simulation models for membrane diffusion. Further, I have introduced an intuitive analysis pipeline which utilizes full trajectory information that would be discarded as part of our traditional diffusion analysis. Chapter 4 will contain discussion of the results of my work. In this chapter, you will find important considerations about how optogenetic tools should be calibrated and applied to any imaging experiment. Further, I make suggestions for additional characterization of the light oxygen voltage (LOV2) domain and the iLID protein itself. Lastly, in chapter 5, I discuss the trajectory of work to be done in light of my analyses. This includes using far-red laser excitation to decrease pre-activation of the optogenetic system, incorporating membrane diffusion into our existing diffusion coefficient model, and using full-trajectory analyses to derive kinetic information about protein interactions.

CHAPTER 2:

FLUORESCENCE IMAGING

As described in the previous chapter, the vision of this work is to use the iLID optogenetic system to transiently deplete cytosolic diffusive states through spatial redistribution of proteins to non-native cellular compartments. Before knocksideways experiments could be designed, it was necessary to first evaluate the iLID optogenetic response in the live *E.coli* model system. Optogenetic tools, including iLID, have been widely applied in eukaryotic cells in conjunction with diffraction-limited fluorescence microscopy to obtain population-averaged, phenotypic readouts[70,81]. Therefore, I sought to use both conventional diffraction-limited conditions and single-molecule localization and tracking microscopy to quantify the iLID optogenetic response. In this chapter, I will discuss the imaging techniques used with an emphasis on experimental design considerations required for live-cell single-molecule fluorescence microscopy.

2.1 Single-molecule fluorescence imaging

Fluorescence microscopy allows for imaging of cellular structures in native contexts. Conventional imaging techniques, however, are limited by their ability to resolve structures that are close in space. Each fluorescent molecule emits photons of light that can be described by a wavelength within the visible range (380 nm – 700 nm) which are collected using a detector. Due to light diffraction, the fluorescence distribution is described by a point spread function (PSF) which appears as an airy disk (**Figure 2.1**). Because each emitter can be described by a PSF, emitters which are close in space will produce an image with overlapping PSFs (**Figure 2.2**). Thus, there is an inherent physical limit to how close emitters can be in space and still be resolved. This was first described by Ernst Abbe according to the following equation[82]:

$$d_{x,y} = \frac{\lambda}{2 \cdot n \cdot \sin\theta}$$

where the lateral diffraction limit ($d_{x,y}$) is limited by the wavelength (λ) of light collected, as well as the inherent imaging conditions such as the refractive index of the imaging medium (n), and maximum angle of light (θ) collected by the objective lens. The imaging parameters can be combined into a single term called the numerical aperture (NA):

$$NA = n \cdot \sin\theta$$

Such that the diffraction limit can be simplified to:

$$d_{x,y} = \frac{\lambda}{2 \cdot NA}$$

This relationship describes the achievable lateral resolution for a fluorescent emitter. Resolving emitters axially is even more difficult, as the achievable resolution shows an even greater dependence on the amount of light collected by the objective lens as described by[83]:

$$d_z = \frac{\lambda}{n \cdot (\sin\theta)^2}$$

Therefore, the distance between two objects required to resolve them is approximately half the wavelength of visible light (~200 nm), depending on the objective lens used in the microscope. That means that small biomolecules, which are on the order of a few nanometers in size, cannot be resolved within larger complexes. For example, fluorescently tagged subunits making up the nucleoporin complex form a continuous ring of fluorescence

which cannot be resolved into individual components without further manipulation (**Figure 2.2**).

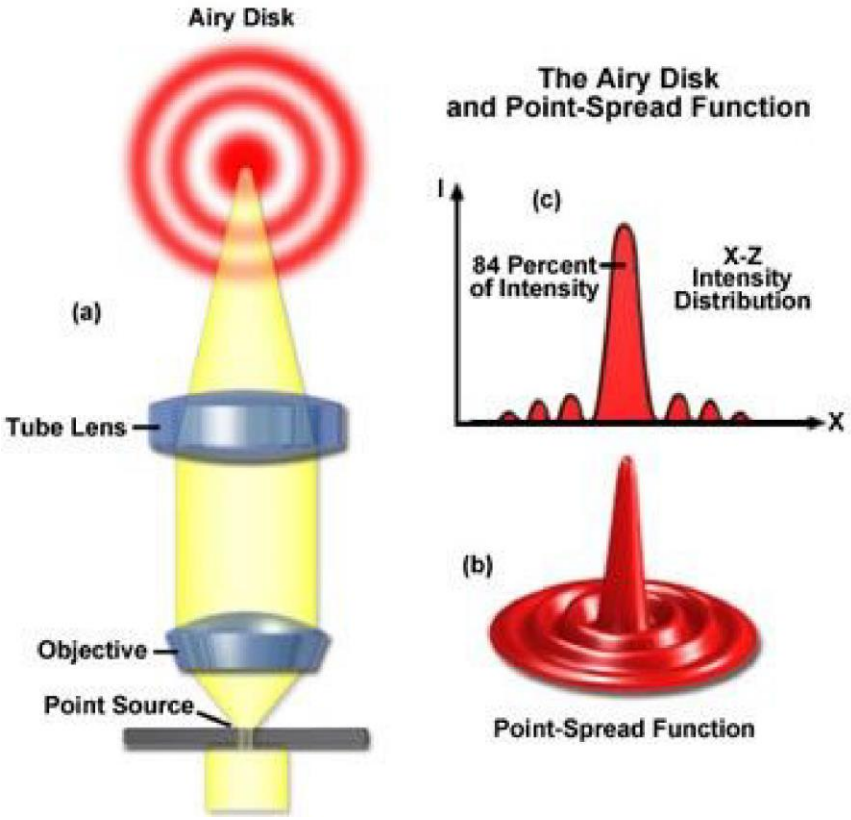

Figure 2.1. Airy disk point spread function. (a) Photons emitted from a point source are collected with the microscope objective, and propagate through the imaging system. When focused, photons will form an airy disk pattern due to diffraction of the light waves. An axial (x-z) cross-section of the airy disk pattern indicates that the central lobe of the disk contains approximately 84% of the observed intensity which is equally apparent in (b) a 3D representation of the point spread function collected. Figure reproduced from ref.[84]

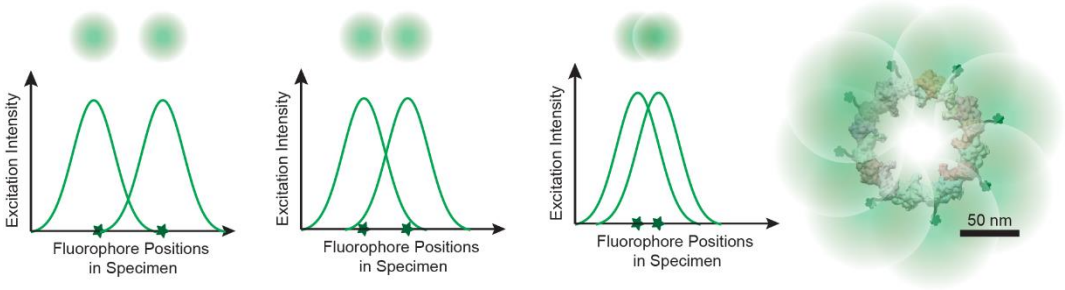

Figure 2.2. Overlapping point spread functions. PSFs approximated as smoothed Gaussian functions as detected on a camera (top) and as intensity cross-sections (bottom) become unresolvable as the distance between emitters is decreased (left to right). For example, fluorescently labeled subunits within a nucleoporin complex cannot be resolved from each other and will resemble a continuous ring, due to the diffraction limit. Figure adapted from reference[14].

It is thus necessary to manipulate imaging conditions to resolve biomolecules that are close in space. This can be achieved by controlling the emission of fluorophores for separated collection of fluorescence. The development of imaging techniques to address this issue was a significant advancement in the field, and resulted in the Nobel prize awards for the scientists that pioneered super-resolution microscopy. The three main fields of super-resolution microscopy include Stimulated Emission Depletion (STED) microscopy[85], Structured Illumination microscopy (SIM)[86], and Single-Molecule Localization Microscopy (SMLM)[87]. STED utilizes patterned light to deplete fluorescence in a region surrounding a narrow fluorescence excitation beam to spatially separate fluorescence of molecules[85]. SIM also utilizes patterned light to achieve super-resolution. Light diffraction from interference of incident light waves form predictable light patterns, called optical lattices, are used to image samples, offering higher spatial frequency

information than traditional imaging methods. Thereby, super-resolution images can be reconstruction from image data. Alternatively, SMLM achieves super-resolution by controlling emitter concentration at any given time, such that spatially separated single-molecules can be imaged. SMLM can be achieved through a variety of methods such as photoactivated light microscopy (PALM), stochastic optical reconstruction microscopy (STORM), and point accumulation in nanoscale topography (PAINT). Each of these methods rely on the fluorophore transitions between fluorescent ON and OFF states. Spatially separated PSFs are fit with a Gaussian function that describes the fluorescence profile. Super-resolution images are then rendered by adding all of the fit localizations with tens of nanometers of precision. (**Figure 2.3**).

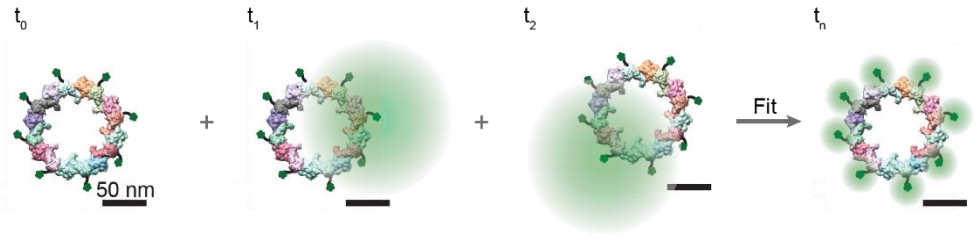

Figure 2.3. Single-molecule localization microscopy image rendering. To illustrate image reconstruction in SMLM, a representation of a nucleoporin complex which has been densely labeled with fluorophores is used. Single fluorophores stochastically enter the fluorescence ON state at a given time, *t*. A Gaussian fitting model is applied to each image to identify single-molecule emitters, achieving tens of nanometers of resolution, laterally. Fit images over the collection time, t_n, are integrated to produce a super-resolution image. Figure adapted from reference.[14]

In PALM, a small subset of fluorophores is primed for excitation using low intensities of UV light, and then excited into the fluorescent ON state with light at longer

wavelengths. Unprimed, unexcited fluorophores remain in the fluorescent OFF state[88]. STORM is achieved using synthetic dyes which stochastically switch between the ON and OFF state in suitable buffer conditions[89-92]. Unlike PALM and STORM, PAINT does not rely on the photophysics of the fluorophore for switching between fluorescent states, but rather depends on fluorophore binding to static structures[93]. Quickly diffusing, unbound molecules escape detection until bound to the labeled structure. Bound molecules are recycled back into the cytosol or medium and remain "invisible" until binding occurs again. The most common implementation of this technique is in the form of DNA-PAINT which utilizes specific DNA nucleotide tags as scaffolds for fluorophore binding[94].

2.2 Measuring the depth of an emitter

Conventional PSFs offer information about the lateral (*x*- and *y*-) positions of fluorophores. To attain three dimensional images of structures, axial information is required. Many techniques have been developed to squeeze more information out of fluorescence PSFs including the use of multiplane imaging, interferometric measurements, and PSF engineering[95]. The simplest form of multiplane imaging is biplane imaging in which emission light is split into two channels, and is collected by two cameras that are slightly offset by a known distance to different image planes. Thus, an emitter will always be out of focus on at least one of the cameras. The ratio of PSF size between the two cameras monotonically increases as a function of the PSF axial position. Thus, by simultaneously imaging on both cameras, it is possible to determine the depth of the emitter[96]. This method can resolve up to 1 μm of axial distance, and is fundamentally limited in localization precision by splitting photons between to detectors. Interferometric methods do not suffer from this same issue. Multiple objectives are used to collect emission

light from the sample into different channels which are recombined to induce diffraction. Position-dependent phase information can be used to extract axial information with sub-micron resolution range[97].

Point spread function engineering also takes many forms such as self-bending PSFs (sbPSF)[98], astigmatism[99], and double-helix point spread function (DHPSF)[100]. In each case, the shape or relative position of shapes within the PSF is dependent upon the axial position of the molecule. Thus, the axial position of the emitter can be determined by fitting the PSF shape. Our lab employs the DHPSF method to achieve 3D imaging because it offers sufficient depth information of 1.5 μm - 2 μm to image entire bacterial cells[49,50,101-103], and it is easy to implement physically in the microscope and computationally in to fitting models. The DHPSF is created by inserting a phase mask into the emission path of the microscope that modulates the phase of light to split the traditional PSF into two lobes. The lobes of the PSF are vertically stacked when in focus, and rotate around a central position when the emitter moves out of focus. The position of an emitter can be determined by using a double Gaussian fitting model which uses the relative position of the two lobes to determine the lateral and axial position of the emitter.

2.3 Experimental design: choosing the right fluorophore

Single-molecule localization microscopy relies on stochastic transitions of molecules between fluorescent ON and OFF states. There is a large variety of fluorophores in the form of dyes and fluorescent proteins which can accomplish this task, and choosing one that fits your experiment can be daunting. Selectivity of labeling, label size, brightness, and photostability are all important factors which are often at odds with each other.

The precision of any single-molecule fluorescence measurement is directly dependent on the number of photons collected for the measured PSF. This relationship is described by the equation[104]:

$$\sigma = \frac{s}{\sqrt{N}}$$

Where σ is the lateral localization precision, *s* is the standard deviation of the 2D intensity profile fit with a Gaussian function, and *N* is the number of photons collected from the emitter. Therefore, the brightness of the fluorophore directly impacts the precision of measurement, and the achievable resolution. The reported quantum yield (Φ), the number of photons emitted per photon absorbed, can be used as a direct measure of fluorophore brightness. Fluorescent dyes typically outperform fluorescent proteins in terms of brightness. Further, dyes remain fluorescent for longer, exhibiting superior photostability[105]. Despite the excellent photophysical qualities of fluorescent dyes, there are major drawbacks to consider. For live cell imaging, the dye must be membrane-permeable to achieve cytosolic protein labeling. Further, rigorous washing of the sample is required to ensure all unbound dye is removed for high specificity in labeling.

Fluorescent proteins, on the other hand, are genetically encodable, and offer unprecedented labeling specificity. Therefore, a considerable amount of work has been done to optimize fluorescent protein photophysical properties, and expand the toolbox of utilities available. Local concentration of fluorescent proteins through the use of Sun tags is a viable option for amplifying the signal of fluorescent proteins[106]. However, the molecular weight of a single fluorescent protein is ~30 kDa, comprising a bulky label that could interfere with the functionality of the tagged protein. The Sun tag increases the size

of the label with each fluorescent protein that binds to it. Therefore, it works best when tracking large structures, such as vesicles, to ensure that it does not alter the properties of the tagged molecule. Further, it is important to establish functionality of the system before proceeding to further imaging experiments with the tagged protein. Fluorescent dyes are considerably smaller in size, typically less than 1 kDa, but require site specific labeling tags. For example, the Halo tag[107], which are routinely used for genetically tagging proteins of interest for site-specific labeling with ligand-based dyes, is 33 kDa and comparable in size to fluorescent proteins. Thus, there is more work to be done to increase the brightness of fluorophores while enhancing live-cell compatibility.

Labeling using unnatural amino acids (UAA) offers a promising new alternative. Labeled unnatural amino acids are supplied to the growth medium, and are specifically incorporated into a protein at "recoded" stop codons[108-111]. This decreases the label size to a single dye-labeled amino acid. However, implementation of this technology requires a lot of manipulation of the model system, and includes many components for which extensive optimization is required. This includes genetic encoding of tRNAs with complementarity to the recoded stop codon, and aminoacyl tRNA synthetases to load the tRNA with the unnatural amino acid. Further, conditions must be optimized for labeling efficiency, uptake, and incorporation of UAAs.

It is also possible that the system being studied will restrict the fluorophores available for use. For example, I characterize the diffusive behavior of the iLID optogenetic system in Chapter 4. The iLID protein contains a light oxygen voltage (LOV2) domain which absorbs light at wavelengths less than 500 nm, resulting in conformational changes and activation of the optogenetic system[80,112,113]. To track the cytosolic binding partner of

iLID in non-activated conditions, it is required that the fluorescent tag is excited at wavelengths greater than the reported absorption value. To determine the sensitivity of the iLID system to different wavelengths of light, I used low intensity laser illumination at 405 nm, 488nm, and 561 nm. In all illumination conditions, with the exception of 561 nm light, I found that the iLID system was activated to some degree. Therefore, I was restricted to using a spontaneously blinking fluorophore which could be excited at 561 nm. There are not any known fluorescent proteins which exhibit this behavior, all requiring priming with 405 nm light for photoactivation, thus restricting labels to fluorescent dyes[105]. Similar considerations are required when designing multi-color labeled experiments. Excitation and emission spectra of each fluorophore must show minimal overlap with each other to ensure that fluorescence is excited and collected with high specificity[114,115].

2.4 Instrumentation

The work presented here was performed on a custom-built inverted fluorescence microscope in both diffraction-limited and 3D single-molecule modes. The microscope has been described in detail previously[49,50,116]. A major advantage of customizable instruments is the ability to modulate the instrument based on the needs of the experiment. This is highlighted by the modifications made here for application to optogenetic experiments.

2.4.1 Fluorescence imaging

The light used to excite fluorescence within a biological sample exhibits an absorption spectrum which is blue-shifted to shorter wavelengths compared to the light emitted by the sample. The difference in absorption and emission maxima is called the Stokes shift. Therefore, different optical elements are required for channeling each type of

light, and the microscope layout (**Figure 2.4**) will be discussed in terms of its excitation and emission pathways.

The excitation pathway is the same in structure as described previously[49,50,103]. An additional 488 nm laser (Genesis, MX488-1000 STM) line was launched from a fiber optic cable (PM-S405-XP, ThorLabs), in parallel to the other excitation lasers including 405 nm (Coherent OBIS 405), 514 nm (Coherent Genesis MX514 MTM), and 561 nm (Coherent Genesis MX561 MTM) emitting lasers. The configuration of the microscope has been constructed to support excitation and photoactivation of fluorophores utilized in single-molecule microscopy where 405 nm laser light is used to photo-activate fluorophores such as PAmCherry, 514 nm and 561 laser light excites fluoresce of commonly used blinking fluorophores such as eYFP and Janelia Fluor 549, respectively. Lastly, the 488 nm laser line was implemented to extend the compatibility of the microscope to activate optogenetic systems. While we specifically used the iLID system, the 488 nm activation is compatible with any blue-light absorbing light-sensing domain with an absorption maxima near this value[117]. Each laser is first expanded to create a collimated beam with a larger size than the input beam by two lenses. Then the excitation beam passes through a zero order quarter wave plate to circularly polarize the laser. In 514 nm laser excitation pathway, there is a band-pass filter (Chroma ET510/10bp) to limit the wavelength range in the pathway. After initial collimation of the 488 nm beam, a mirror redirects the beam into the 514 nm pathway, and utilizes the same optic elements. All three laser lines (with 514 nm, and 488 nm together) are combined by using a set of dichroic mirrors (Chroma T470lpxr and Chroma T525lpxr) and reflecting mirrors. The shared pathway is directed to another dichroic mirror passing into the inverted microscopy objective lens (UPLSAPO 60X

1.4NA). For experiments which require 514 nm excitation, the dichroic mirror (Chroma ZT405-440/514/561rpc-UF1) filters out wavelengths of light between 440 nm and 514 nm. Thus, for optogenetics experiments, the dichroic mirror was replaced with another which would not filter out 488 nm activation laser light (Chroma zt440/488/561rpc). It is not possible to perform experiments in which both 488 nm and 514 nm light are required for excitation purposes using this set up. The objective lens projects collimated laser beams onto the sample, which enables wide-field illumination. The sample is mounted on an xyz nano-positioning stage (Mad City Labs), which provides positioning and stability with nanometer precision. Immersion oil is placed on the objective lens, and the glass coverslip (#1.5, 22 mm x 22 mm, VWR) mounted sample is placed on the sample stage, in close proximity to the objective. Fluorophores within the sample are excited using the collimated laser beams. Emitted light is captured by the same objective lens and transmitted into the emission pathway.

Emitted fluorescence collected by the objective lens is first reflected by the dichroic mirror used for transmitting excitation beams into the laser (Chroma ZT405-440/514/561rpc-UF1 for 514 nm light excitation, and Chroma zt440/488/561rpc for 488 nm light excitation). The emission light is then passed through a series of filters to remove scattered excitation light from the emission pathway (514 nm long pass filter: Semrock LP02-514RU-25, and 561 nm notch filter: Semrock NF03-561E-25), as well as a 700 nm short-pass filter (Chroma ET700SP-2P8) to limit the amount of light outside of the emission wavelength range passing through to the detector. The objective lens used in the microscope is infinity corrected, meaning that the focal plane is infinitely far from the lens. To capture the image plane, a tube lens is used to collect and transmit emission light. After this stage, a flip

mirror is in place to allow for reflection of the signal into the phase contrast pathway (described in the next section) if in the “up” position. If the flip mirror is in the “down” position, the emission light will bypass the mirror and is separated depending on the wavelength of emitted light using a dichroic mirror (Chroma T560lpxr-uf3) into “red” and “green” channels. In both channels, emitted light is then passed into two lenses in a 4f configuration. These lenses are doublet achromatic lenses, and thus limit the effects of spherical and chromatic aberrations. For single-molecule imaging experiments, a double helix phase mask (Double Helix LLC) is placed in the Fourier plane between the lenses in the 4f system to apply the DHPSF transfer function in frequency space. The second 4f lens converts the light back to a real image which is then collected and visualized by an sCMOS camera (Hamamatsu ORCA-Flash 4.0 V2). Emitters will exhibit the DHPSF in this configuration.

In the single-molecule configuration, fluorophores must be excited with high intensity laser light to 1) ensure that most fluorophores are bleached, and each cell contains a low concentration of emitting fluorophores at the time of image acquisition and 2) produce the stochastic blinking events required for imaging molecules over time. To produce this effect, excitation lasers are focused to a small area (~0.25 cm^2) to produce laser intensities of ~1-3 kW/cm^2. For imaging optogenetic systems, it was important that the same fluorescence excited molecules were activated by 488 nm light. Thus excitation (561 nm) and activation (488 nm) beams were aligned to the same region.

Diffraction-limited imaging was performed by removing the DHPSF phase masks from the emission pathway, keeping all other components constant. Additionally, laser power is three orders of magnitude lower (~ 1 W/ cm^2) to reduce photobleaching. This is necessary for acquiring images in which most molecules are fluorescent and contributing to image formation.

2.4.2 Phase contrast imaging

Phase contrast imaging enables visualization of whole cell morphology. This step is important for determining the cell position for fluorescence data registration and filtering, as well as morphological detection of sick cells for exclusion in further analyses. Phase contrast imaging is possible due to the inherent scattering properties of the densely packed bacterial cell cytosol, and is particularly advantageous because it does not require further labeling. Optical elements are used to enhance the scattering of light, and produce high contrast images from which cells are clearly visible.

Light from a red light-emitting-diode (LED) which is positioned above the sample stage and objective lens on an illumination tower, is passed through an annulus to form a ring of light. A condenser lens focuses the ring of light on the sample. Light that is scattered by cellular contents is typically phase shifted by -90° while transmitted light will remain unaffected. Light is then collected by the objective lens, and passes through the same optics as emission fluorescence, including the dichroic mirror and tube lens. A flip mirror in the emission path reflects the light into a separate phase contrast channel, as described in the previous section. The light then passes through a 4f lens system where a phase ring is placed in the Fourier plane. The phase ring shifts the phase of the transmitted light by +90°. In this way, light which did not pass through cells will be a total of 180° phase shifted with respect to light that was scattered. Thus, scattered light and transmitted light will destructively interfere to effectively enhance the contrast between cells and the transparent mounting substrates which is visualized on a detection camera (Aptina MT9P031).

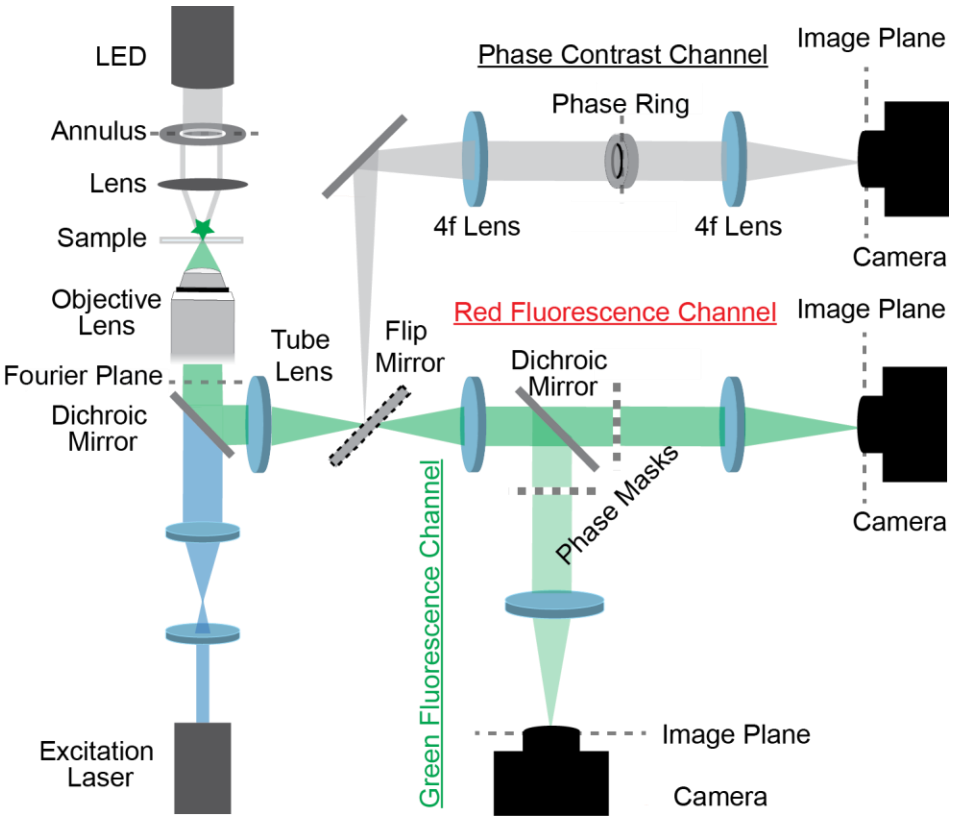

Figure 2.4. Schematic of microscope layout including excitation, emission, and phase contrast pathways. Figure was reproduced from references[118,119]. A detailed description of optical elements can be found in accompanying text.

CHAPTER 3: DATA PROCESSING AND ANALYSIS

Introduction

Fluorescence image data is rich with information. One can obtain measurements of biomolecule position, diffusion behavior, proximity to cellular structures, and more. While the phrase "seeing is believing" is popular in the field, quantitation of image data is equally or more important for substantiating claims and hypotheses.

The Gahlmann lab has curated a robust framework for fitting, analyzing, and validating single-molecule tracking data. This chapter will discuss the general workflow which takes raw image data, identifies fluorescent single-molecules, and constructs single-molecule motion trajectories from which we can infer diffusive behavior of molecules. Further, I will discuss in detail the extensions that I have made to these analyses that have been integral to characterizing the iLID optogenetic system. This includes estimation of single-molecule residence times to infer kinetic constants in binding systems that match the timescale of measurement. I also implemented diffraction-limited image similarity measurements which is particularly useful for describing changes in fluorescence distribution in the same cell due to some stimulus. Lastly, I have extended our single-molecule trajectory Monte Carlo simulations to include a module for membrane-associated diffusion. This last improvement will prove useful in expanding our analyses to integral membrane protein diffusion and to proteins which associate dynamically to membrane embedded molecules.

3.1 Single-molecule localization

3.1.1 Point spread function fitting

Raw image data was processed using a modified version of the easy-DHPSF Matlab software[49,50,103,120]. The goal of the image processing package is to extract the three-

dimensional position of single-molecules. As described in Chapter 2, the precise position of the emitter is determined by fitting the double helix point spread function to a double Gaussian model. The center position between the two fluorescent lobes is used to estimate the lateral (x- and y-) position of the molecule, while the angle between the two lobes is used to estimate the axial position (z- position). A calibration curve is created by imaging a fluorescent bead over an axial range of ~3 μm and is used to generate template images. Raw data images are scanned for fluorescent profiles which match the template images to identify potential DHPSF signals. Then, potential DHPSFs are fit with a double Gaussian model where maximum likelihood estimation is used to statistically discern fluorescence signal from background using model parameters such as gaussian lobe width. Fit localizations are filtered using quality metrics including number of photons collected, distance between DHPSF lobes, lobe intensity ratio, and lobe width.

To correct for drift in the stage, which could bias diffusion data, each sample is imaged with a fluorescent fiducial marker whose position is tracked and used to correct the position of the emitter over time. Drift-corrected localizations are then subject to subsequent analyses.

3.1.2 Fluorescence data registration to bacterial cells

Localization data obtained from easy-DHPSF must be assigned to cells to establish boundaries for diffusion. First, phase contrast images of the imaged field of view are used to derive cell outlines using OUFTI[121] software. Any cells which show morphological abnormality (e.g. excessively long/undivided cells) are not considered for further analyses. Then outline meshes are exported to a previously described Matlab script which uses a 2-step 2D affine transformation to register localization data to cells[49,50,103]. The built-in

Matlab function 'cp2tform' is used to accomplish the affine transformation, both translating localization data laterally, and scaling the distance between localizations to fit within cell outlines. In the first step, five pairs of matching points on cell outlines and localization data are manually chosen to roughly align the data. Cell outlines containing less than 10 localizations are removed from analysis. The second step uses the center of mass of localizations to finely align localization data to the center of the cell outline, using a larger number of control points for alignment. Localizations outside of cell outlines are removed, and outline-internal localizations are used in subsequent diffusion analyses.

3.2 Diffusion analyses

The diffusion rate of biomolecules provides information about both intrinsic and extrinsic factors. Diffusion rate (D) in a given medium can be described by the Stokes-Einstein relationship:

$$D = \frac{k_b T}{6\pi\eta \mathrm{R}}$$

which shows that diffusivity of a molecule is directly related to the thermal energy in the system in terms of temperature (T) and the Boltzmann constant (k_b). On the other hand, viscosity (η) of the environment, and the hydrodynamic radius (R), are inversely related to the diffusion rate of a biomolecule. Given a stable environment in which temperature and viscosity are held constant, it is possible to use diffusion measurements to derive information about the hydrodynamic radius, and thus oligomerization state of the tracked molecule. For an in-depth discussion of protein diffusion and fitting models, refer to the introduction of the thesis in Chapter 1.

3.2.1 Mean Squared Displacement Analyses

To perform diffusion analyses, single-molecule positions over time must be linked into trajectories. Localizations identified in consecutive frames were linked into the same trajectory, with a 2.2 μm maximum distance between localizations considered for linking. This threshold was chosen to reflect the diffusion rate of a free fluorescent protein, including an additional 25% buffer for localization error. If multiple molecules were identified within the time frame of the trajectory within a given cell, the trajectory was discarded to minimize the possibility of mis-assignment. Further, only trajectories with at least four displacements were used in further analyses.

To calculate the diffusion rate of each single-molecule, we found the mean squared displacement (MSD) using the relationship:

$$\mathrm{MSD} = \frac{1}{(N-1)} \sum_{n=2}^{N} (x_n - x_{n-1})^2$$

where *x* is the 3D position at timepoint *n*, including up to 11 timepoints for calculating the mean over 10 displacements. Longer trajectories were truncated to contain 10 displacements to ensure multiple diffusive states were not averaged over in the MSD analysis. The MSD measurement was then used to calculate the apparent diffusion coefficient (*D**) according to:

$$D^* = \frac{\mathrm{MSD}}{2 \cdot m \cdot \Delta t}$$

where *m* is the dimensionality of the measurement (*m*=3 for the 3D trajectories reported here), and Δ*t* is the camera exposure time used for imaging (Δ*t*=25 ms under our conditions).

3.2.2 Radial distribution analyses – 2D cross section projections

The diffusion analyses in the previous section quantifies the rate of movement of single-molecules. We next chose to explore how the diffusion rate of molecules correlated with their spatial distribution. The vector describing the central axis of each cell was determined using the cell outline generated from OUFTI. The outline was segmented into sections along the cell length (**Figure 3.1**), and localizations from trajectories in each section were projected onto a 2D plane. The position of the central cell axis was adjusted to match the centroid of all localizations within the section. Positions of localizations from each cell were scaled to match the mean cell radius and mean cell length, which was calculated from OUFTI outlines. The trajectories were classified as slow or fast diffusing using the threshold $D^* = 0.15\ \mu m^2/s$ which was determined by identifying a transition point from the first major change in slope in the CDF plot of apparent diffusion coefficients of data containing both iLID-associated and cytosolic diffusion (**See Chapter 4, Figure 4.3)**. The width-normalized localizations from each trajectory was used to generate 2D histograms with 20nm x 20 nm bin widths, to match the experimentally measured localization precision.

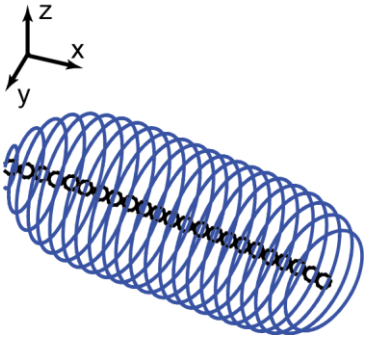

Figure 3.1. Cell sections generated from OUFTI outline. The mesh output from OUFTI is used to create equally spaced sections (blue lines) along the length of the cell. The midpoint between the two halves of the outline are used to generate the central cell axis vector (black circles).

3.2.3 Residence time analysis

In single-molecule microscopy, the time a fluorescently labeled protein spends bound to a cellular structure is often referred to as the residence time. Residence time measurements have been used to characterize a variety of phenomena including, but not limited to, fibrinogen-substrate interactions[122], enzyme reaction rates during DNA repair[43], and transcription factor sequence search and binding[41,123-125]. The amount of time that a ligand stays bound to its substrate is an indicator of the activity of an enzyme and/or the affinity of the interaction, whereas the half-life of the bound state is inversely related to the dissociation constant, K_D[126]. Single-molecule studies using long exposure time, 2D fluorescence assays are often used for making such measurements. Using long exposure times decreases the time resolution of the measurement. Therefore, we sought to quantify residence times using our full-length single-molecule trajectories. Labeling with the dye JFX549, which has exceptional photostability[127], allowed us to track molecules over hundreds of milliseconds up to multi-second time scales. Thus, we postulated that we would observe some state switching of molecules from bound to unbound or *vice versa*.

To identify diffusive state transitions in single-molecule trajectories, we instituted a workflow to analyze displacement data over time (**Figure 3.2a and c**). First, we plotted the additive, or cumulative displacement (CD) as a function of time elapsed according to:

$$\mathrm{CD}(t) = \sum_{t=1}^{N} \sqrt{(x_t - x_{t-1})^2}$$

where *x* is the 3D position at timepoint *t*. The CD was calculated for each displacement, for the full trajectory length (N).

The instantaneous rate of displacement was estimated by finding the slope within a small, sliding window containing 3 displacements for the full length of the trajectory (**Figure 3.2**). The size of the sliding window was chosen to be small enough such that switching events were not excessively averaged over, while being large enough to be somewhat insensitive to random displacement size fluctuations that are unconnected to binding and unbinding events. Each segment of the trajectory was then classified as bound or free by calculating its slope and comparing it to a threshold, which was chosen to match the upper-limit of the displacement sizes used in the membrane-bound single-molecule trajectory simulations at 0.2 $\mu m^2/s$ (**see section 3.3.2**). Trajectories which contained consecutive segments of fast-slow-fast state assignments were used for further analysis because of the presence of a bound state that is preceded and proceeded by an unbound state. To be considered for analysis, the molecule must reside in each state for at least 2 segments (4 displacements) of the trajectory to ensure that the identified state change was a true diffusive state change and not due to random fluctuation. Each switching trajectory was ascribed a score (TS) by how well the slope of trajectory segments matched simulated diffusion coefficient slopes derived for freely diffusing, cytosolic and membrane-bound molecules:

$$TS = \frac{1}{N_{seg} - 2} \sum_{i=1}^{N_{seg}} e^{-|m_i - m_s|}$$

where m_i is the slope fit to the experimental trajectory segment, and m_s is the slope derived from free cytosolic or membrane-bound simulated data, depending on the state assigned to the trajectory segment. N_{seg} refers to the number of segments in the trajectory. Switching trajectories were ranked by their TS, and the top-scoring trajectories (TS>~0.16) were

inspected individually to verify that switching events occurred at the membrane of the cell. The residence time (t_{bound}) of bound molecules in these switching trajectories was calculated by determining the number of displacements the molecule was assigned to the bound state.

A similar analysis was employed by Chung et al.[46] where they evaluated the cumulative squared displacements over time, combined with Hidden Markov Model (HMM) analyses to identify state transitions. This analysis allowed them to differentiate epidermal growth factor receptor monomer-dimer transitions. The diffusion rate, and thereby cumulative square displacements slopes, of monomer and dimer populations differed by approximately a factor of two (0.1 $\mu m^2/s$ versus 0.2 $\mu m^2/s$). Therefore, the HMM model was absolutely required for differentiating these populations. Because our data contains two, very well separated populations (0.2 $\mu m^2/s$ versus 5.5 $\mu m^2/s$), this added degree of complexity was not necessary for identification of state transitions within trajectories. Further, trajectories collected in cells which didn't express the MA-iLID binding partner did not show any verified state switching events, lending credence to our workflow model.

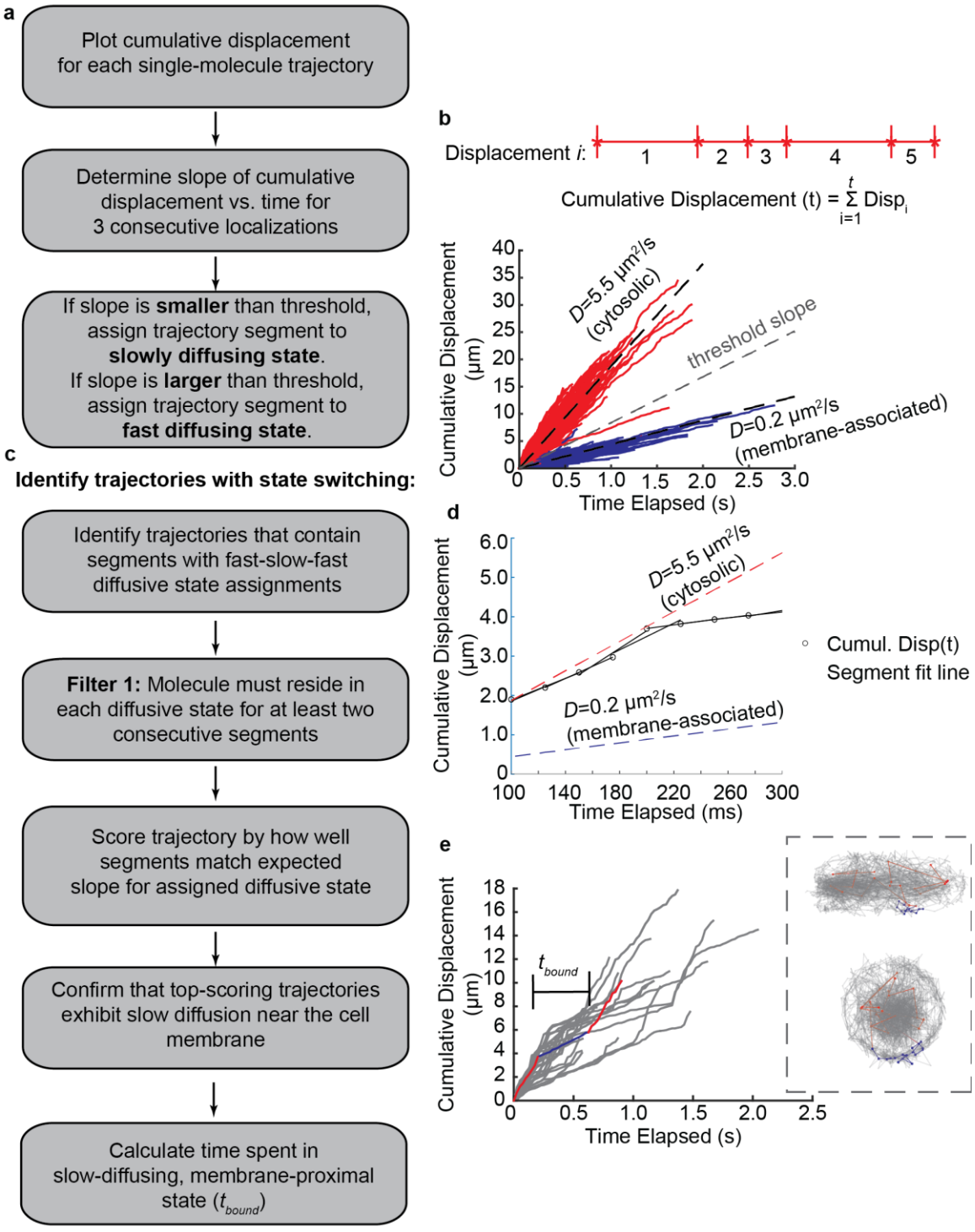
a
Plot cumulative displacement for each single-molecule trajectory
Determine slope of cumulative displacement vs. time for 3 consecutive localizations
If slope is **smaller** than threshold, assign trajectory segment to **slowly diffusing state**.
If slope is **larger** than threshold, assign trajectory segment to **fast diffusing state**.
c
Identify trajectories with state switching:
Identify trajectories that contain segments with fast-slow-fast diffusive state assignments
Filter 1: Molecule must reside in each diffusive state for at least two consecutive segments
Score trajectory by how well segments match expected slope for assigned diffusive state
Confirm that top-scoring trajectories exhibit slow diffusion near the cell membrane
Calculate time spent in slow-diffusing, membrane-proximal state (t_{bound})
b
Displacement *i*: 1 2 3 4 5
Cumulative Displacement (t) = $\sum_{i=1}^{t}$ Disp$_i$
Cumulative Displacement (μm)
D=5.5 μm²/s (cytosolic)
threshold slope
D=0.2 μm²/s (membrane-associated)
Time Elapsed (s)
d
Cumulative Displacement (μm)
D=5.5 μm²/s (cytosolic)
D=0.2 μm²/s (membrane-associated)
Cumul. Disp(t)
Segment fit line
Time Elapsed (ms)
e
Cumulative Displacement (μm)
t_{bound}
Time Elapsed (s)

Figure 3.2. Cumulative displacement analysis of single-molecule trajectories to derive molecule residence time. (a) Workflow of cumulative displacement analysis to distinguish fast, cytosolic diffusing molecules from slow, membrane-associated molecules. (b) Top panel: Schematic of displacement data transformed into a 1D trajectory to illustrate displacement size over time. The cumulative displacement is the sum of all displacements up to a given time point, *t*. Bottom panel: Cumulative displacement over time for $SspB_{micro}$ trajectories collected in MA-iLID expressing cells (256 nM) in unactivated conditions. A threshold slope corresponding to D = 1.75 $\mu m^2/s$ was used to distinguish fast diffusing molecules (blue) from slow diffusing molecules (red). Simulated trajectories in the cytosol at 5.5 $\mu m^2/s$ and in the membrane at 0.2 $\mu m^2/s$ recapitulated experimental cumulative displacement slopes and were used as reference slopes in the following steps. (c) Workflow used to identify trajectories with state-switching (see text for details). (d) Example of a $SspB_{micro}$ partial trajectory which exhibits state-switching. Three consecutive cumulative displacements are fit to a line, and the slope is compared to the threshold slope to classify the trajectory segment as cytosolic or membrane-bound. The slope of the segment is then compared to the reference slope for cytosolic diffusion or membrane diffusion depending on the state assignment, and scored by how closely they match. Trajectories with at least 2 consecutive segments in cytosolic and then membrane-associated states (or vice versa) are categorized as state-switching and used for later analysis. (e) Cumulative displacements over time of trajectories which show state transitions of fast-slow-fast. Trajectory localization of example fast(blue)-slow(red)-fast(blue) state-switching cumulative displacement plotted to highlight state transition at

the membrane of the cell. Time spent in bound state (red portion of trajectory) is integrated to calculate the residence time t_{bound}.

3.3 Model validation

3.3.1 Simulation of Cytosolic Single-molecule Trajectories

Cytosolic diffusion simulations were performed as described previously[49,50]. Brownian motion was simulated at 5.5 $\mu m^2/s$. The rate of diffusion was approximated from the slope derived from cumulative distribution analysis (see section 3.1.2) of fast diffusing molecules. The initial position of the single-molecule trajectory was randomly chosen within the volume of a cylinder with dimensions that match those of an *E.coli* cell (radius (r) = 0.5 μm, length (l) = 2.5 μm). Molecule diffusion was simulated at a time interval appropriate for the application. For single-molecule trajectory analysis, 100 ns time intervals were used. Trajectories used for generating diffraction-limited images were simulated at 1 μs to match the longer exposure time used in imaging, and decrease the computational load of the simulation. Diffusion of molecules was confined within cylindrical boundaries, assuming hard-sphere reflection of the molecule. Any molecules which diffused outside of the boundary within a time step were allowed to collide with the cell boundary, and then reflected back into the cylinder at a random angle[118].

3.3.2 Simulation of Membrane-associated Single-molecule Trajectories

Monte Carlo simulations of modified Brownian motion on the cell surface were performed for molecules diffusing at 0.2 $\mu m^2/s$. The rate of diffusion was approximated from the slope derived from cumulative distribution analysis (see section 3.1.2) of slow diffusing molecules. Diffusion on the spherical endcaps, and cylindrical body of the surface

were modeled separately due to the difference in curvature. The initial position of a single-molecule was randomly chosen on the surface of a spherocylinder with dimensions which match those of an *E. coli* cell (radius (r) = 0.5 μm, length (l) = 2.5 μm). The fraction of molecules with initial positions on the cylinder or hemispherical portions of the surface was determined by using the surface area ratio of each section where the probability of a molecule starting on the cylindrical surface (p_c) is given by:

$$p_c = \frac{2\pi r^2 l}{2\pi r^2 (l + 2)}$$

It follows that the probability of a molecule starting on the hemispherical portions (p_s) is then:

$$p_s = 1 - p_c$$

Molecule diffusion was simulated at a time interval appropriate for the application. For single-molecule trajectory analysis, 100 ns intervals were used. For use in diffraction-limited image simulation, we chose a longer time interval of 1 μs to match the longer exposure time used in imaging, and decrease the computational load of the simulation.

Molecule diffusion was constrained to the surface of the spherocylinder, but molecules were allowed to move freely between the cylindrical and hemispherical surfaces to create a continuous surface for diffusion. On the cylindrical surface, the direction of movement was determined by finding a random angle, and the displacement was split into lateral and curved displacements to maintain the distance of the molecule at (r) from the center axis of the object. Curved displacements were resolved using rotation matrices. If a molecule's lateral position exceeded the length of the cylindrical surface, the remaining displacement occurred on the hemispherical surface.

On the hemispherical surface, the position at step (t) was described using a vector matrix. The direction of diffusion was determined by finding a random angle, and the position was updated using vector addition, approximating 2D diffusion. To ensure that the molecule did not diffuse away from the hemispherical surface, the length of the updated vector was scaled to the radius of the cell. This strategy works well for very small step sizes, as the scaling factor is very small, and will have a negligible effect on the step size. Larger step sizes may require a more nuanced strategy for updating the molecule position. If a molecule's lateral position exceeded the hemispherical radius, the remaining displacement occurred on the cylindrical surface, as described in the previous paragraph (**Figure 3.3**).

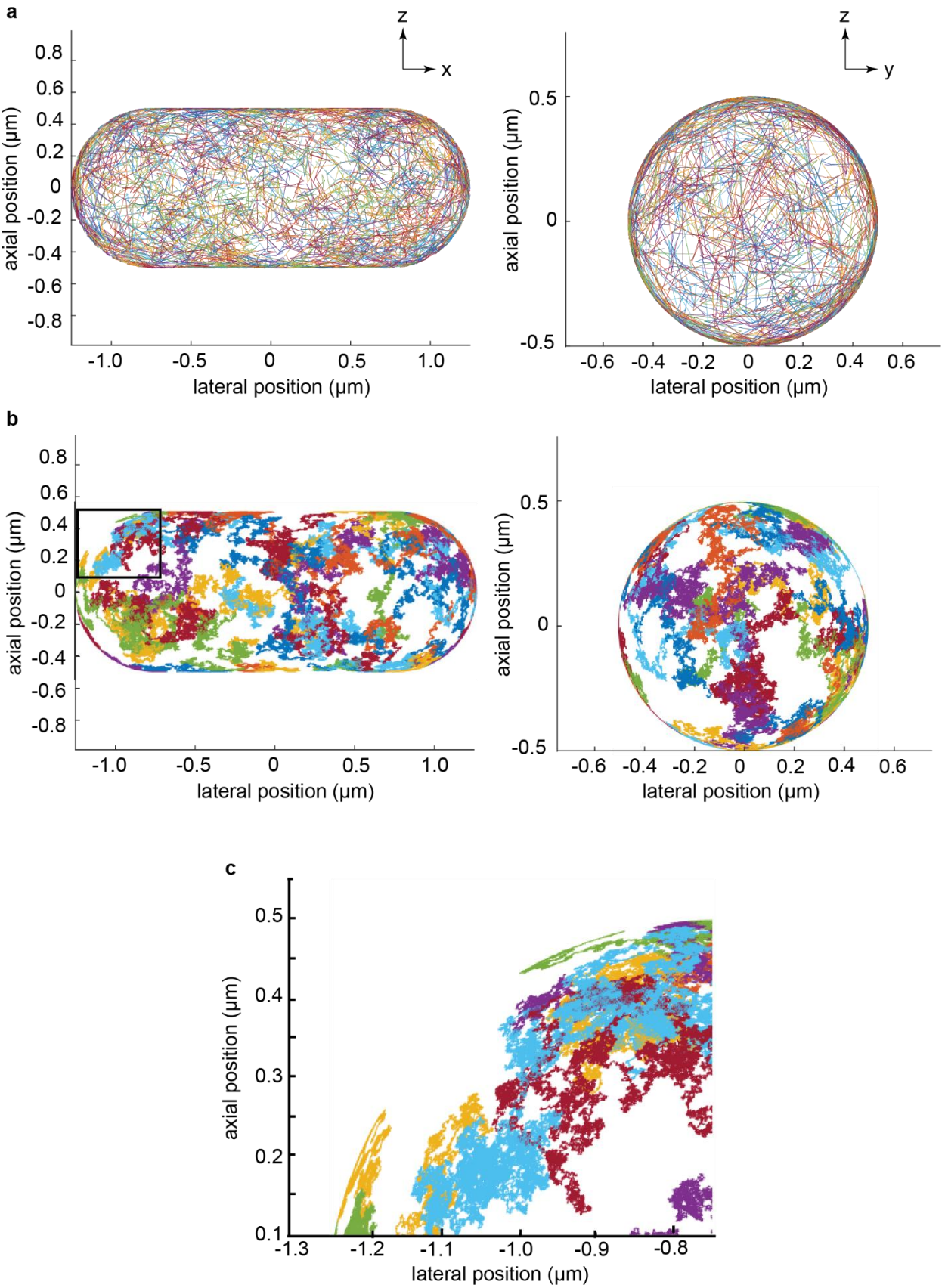
a
z
x
axial position (µm)
lateral position (µm)
z
y
axial position (µm)
lateral position (µm)
b
axial position (µm)
lateral position (µm)
axial position (µm)
lateral position (µm)
c
axial position (µm)
lateral position (µm)

Figure 3.3. Simulated membrane-associated single-molecule trajectories. (a) 3D single molecule trajectories of molecules diffusing at 0.2 $\mu m^2/s$. Macrostep positions were sampled every 25 ms for a total of 125 ms. Left: top view. Right: *en face* view. N= 1,000 trajectories. **(b)** 3D single molecule trajectories of molecules diffusing at 0.2 $\mu m^2/s$. Microstep positions were sampled every 100 ns for a total of 125 ms. Only the first 62.5 ms of each track is visualized. Left: top view. Right: *en face* view. N = 100 trajectory subset of 1,000 trajectories simulated. **(c)** Cropped region indicated in left panel of (b). Visualized to show molecules can pass between the hemispherical and cylindrical regions of the cell freely.

3.3.3 Single-molecule image generation

It is important that simulated data matches the experimental conditions as closely as possible to ensure that analyses of single-molecule trajectories are benchmarked properly. Therefore, we subject our simulated trajectories to the same data fitting and analysis pipeline as our experimental data. To convert our trajectory simulations into a form that can be properly analyzed, we must first generate noised, motion-blurred images of single-molecule trajectories.

Image simulation of DHPSF images for single-molecule trajectories was performed as described previously[49,50,118]. Images were generated for each 25 ms exposure time by sampling 50 sub- positions of 25,000 total micropositions within the displacement. A DHPSF image was generated for each subposition, and then these images were summed to generate the total image with a motion-blur effect. The number of photons emitted was set to 2,000 to mimic the fluorescence emission of typical fluorescent proteins such as eYFP. Laser background of approximately 13 photons per pixel was added. Poisson noise, dark

offset, and Gaussian read noise were added to the image. The final images were then converted to signal counts by multiplying by the experimentally measured and calibrated camera gain. Images in this form were processed as described for experimentally collected images, and used for localization, tracking, and cumulative displacement analyses.

3.3.4 Simulation of Diffraction limited images

Trajectories of cytosolic and membrane-associated diffusing molecules were simulated as described above in sections 3.1.3 and 3.1.4. Molecule positions were sampled every 200 ms from the microstep trajectories, resulting in 6 localization positions (macro-positions) per track.

The 3D molecule macro-positions were used to generate conventional diffraction-limited 2D point-spread functions of isotropic emitters using a vectorial light propagation model adapted from Yan et al. (2019)[116]. We modified the algorithm to omit the double helix phase mask and optical aberrations. In the simulation, the nominal focal plane was positioned at the center of the cell. A total of 10,000 trajectories were simulated for both cytosolic and membrane-bound molecules, providing 60,000 total emitter positions in each condition. Noised images obtained for each emitter were added to attain the total image. To attain mixed population images, trajectories were chosen at random from the total simulated trajectory population to reflect the specified membrane-associated molecule fraction.

3.4 Quantifying fluorescence redistribution using SSIM

To quantify the optogenetic response to 488 nm illumination, a population-level analysis of all imaged cells was performed. Image stacks from each condition were

averaged and background subtracted. Post-illumination images were contrast-inverted and used to generate cell outlines using OUFTI.[121] OUFTI outlines were used to make a binary mask so that single-cells images were compared to themselves before and after activation. The structural similarity index matrix (SSIM) was used to assess image similarity between before- and after- 488 nm illuminated images using the following relationship:

$$SSIM = [l(x,y)]^{\alpha} \cdot [c(x,y)]^{\beta} \cdot [s(x,y)]^{\gamma}$$

where luminance (*l*), contrast (*c*), and structure (*s*) is compared between the two images (*x* and *y*) with weights α,β, and γ, respectively. The luminance term is indicative of the overall, average pixel intensity (μ) of image x or y:

$$l = \frac{2\mu_x\mu_y + C}{{\mu_x}^2 + {\mu_y}^2 + C}$$

where *C* is a constant that is a measure of the pixel value range. To decrease the contribution of photobleaching to the measurement when comparing frame to frame, each pixel of an image was normalized to the total intensity counts in the image.

The contrast term compares the standard deviation (σ) in pixel intensity within each image, providing a measure of the range in intensity values (e.g. large standard deviation results in a large contrast term):

$$c = \frac{2\sigma_x\sigma_y + C}{{\sigma_x}^2 + {\sigma_y}^2 + C}$$

Finally, the structure term is a measure of the covariance (σ_{xy}) between the two images and is given by (high correlation in relative pixel intensities results in a large covariance/structure term):

$$s = \frac{\sigma_{xy} + C}{\sigma_x\sigma_y + C}$$

The built-in Matlab (The MathWorks, Inc, Natick, Massachusetts) function “ssim” was applied to the masked images with equal weighting of the comparison metrics to assess the degree of image similarity. We found that each comparison term offered different values in the similarity assessment. However, the trends observed between imaging treatment conditions were conserved, so we chose to use equal weighting.

CHAPTER 4:

INTERACTION OF ILID OPTOGENETIC PROTEINS CHARACTERIZED USING SINGLE-MOLECULE TRACKING IN LIVE *E. coli*

****Chapter adapted from Achimovich, A. M., Yan, T. & Gahlmann, A. *Dimerization of iLID Optogenetic Proteins Observed Using 3D Single-Molecule Tracking in Live Bacterial Cells* (bioRxiv, 2022).[128]**

AM Achimovich created bacterial strains required for imaging, designed and performed all experiments and data analysis, as well as single-molecule trajectory simulation and analysis. T Yan wrote diffraction-limited image simulation code. A Gahlmann conceived the study and experimental setup. AM Achimovich and A Gahlmann wrote the manuscript.

4.1 Introduction

Many fluorescence microscopy-based techniques have been developed over the past decades to detect and quantify interactions between biomolecules *in vitro* and *in vivo*. Improvements of fluorescent probes and biomolecular labeling technologies in conjunction with instrumental improvements have enabled measurements that provide critical insights into cellular organization and the biochemical interactions occurring within them.[14] Spatial co-localization of emitters through multi-color imaging has been widely utilized to gauge whether biomolecules are close in space and are thus able to interact. The power of such measurements depends critically on the achievable spatial resolution of the instrument used. Diffraction-limited imaging provides 200-300 nm resolution, which is orders of magnitude larger than the size of a typical protein (~2 nm) or the size of small protein complexes (~20 nm). Diffraction-limited resolution is thus too low to conclusively determine whether two proteins interact directly or whether their interaction is mediated by a third protein[15]. Super-resolution microscopy approaches such as PALM/STORM and MINFLUX, have been successful in addressing this challenge by enabling precise single-molecule localization with tens of nanometers of precision. For example, Symborska et al. determined radial positions of protein subunits of the nuclear pore complex (NPC) with subnanometer precision using PALM/STORM in conjunction with particle averaging[16]. This approach was later extended to achieve a 3D reconstruction of the nuclear pore complex through iterative multi-color imaging of each NPC subunit relative to a reference protein also within the NPC.[129] More recently, Ries and co-workers used MINFLUX microscopy to pinpoint the position of subunits within the NPC with single nanometer precision without the need for radial averaging[17]. Thus, for relatively large, immobile, and

highly symmetric structures like the nuclear pore complex, super-resolution fluorescence microscopy can provide accurate co-localization data that provides information on how individual subunits interact with each other.[18-20]

Detecting protein interactions within freely-diffusing complexes cannot be accomplished by fluorescence co-localization and thus requires different approaches. Live cell measurements of protein oligomerization is possible using fluorescence microscopy techniques such as Fluorescence recovery after photobleaching (FRAP), and Fluorescence correlation spectroscopy (FCS)[130-132]. These methods have gained popularity due to the increased availability of commercial confocal laser scanning microscopes over the past twenty years. Because they provide complimentary measurements, FCS and FRAP can be used together to probe binding kinetics of protein-protein interactions[133,134]. However, it is difficult to identify transient binding events from these data because these methods provide ensemble-averaged data. Alternatively, Forster resonance energy transfer (FRET), measures the efficiency of non-radiative energy transfer from an excited donor fluorophore to an acceptor fluorophore in the ground state over a distance of a few nanometers[24,135]. Thus, FRET efficiency serves as a measurement of spatial proximity of fluorescently labeled proteins and can be used to infer protein-protein interactions.

Detecting interactions of diffusing proteins using dual-color single-molecule microscopy is not practically feasible because both fluorophores used to label the putative interacting proteins must be in a fluorescent ON state at the same time within the same complex. The probability of observing such co-diffusion directly in separate color-channels is negligibly small, because fluorophore photo-activation or blinking in

PALM/STORM occurs stochastically. To avoid this problem, the diffusive behaviors of putative interacting proteins can be measured in separate experiments. If the two proteins diffuse at the same rate, then it is possible that they exist within the same protein complex. Because single-molecule trajectories in living cells are limited in duration by fluorophore photobleaching, information from thousands of trajectories are often pooled and statistical data analysis approaches are employed to resolve different diffusive states[48,49,51,136-140]. Indeed, different diffusive states can be resolved in living cells due to homo- and heterooligomeric complex formation among interacting proteins[49,50,103] or proteins binding to quasi-stationary structures, such as DNA[39,43,101,141-148]. However, to assign diffusive states to specific biomolecular complexes of different protein compositions, additional experimental perturbation is needed. Single-point mutations or genetic deletion mutants of potential interacting partners can be used as a tool to disrupt putative complexes and observe changes in diffusive behavior. A drawback of such genetic approaches is that the permanent disruption of an interaction interface or absence of a binding partner can interfere with cellular processes in ways that are difficult to predict or control, or yield the cells inviable[149,150]. Therefore, controllable, transient perturbations of cellular processes on experimentally-relevant time scales is preferable.

Optically and chemically induced dimerization provides a favorable alternative to permanent genetic perturbations. Such optogenetic and chemogenetic dimerization systems enable manipulation of protein spatial localization to non-native cellular compartments. These methods will be referred to as knocksideways assays[76,151]. In a knocksideways experiment, one of the dimerizing molecules is attached to a cytosolic

protein of interest and the other dimerization partner is targeted to a cellular location that differs from the native localization of the tagged protein of interest (e.g. the cell membrane). Upon optical or chemical stimulation of dimerization, the protein of interest is sequestered away from its native localization, and interacting proteins can be sequestered along with it. Optogenetic knocksideways experiments can thus be used to detect molecular interactions in living cells.

We reasoned that manipulating the spatial distributions of otherwise cytosolic proteins would aid the assignment of diffusive states (observed in single-molecule tracking experiments) to protein complexes of specific protein composition. In the simplest scenario, depletion of the cytosolic diffusive state corresponding to the suspected oligomer would be expected when either interacting partner is sequestered to the membrane. Chemogenetic systems rely on dimerization being induced by a diffusing molecule itself, whereas optogenetic systems can be activated by photon absorption. Optogenetic systems thus allows for more precise spatial and temporal control over dimerization than chemogenetic systems.

Here, we test the possibility of combining optogenetic manipulation with 3D single-molecule tracking microscopy in live *Escherichia coli*. The improved Light Induced Dimerization (iLID) system[4] was selected because it has been extensively characterized and engineered for optimized performance in different model systems. Thus, a considerably large toolbox of iLID variants with different affinities, and reversion times are available for implementation[77,78,152]. The iLID protein contains the light sensing light oxygen voltage (LOV2) domain derived from *Avena sativa* which incorporates a flavin

cofactor during folding. The flavin cofactor acts as a chromophore, and forms a cysteine adduct with the LOV2 domain after illumination with blue light. As a result, the iLID protein changes conformation and exposes a binding site for the interacting partner, SspB[79,80]. We demonstrate that the iLID system exhibits a robust response after 488 nm illumination in low-intensity excitation conditions used for diffraction-limited imaging. Using single-molecule tracking, we found that $SspB_{micro}$ exhibited the most substantial 488 nm-induced response among three tested SspB mutants. Surprisingly, our results also reveal that activation of the optogenetic response also occurs under high intensity illumination conditions, even at wavelengths for which iLID shows minimal absorbance. Titrating the iLID expression level with respect to SspB reduced imaging laser-induced iLID:SspB interaction in 3D single-molecule tracking experiments Together our results establish the need for careful calibration of the optogenetic system prior to its application to imaging experiments.

4.2 Results and Discussion

4.2.1. Diffraction-limited imaging indicates a robust redistribution of otherwise cytosolic fluorescence to the membrane upon blue-light activation.

Optogenetic tools have been widely applied in eukaryotic cells in conjunction with diffraction-limited fluorescence microscopy to obtain population-averaged, phenotypic readouts[70,81]. Therefore, we sought to quantify the optogenetic response of the iLID system in K12 *E.coli* using diffraction-limited imaging. We expressed the iLID protein from an inducible arabinose promoter and targeted it to the inner membrane using an N-terminal genetic fusion containing a modified single transmembrane spanning helix derived from

the *E.coli* transmembrane protein, TatA[153,154]. This construct, herein referred to as MA-iLID, was previously used for stable insertion into the inner membrane of gram negative bacteria and has been shown to enable optogenetic disruption of type 3 protein secretion in *Yersinia enterocolitica.*[73]. We genetically fused the strongest reported iLID binding partner, $SspB_{nano}$, with a C-terminal Halo tag, and expressed this construct from a second, constitutively expressing plasmid. $SspB_{nano}$-Halo was labeled with JFX549 for visualization in fluorescence imaging experiments[127] (**Figure 4.1a**). For simplicity, the JFX549-labeled $SspB_{nano}$-Halo is referred to as $SspB_{nano}$ in this chapter.

Prior to optical activation of MA-iLID with 488 nm laser light, we observed a uniform distribution of cytosolic $SspB_{nano}$. Redistribution of $SspB_{nano}$ to the membrane was dependent on both expression of MA-iLID and 488 nm laser illumination (~1mW/cm^2) (**Figure 4.1b-d**). We quantified $SspB_{nano}$ redistribution upon 488 nm laser illumination in each cell using the structural similarity index measure (SSIM), which quantifies similarity between two images[155]. Cells expressing MA-iLID were more dissimilar (1-SSIM) after 488 nm laser illumination compared to controls (**Figure 4.1e**). To estimate the fraction of molecules that reside at the membrane in each condition, we simulated 2D diffraction-limited images that matched our imaging parameters and contained realistic noise contributions (see methods) (**Figure 4.1f, 4.2a**). Fluorescence line profiles across the midsection of cells showed a Gaussian-like line shape for cytosolic fluorescence, while membrane-associated fluorescence produced double-peaked line shapes. The experimental line shape obtained with a fluorescently labeled, membrane-anchored iLID protein (MA-mCherry-iLID) agreed well with line shape obtained based on simulated images of 100%

membrane localized molecules (**Figure 4.2b**). Based on qualitative comparison of simulated and measured line shapes, we estimate that the fraction of molecules at the membrane in living cells is close to 0% pre-activation and greater than ~80% post-activation. These data suggest that the iLID system can be used to efficiently sequester otherwise cytosolic molecules to the membrane.

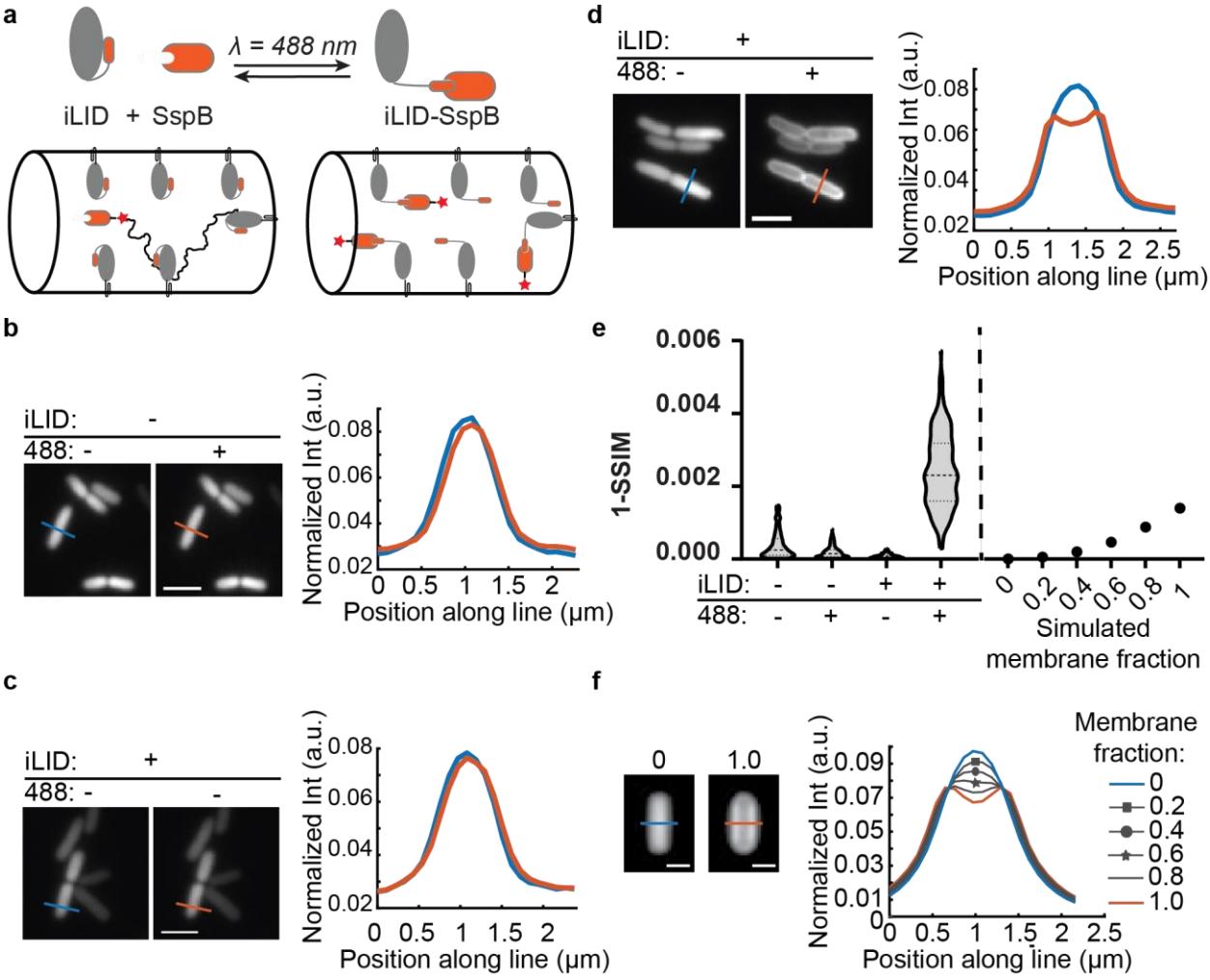

Figure 4.1. Diffraction-limited imaging indicates a substantial redistribution of SspB$_{nano}$ to the membrane after blue-light activation. (a) Schematic depiction of a knocksideways experiment using the iLID system. The iLID protein undergoes a

conformational change after 488 nm-light illumination and uncages a binding site for SspB. Halo-tagged (red star) cytosolic SspB binds to membrane-anchored iLID (MA-iLID) after 488 nm illumination. SspB-Halo is labeled with JFX549 for fluorescence imaging (hereafter referred to as SspB). **(b)** Diffraction-limited images of $SspB_{nano}$. Illumination with 488 nm light has no effect on the spatial distribution of $SspB_{nano}$ in the absence of MA-iLID. Fluorescence intensity line profiles across the midsection of the cell (normalized to the integrated line intensity) also exhibit no apparent shift in $SspB_{nano}$ spatial distribution. **(c)** Low intensity (~1 W/cm^2) 561 nm laser excitation over the entire exposure (80 seconds) is not sufficient to induce $SspB_{nano}$ sequestration to the membrane. **(d)** In the presence of MA-iLID, low intensity (~4 mW/ cm^2) 488 nm laser illumination shifts the spatial distribution of $SspB_{nano}$ to the cell membrane. The fluorescence intensity line profile across the midsection of the cell changes from a Gaussian-like line shape to a characteristic double-peaked line shape. **(e)** Left panel: Image dissimilarity (1-SSIM) of experimentally-acquired individual cell images before and after 488 nm illumination (n=200-350 cells in each condition). A population-level response in image dissimilarity is dependent on MA-iLID expression and 488 nm illumination. Right panel: Calibration of the image dissimilarity metric as a function of the fraction of membrane-associated fluorophores (relative to a simulated cell with 0% membrane-associated fluorophores). **(f)** Simulated diffraction limited images of cells with 0% or 100% membrane-associated fluorophores, respectively. Normalized line profiles of simulated diffraction-limited images (**Figure 4.2**) indicate a progressive broadening, and redistribution of fluorescence as the fraction of membrane-associated fluorophores increases.

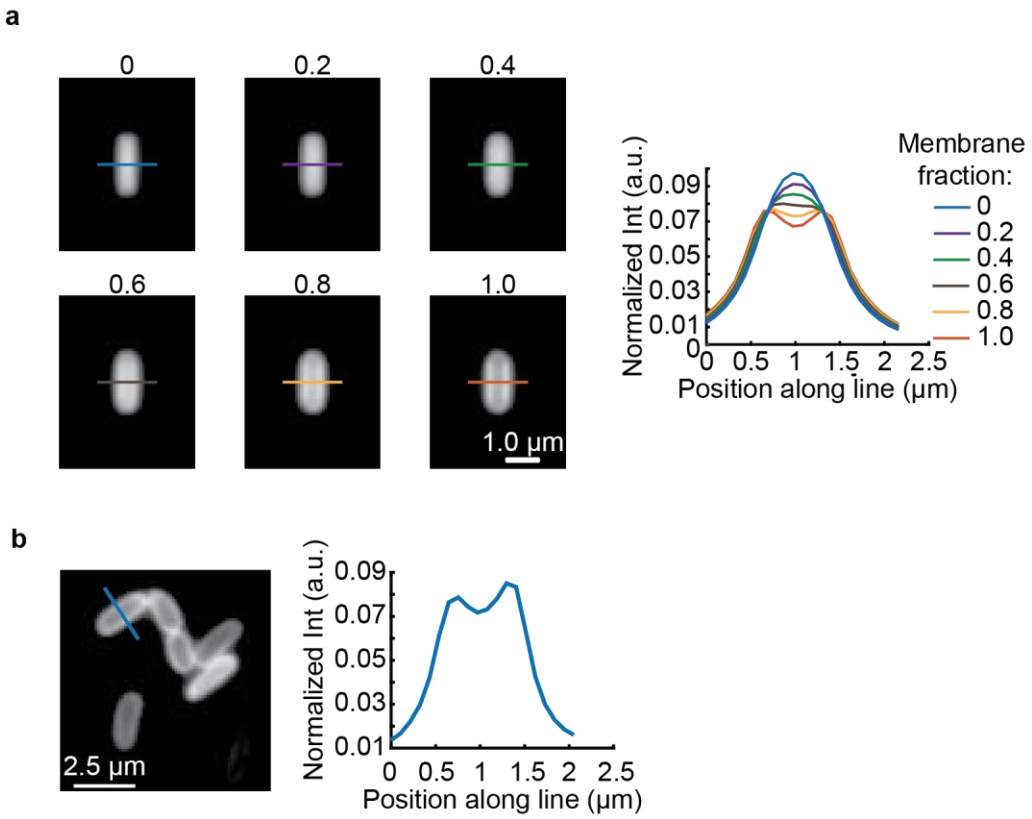

Figure 4.2. (a) Simulated diffraction-limited images of cells with increasing fractions of membrane-associated fluorophores show a clear shift in fluorescence intensity line profile across the midsection of cell. **(b)** Experimental fluorescence images and line profile observed for MA-mCherry-iLID qualitatively match that of simulated cells with 100% membrane-associated fluorophores.

4.2.2 3D single-molecule tracking data show increased SspB:iLID interaction prior to 488 nm illumination

Single-molecule tracking microscopy has been used to resolve different diffusive states of proteins that manifest in living cells due to protein complex formation[38]. Because

optical activation of the MA-iLID:SspB interaction allows for transient spatial redistribution of protein localization, the light-driven interaction could provide a means to non-invasively perturb the diffusive states that manifest in the cytosol of living cells. We therefore sought to measure SspB diffusive behavior in living cells and determine the extent of MA-iLID association using 3D single-molecule tracking. Based on the clear membrane localization of MA-iLID in diffraction limited images (**Figure 4.3**), we reasoned that $SspB_{nano}$ interacting with MA-iLID should diffuse along the membrane at a much slower rate than cytosolic $SspB_{nano}$. In 488 nm illuminated cells, the cumulative distribution function of apparent diffusion coefficients indeed shows a bimodal curve with a transition at $D^* = 0.15\ \mu m^2/s$ (**Figure 4.3a**). When plotting the spatial trajectories of slowly diffusing molecules ($D^* < 0.15\ \mu m^2/s$) it is clear that they localize near the bacterial membrane. On the other hand, the spatial trajectories of fast diffusing molecules ($D^* > 0.15\ um^2/s$) localize in the cytosol (**Figure 4.3b**). We conclude that it is possible to clearly distinguish freely-diffusing, cytosolic $SspB_{nano}$ from iLID-associated $SspB_{nano}$ molecules in living cells based on their diffusion rate and sub-cellular localization.

The $D^* = 0.15\ um^2/s$ threshold allowed us to estimate the relative population fractions of iLID-associated and cytosolic $SspB_{nano}$. In cells that do not express MA-iLID, the vast majority (95%) of $SspB_{nano}$ proteins diffuse fast and localize to the bacterial cytosol, as expected. The remaining 5% of tracked proteins were classified as slowly diffusing, but the corresponding trajectories showed no discernable preference for the membrane. The diffusive behavior and spatial distribution of $SspB_{nano}$ remained unchanged upon 488 nm illumination in these cells (**Figure 4.2a** and **c**). Surprisingly, and in contrast

to the diffraction-limited images (**Figure 4.1**), a large fraction of $SspB_{nano}$ proteins exhibited slow diffusion (48%) in cells that express MA-iLID, even in the absence of 488 nm light. This shift towards slow diffusion is accompanied with spatial redistribution of $SspB_{nano}$ to the membrane, whereas the fast diffusing population of proteins remained uniformly localized to the cytosol (**Figure 4.3d**). When cells expressing both $SspB_{nano}$ and MA-iLID were exposed to 488 nm light, we observed an additional shift towards slower diffusion and membrane-proximal localization (56%) (**Figure 4.3e**). The increase in iLID-associated SspB observed is marginal compared to the shift observed in diffraction-limited images (**Figure 4.1**). However, we note that the line profile quantitation of our experimental images represents an example of a single cell displaying an obvious change in $SspB_{nano}$ spatial distribution. Across a population the degree of response observed in line profiles varies. Further, the population level analysis of image dissimilarity performed on the diffraction limited images indicates a varied response to 488 nm illumination. This is likely due to expression level heterogeneity which is evident in whole cell fluorescence comparisons of both arabinose-promoter driven expression of MA-iLID, and constitutive expression of SspB (**Figure 4.1, Figure 4.2**).

We hypothesize that the discrepancy of MA-iLID associated SspB seen in diffraction-limited image quantitation compared to single-molecule trajectory data is due to the higher excitation intensity required for single-molecule localization microscopy. The absorption spectrum of iLID proteins shows very minimal absorption at wavelengths larger than 500 nm[112]. However, optical activation of the iLID:$SspB_{nano}$ interaction is possible with 514 nm light at illumination intensities typical for diffraction-limited imaging (~1

W/cm^2). (**Figure 4.4**). The intensity used for JFX549 fluorescence excitation by 561 nm laser light was three orders of magnitude higher in single-molecule imaging experiments (2 kW/cm^2). These data suggest that an increase in 561 nm photon flux is able to activate the iLID optogenetic response.

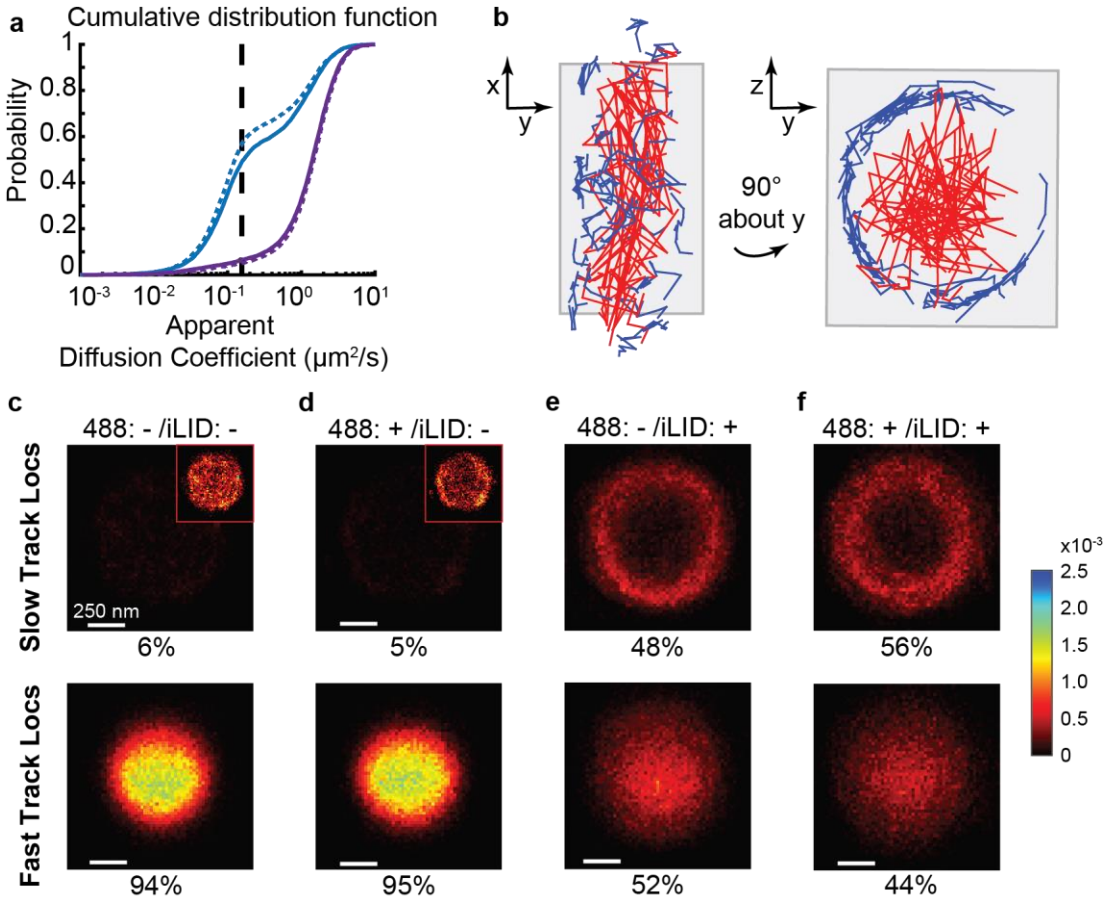

Figure 4.3. 3D single-molecule tracking data show SspB:iLID interaction prior to 488 nm illumination (a) Apparent diffusion coefficient distributions of $SspB_{nano}$ in the absence (purple, solid line, *N* = 11,523 tracks, 120 cells) and presence (blue, solid line, *N* = 8,542 tracks, 78 cells) of MA-iLID. Illumination with 488 nm light marginally increases the population of slowly diffusing $SspB_{nano}$ in MA-iLID expressing cells (blue, dashed line, *N* = 6,360 tracks, 88 cells), but not in cells which do not express MA-iLID (purple, dashed

line, N = 9,922 tracks, 94 cells). Vertical dashed line indicates threshold used to distinguish fast diffusers ($D^* > 0.15$ μm^2/s) from slow diffusers ($D^* < 0.15$ μm^2/s) **(b)** Single-molecule trajectories in a representative cell expressing MA-iLID, after illumination with 488 nm light. Left: top view. Right: *en face* cross sectional view. Slowly diffusing molecules (blue) clearly localize to the periphery of the cell and diffuse laterally along the membrane, while fast diffusing molecules (red) localize predominately to the cytosol and diffuse in 3D. **(c-f)** 2D histograms of localizations from slow and fast trajectories within the population of cells imaged. Histograms recapitulate trends observed in panel b. Bin size 20 nm x 20 nm. Each histogram is normalized to the total number of molecules observed in that experiment. Inset: rescaled (unnormalized) histograms, shown for clarity.

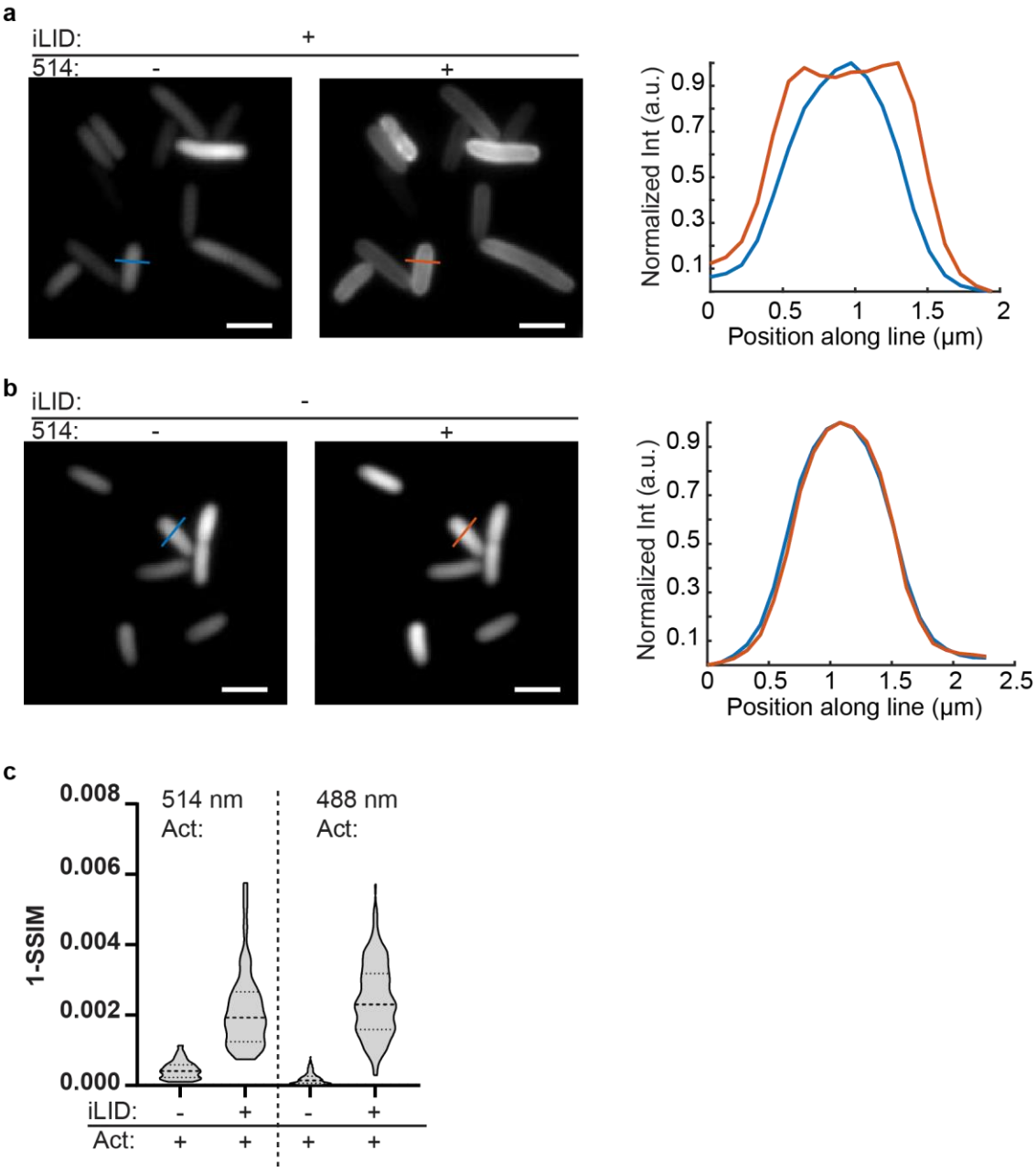

Figure 4.4. Optical activation of the iLID: $SspB_{nano}$ interaction is possible with 514 nm light (a) Spatial redistribution $SspB_{nano}$ is observed in cells expressing MA-iLID after 514 nm laser illumination. The fluorescence intensity line profile across the midsection of the cell changes from a Gaussian-like line shape to a characteristic double-peaked line shape. **(b)** Spatial redistribution of $SspB_{nano}$ is not observed after 514 illumination in cells

which do not express MA-iLID. Further, the fluorescence intensity line profile across the midsection of the cell retains its Gaussian-like line shape **(c)** Image dissimilarity (1-SSIM) analysis performed on the full cell population before and after 514 illumination. The image dissimilarity is comparable to cells illuminated with 488 nm light.

4.2.3 Single-molecule tracking of SspB mutants further indicate activation of iLID optogenetic response by high intensity 561 nm light.

To decrease the amount of iLID-bound SspB prior to 488 nm illumination, we made a series of previously characterized mutations to SspB[77,78]. These mutant versions of SspB, termed $SspB_{micro}$ and $SspB_{milli}$, have decreased binding affinity for the iLID protein. When we tracked single $SspB_{micro}$ and $SspB_{milli}$ proteins in living cells, we indeed observed a decrease in the fraction of slow diffusers near the cell membrane prior to 488 nm light illumination (**Figure 4.5a-c**). We found that 31% of $SspB_{micro}$ proteins were iLID-associated, while iLID-associated $SspB_{milli}$ comprised only 6% of the population. Upon 488 nm light illumination, the membrane-proximal, slow-diffusing fractions increased to 45% and 7%, respectively (**Figure 4.5b** and **c**). The magnitude of the optogenetic response thus differs between the mutants, with $SspB_{micro}$ showing the largest response, under otherwise identical experimental conditions. Diffraction-limited images of $SspB_{micro}$ and $SspB_{milli}$ recapitulate this trend (**Figure 4.6**). Previous work has also shown that the $SspB_{milli}$:iLID interaction is only minimally affected by blue light, as judged based on $SspB_{milli}$ localization to iLID-labeled organelles in HeLa cells[156].

The reported dissociation constants for the three abovementioned SspB mutants differ by six orders of magnitude. The data reported above was collected at the same

expression levels for each interacting protein components. $SspB_{nano}$ may thus saturate the available binding sites at the membrane at the expression level used. Consequently, a large increase in binding upon 488 nm illumination is not observed. At the other extreme, $SspB_{milli}$ may require a much higher number of binding sites to observe binding both before and after 488 nm illumination due to its inherently low affinity for the iLID protein. The comparatively larger optogenetic response observed for $SspB_{micro}$ suggests that the concentration of each interacting partner is better-matched to the dissociation constant for this mutant.

To test this model, we titrated the amount of MA-iLID, while keeping the expression level of $SspB_{micro}$ constant. To estimate the concentration of MA-iLID expressed at each L-arabinose induction concentration, we performed a calibration experiment in which we expressed MA-mCherry-iLID under the same promoter. The number of MA-mCherry-iLID proteins was estimated by dividing the initial fluorescence intensity of each cell by the average intensity of a single mCherry protein. Uninduced cells still expressed MA-mCherry-iLID at a concentration of ~90 nM due to leaky expression from the arabinose promoter (**Figure 4.7**). At the maximum inducer concentration used (13.3 mM), the MA-mCherry-iLID reached a concentration of ~510 nM. For the following analyses, we assume that MA-mCherry-iLID and MA-iLID are expressed at the same level for a given L-arabinose concentration.

Decreasing the concentration of MA-iLID, decreases the fraction of iLID-associated $SspB_{micro}$. At the lowest MA-iLID concentration, $SspB_{micro}$ does not show an appreciable population fraction of slowly diffusing, membrane-proximal molecules both

before and after 488 nm illumination (**Figure 4.5d**). At the highest concentration of MA-iLID , we estimate that 48% of $SspB_{micro}$ is iLID-associated. It is possible that this fraction could be augmented by further increasing the expression level of MA-iLID. However, we found that high expression of MA-mCherry-iLID leads to an increase in fluorescent foci formation, most often at the cell pole (**Figure 4.8a**). Fluorescent foci formation can be indicative of protein overexpression and subsequent aggregation and/or formation of inclusion bodies[157,158]. These processes do not necessarily interfere with protein folding and function[157,158]. Indeed, we observe fluorescent foci formation in the MA-mCherry-iLID data, but not to the same extent in the $SspB_{micro}$-Halo data (**Figure 4.8b**). These observations suggest that mCherry remains correctly folded and functional within the MA-mCherry-iLID construct, though the iLID protein within the fluorescent foci may not be functional or available for interactions with SspB. Due to the significant increase in fluorescent foci formation, we did not explore higher expression levels of MA-iLID.

Titration of MA-iLID expression allowed us to estimate the dissociation constant K_D of the $SspB_{micro}$:MA-iLID interaction in living cells. Because we observe 48% association of $SspB_{micro}$ at 507 nM MA-iLID, we estimate that the K_D is approximately 510 nM before 488 nm illumination. This value is about 100x smaller than K_D reported in *in vitro* fluorescence polarization assays in unactivated conditions[77]. However, as we argued above, the high intensity 561 nm excitation light activates the iLID optogenetic response. Therefore, it is more appropriate to compare results under activated conditions to the fluorescence polarization data. Indeed, the reported *in vitro* K_D is about 800 nM,[77] which is within a factor of two the K_D value we estimate in living cells. Further, we observe ~45%

association of $SspB_{micro}$ at ~260 nM MA-iLID in activated conditions, which represents an approximately 2-fold increase in affinity upon 488 nm illumination. The reported dynamic range derived from *in vitro* fluorescence polarization assays is reported to be a 58 fold change in binding affinity due to activation of the system. However, we note that proteins reconstituted in lipid bilayers show a shortened dynamic range of binding affinity, observing a 2.7-fold change in affinity upon iLID-activation[159,160]. Together, these results suggest that proximity to the membrane, and the steric hindrance imposed by it may affect the dynamics of the SspB:iLID interaction.

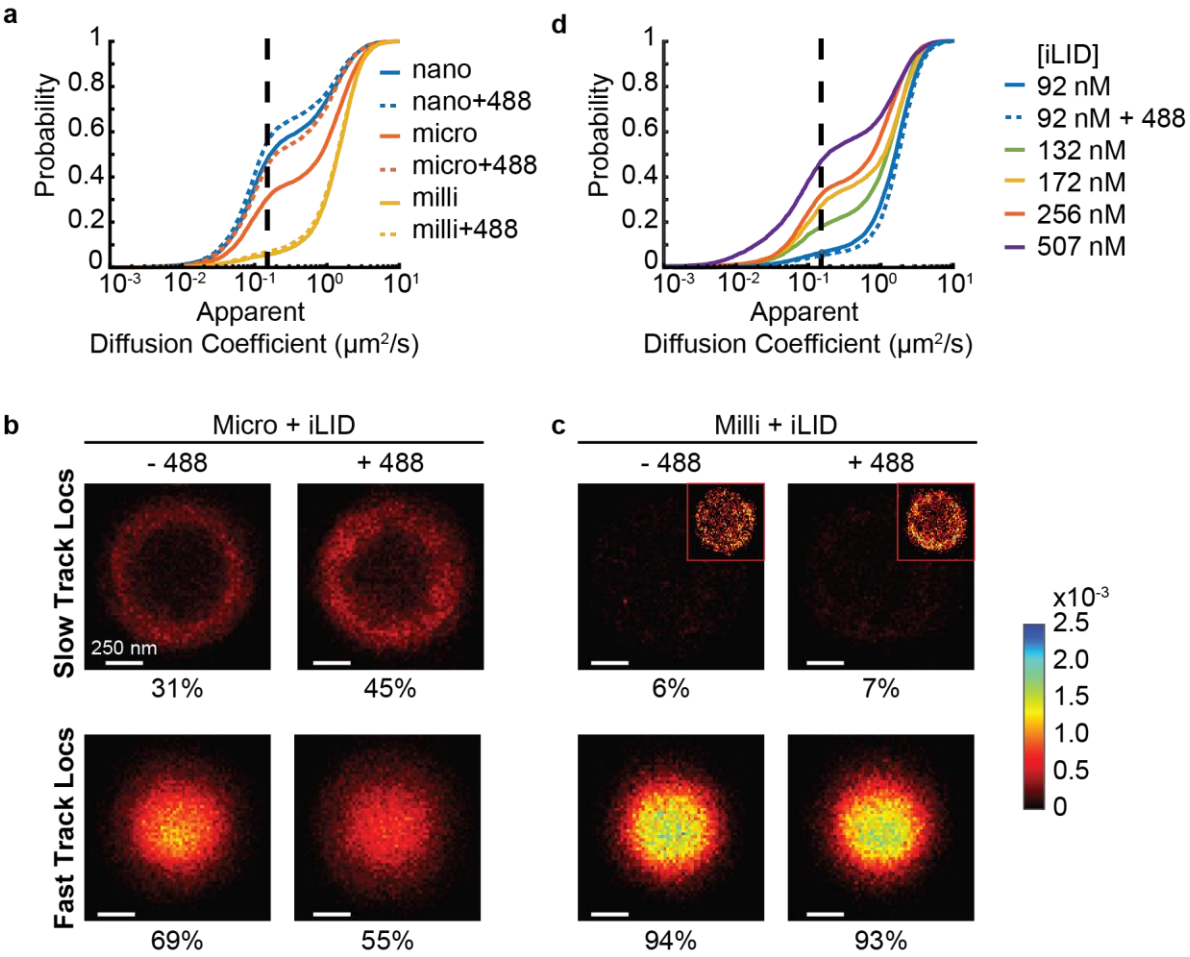

Figure 4.5. Affinity of the SspB:iLID interaction determines the fraction of iLID-associated SspB observed in single-molecule tracking experiments. (a) Apparent diffusion coefficient distributions for three SspB mutants. The lowest affinity mutant, $SspB_{milli}$ (solid, yellow line, N = 4246 tracks, 65 cells) displays the highest population fraction of fast, cytosolic diffusion prior to 488 nm illumination, followed by $SspB_{micro}$ (solid, orange line, N = 7,738 tracks, 97 cells) and $SspB_{nano}$ (solid, blue line, N = 8,542 tracks, 78 cells). Activation of these systems with 488 nm illumination (dashed line distributions) shifts each mutant protein's distribution towards larger fractions of slow diffusing molecules due to MA-iLID association. **(b)** 2D cross-sectional histograms of $SspB_{micro}$ trajectories indicate MA-iLID association at the membrane increases in frequency upon 488 nm illumination (N = 6,491 tracks, 77 cells). Each histogram is normalized to the total number of molecules observed in that experiment. Inset: rescaled (unnormalized) histograms, shown for clarity. **(c)** 2D cross-sectional histograms of $SspB_{milli}$ trajectories indicates small, but qualitatively discernable MA-iLID association after 488 nm illumination (N = 5243 tracks, 99 cells). **(d)** Apparent diffusion coefficient distribution of $SspB_{micro}$ as a function of MA-iLID expression level. Higher MA-iLID expression levels lead to increased population fractions of slow, membrane-proximal diffusion of $SspB_{micro}$ (see also **Figure 4.7** and **4.9**)

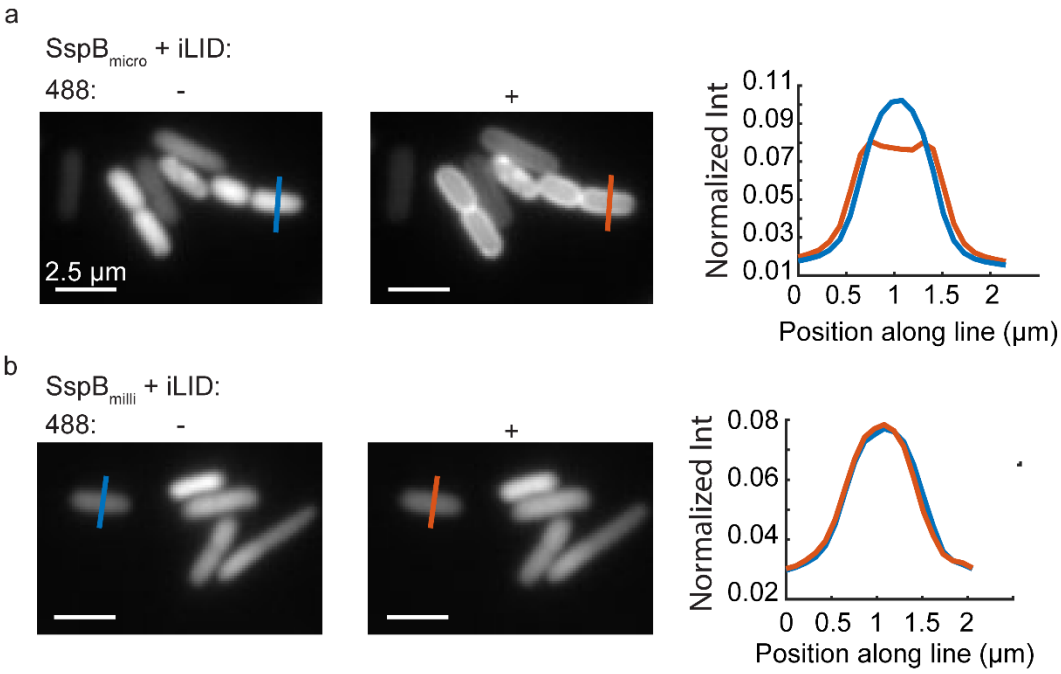

Figure 4.6. Diffraction-limited images of SspB affinity mutants. (a) Diffraction-limited images of SspB$_{micro}$ show robust redistribution of fluorescence from the cytosol to the membrane upon 488 illumination. Normalized fluorescence line-profile information show distinctive line shapes consistent with cytosolic and membrane-proximal fluorescence before and after 488 nm illumination. **(b)** Diffraction-limited images of SspB$_{milli}$ do not indicate changes in fluorophore spatial distribution upon 488 nm illumination.

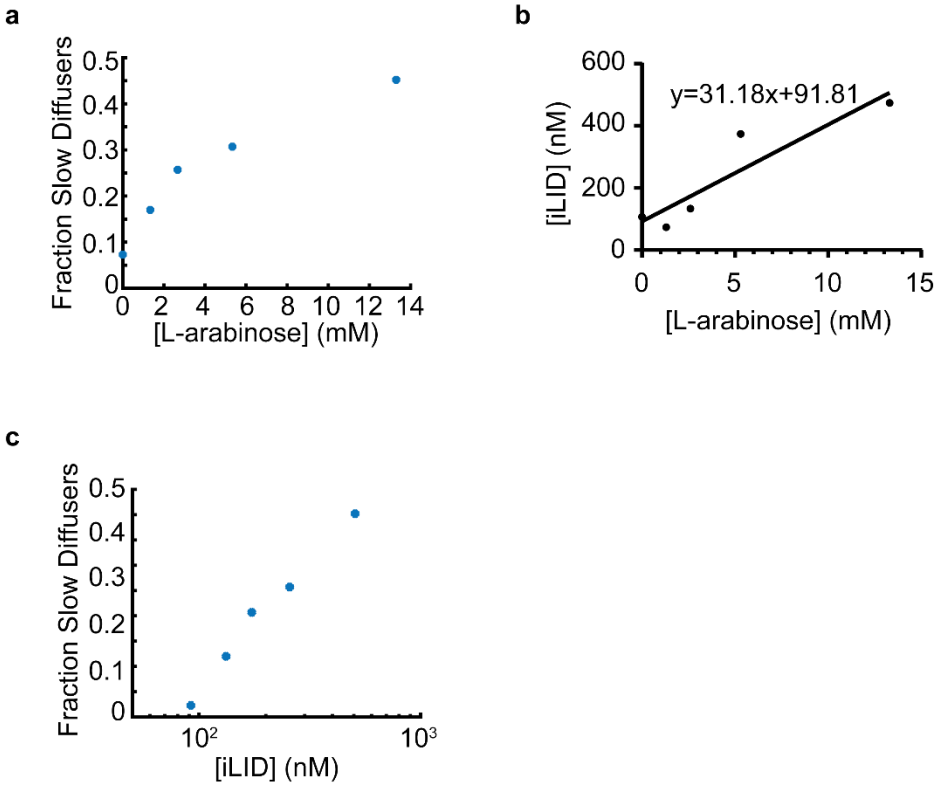

Figure 4.7. The fraction of slow-diffusing, iLID-associated $SspB_{micro}$ is dependent on the expression level of MA-iLID. (a) The fraction of slow diffusing $SspB_{micro}$ as a function of L-arabinose induction concentration derived from single-molecule tracking data. **(b)** The concentration of MA-mCherry-iLID as a function of L-arabinose concentration. The number of MA-iLID molecules was estimated by dividing initial total cell intensity of MA-mCherry-iLID expressing cells by the measured, average intensity of a single mCherry emitter. The data were fit to a line to estimate the MA-iLID concentrations as a function of L-arabinose induction concentration. **(c)** The fraction of slowly diffusing $SspB_{micro}$ derived from single-molecule tracking data as a function of iLID concentration.

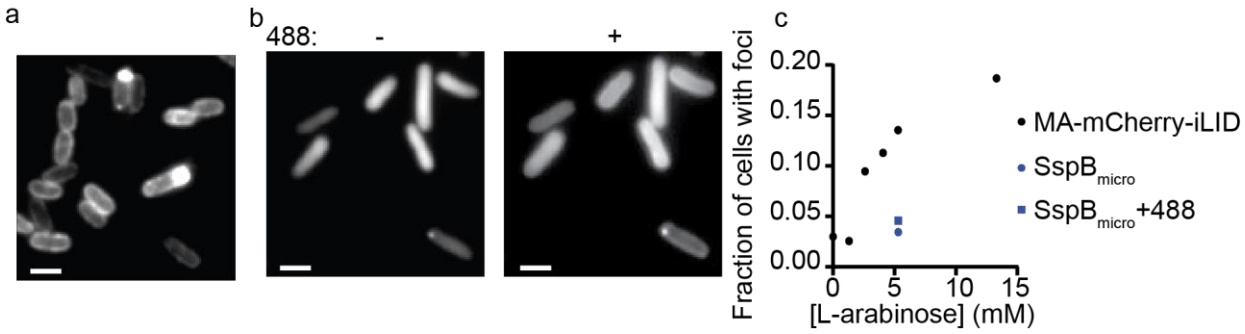

Figure 4.8. Expression level dependent fluorescent foci formation of MA-mCherry-iLID and SspB$_{micro}$. **(a)** Diffraction-limited images of MA-mCherry-iLID expressing cells (5.33 mM L-arabinose). Fluorescent foci formation is evident in a subset of cells. **(b)** Diffraction-limited images of SspB$_{micro}$ co-expressed with MA-iLID (5.33 mM L-arabinose) before and after 488 nm illumination. **(c)** Quantification of the fraction cells with foci. 2 µm scale bar. (N = 618, 321, 81, 604, 445 cells for 0, 1.25, 2.5, 5.33, and 13.3 mM L-arabinose induction levels, respectively; N = 88 cells for SspB$_{micro}$ + MA-iLID – pre and post 488 nm illumination).

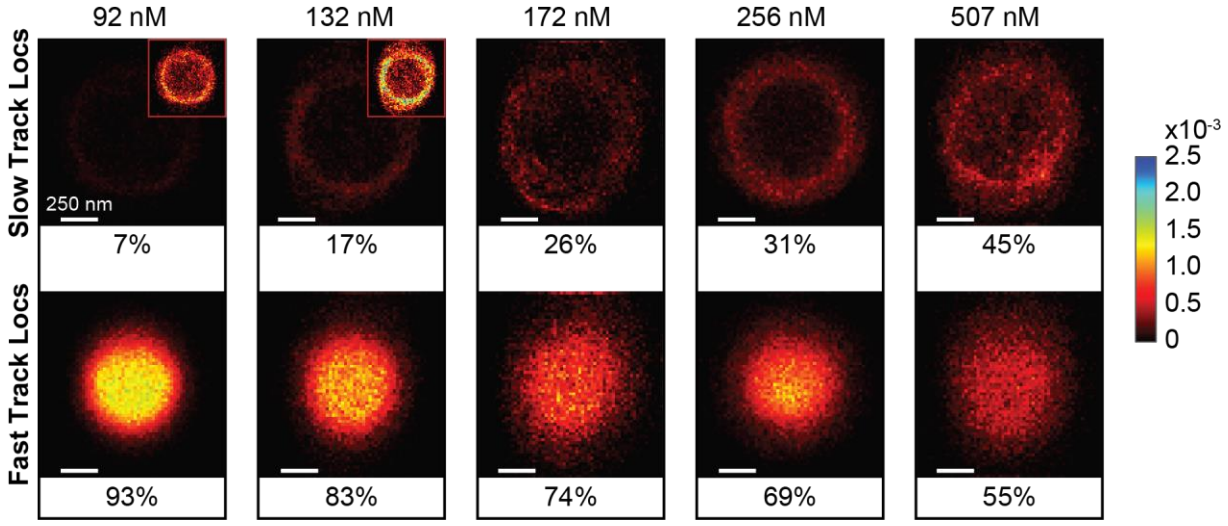

Figure 4.9. Expression level of MA-iLID is directly correlated with fraction of slow diffusers and iLID-association. 2D cross-sectional histograms of $SspB_{micro}$ single-molecule trajectories indicates increased probability of slow diffusion at the cell membrane as MA-iLID expression level is increased. Each histogram is normalized to the total number of molecules observed in that experiment. Inset: rescaled (unnormalized) histograms, shown for clarity. Inset histograms are rescaled versions of the full-size histogram, set to maximum values of $2.0x10^{-4}$ and to $3.0x10^{-4}$ for 92 nM and 132 nM expression levels, respectively.

4.2.4 Cumulative displacement analysis identifies state-switching events in full-length trajectories

Having quantified the dissociation constant of the iLID:SspB interaction, we next sought to determine the kinetics of this interaction. Previous analyses were performed on trajectories which were shortened to contain at most 10 displacements, to prevent averaging over multiple states. Because our data sets contained many long trajectories, we reasoned that some of these trajectories may contain information about the length of time a single SspB protein remains bound to an MA-iLID protein at the membrane. To assess the diffusive behavior over the course of a trajectory, we first calculated the cumulative displacement of each single-molecule over time **(Figure 4.10a** and **4.10b**, see methods). These data show a clear separation for fast cytosolic diffusion and slow, membrane-associated diffusion. Because of the clear distinction, we decided that analysis cumulative displacements could be used to differentiate states within single trajectories. To estimate

the diffusion coefficients that describe motion in each state, we simulated cytosolic and membrane-bound diffusion at different diffusion rates. We found that the cumulative displacement over time of single-molecule trajectories simulated at 5.5 $\mu m^2/s$ in the cytosol and 0.2 $\mu m^2/s$ at the membrane best matched the experimentally measured cumulative displacement data. These values were then used as references for subsequent analysis.

To identify state switching events within trajectories, we employed the workflow outlined in Figure 4a and c. Briefly, the cumulative displacements of small segments within trajectories were designated as fast diffusion or slow diffusion using a threshold corresponding to D = 1.75 $\mu m^2/s$. This threshold was chosen to match the upper-limit of the displacement sizes used in the membrane-bound simulation at 0.2 $\mu m^2/s$. Trajectories which exhibited subsequent fast-slow-fast diffusive states were ranked by evaluating the similarity of experimental slope of cumulative displacement data to the abovementioned simulated slopes of cumulative displacement data corresponding to D = 5.5 $\mu m^2/s$ and 0.2 $\mu m^2/s$ (**Figure 4.10d**). We further verified that the best scoring trajectories indeed exhibited slow-diffusing segments at the membrane, and fast-diffusing segments in the cytosol. The resulting subset of trajectories was then used to calculate t_{bound} (**Figure 4.10e**). As a control, we performed the same analysis for SspB trajectories in the absence of MA-iLID, and, as expected, did not identify clear state switching signatures.

In the presence of 256 nM MA-iLID, $SspB_{micro}$ and $SspB_{nano}$ exhibit similar bound times independent of 488 nm illumination (median = 300 and 350 ms, respectively) while $SspB_{milli}$ displayed comparatively shorter binding times (median = 175 ms) (**Figure 4.10e**). Thus, the measurements of t_{bound} made in this manner do not show a trend that clearly

correlates with each SspB mutant's affinity for the iLID protein or with photoactivation of iLID. Trajectories which were identified as acceptable for residence time measurements were rare (<1% or less of the total number of trajectories analyzed). This low number stands in stark contrast to the much larger fraction of molecules which remained iLID-bound for the duration of the trajectory which matched the trend observed in the analyses of apparent diffusion coefficients (**Figures 4.3, 4.5 and 4.11**). The length of the trajectories of fully-bound molecules ranges from 0.3 seconds up to 3 seconds (longest observed trajectory – **Figure 4.10b**). The long lengths of these trajectories (which are terminated by fluorophore photobleaching) suggest that $SspB_{micro}$ proteins can remain iLID-bound for much longer than the median time scales estimated for t_{bound}. Previously published data estimates the dissociation half-life of $SspB_{nano}$ and $SspB_{micro}$ with iLID to occur on the order of minutes[159,160]. Thus, single-molecule trajectories are not long enough to capture both binding and unbinding events of stable SspB:iLID interactions. These results suggest that short time scale interactions that we capture are representative of a transient binding mode(s) which is(are) not reflective of stable SspB:iLID binding.

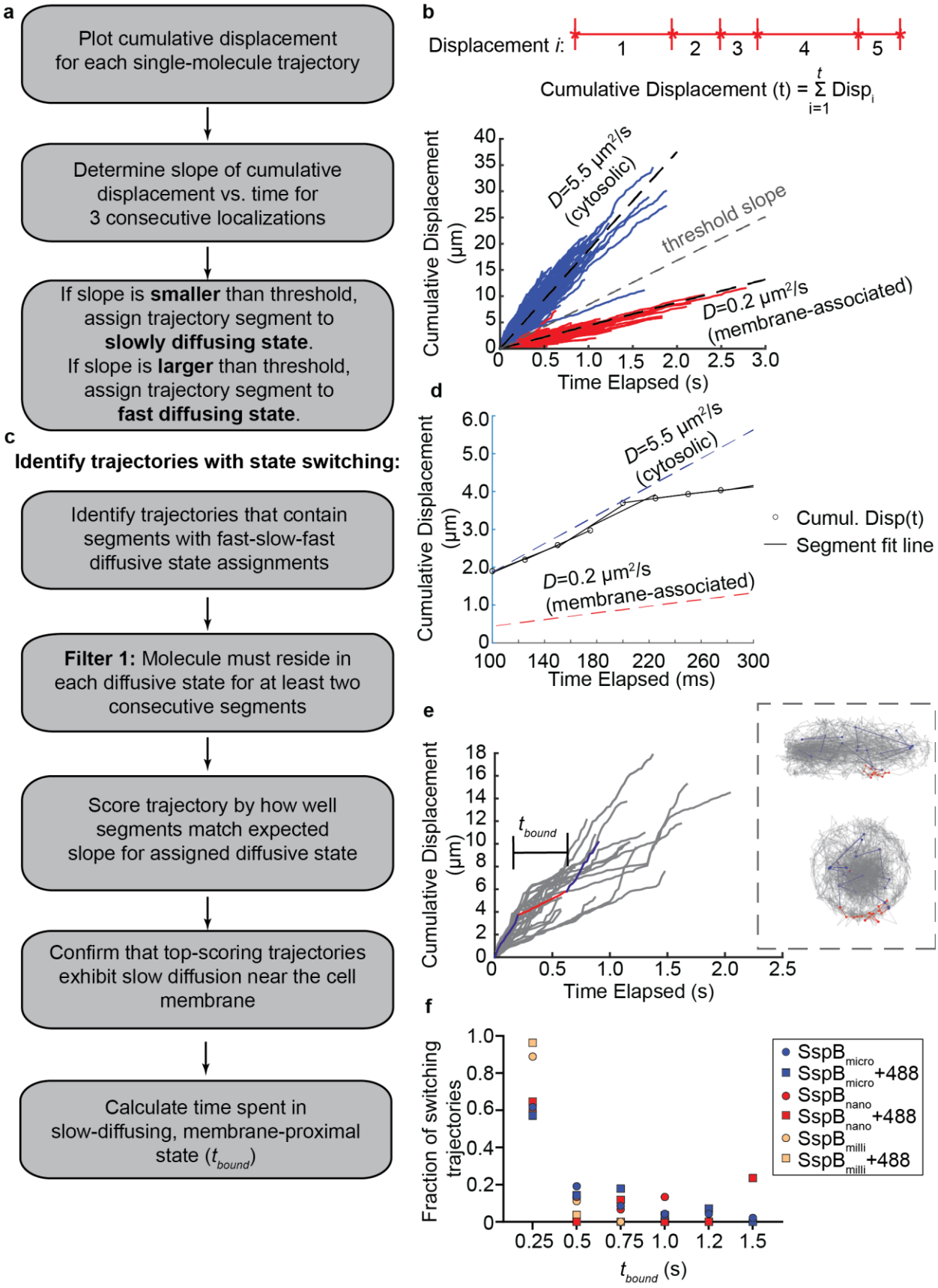
a
Plot cumulative displacement for each single-molecule trajectory
Determine slope of cumulative displacement vs. time for 3 consecutive localizations
If slope is **smaller** than threshold, assign trajectory segment to **slowly diffusing state**.
If slope is **larger** than threshold, assign trajectory segment to **fast diffusing state**.
c
Identify trajectories with state switching:
Identify trajectories that contain segments with fast-slow-fast diffusive state assignments
Filter 1: Molecule must reside in each diffusive state for at least two consecutive segments
Score trajectory by how well segments match expected slope for assigned diffusive state
Confirm that top-scoring trajectories exhibit slow diffusion near the cell membrane
Calculate time spent in slow-diffusing, membrane-proximal state (t_{bound})
b
Displacement *i*: 1 2 3 4 5
Cumulative Displacement (t) = $\sum_{i=1}^{t}$ Disp$_i$
Cumulative Displacement (μm)
D=5.5 μm²/s (cytosolic)
threshold slope
D=0.2 μm²/s (membrane-associated)
Time Elapsed (s)
d
Cumulative Displacement (μm)
D=5.5 μm²/s (cytosolic)
D=0.2 μm²/s (membrane-associated)
Cumul. Disp(t)
Segment fit line
Time Elapsed (ms)
e
Cumulative Displacement (μm)
t_{bound}
Time Elapsed (s)
f
Fraction of switching trajectories
SspB$_{micro}$
SspB$_{micro}$+488
SspB$_{nano}$
SspB$_{nano}$+488
SspB$_{milli}$
SspB$_{milli}$+488
t_{bound} (s)

Figure 4.10. Cumulative displacement analysis identifies state-switching events in single-molecule trajectories. (a) Workflow of cumulative displacement analysis to distinguish fast, cytosolic diffusing molecules from slow, membrane-associated molecules. **(b)** Top panel: Schematic of displacement data transformed into a 1D trajectory to illustrate displacement size over time. The cumulative displacement is the sum of all displacements up to a given time point, *t*. Bottom panel: Cumulative displacement over time for $SspB_{micro}$ trajectories collected in MA-iLID expressing cells (256 nM) in unactivated conditions. A threshold slope corresponding to D = 1.75 $\mu m^2/s$ was used to distinguish fast diffusing molecules (blue) from slow diffusing molecules (red). Simulated trajectories in the cytosol at 5.5 $\mu m^2/s$ and in the membrane at 0.2 $\mu m^2/s$ recapitulated experimental cumulative displacement slopes and were used as reference slopes in the following steps. **(c)** Workflow used to identify trajectories with state-switching (see text for details). **(d)** Example of a $SspB_{micro}$ partial trajectory which exhibits state-switching. Three consecutive cumulative displacements are fit to a line, and the slope is compared to the threshold slope to classify the trajectory segment as cytosolic or membrane-bound. The slope of the segment is then compared to the reference slope for cytosolic diffusion or membrane diffusion depending on the state assignment, and scored by how closely they match. Trajectories with at least 2 consecutive segments in cytosolic and then membrane-associated states (or vice versa) are categorized as state-switching and used for later analysis. **(e)** Cumulative displacements over time of trajectories which show state transitions of fast-slow-fast. Trajectory localization of example fast(blue)-slow(red)-fast(blue) state-switching cumulative displacement plotted to highlight state transition at the membrane of the cell. Time spent in bound state (red portion of trajectory) is integrated

to calculate the residence time t_{bound}. **(f)** Histogram of residence times of SspB affinity mutants (bin size = 250 ms) indicate that transient binding modes to MA-iLID do not exhibit residence times that are dependent on the affinity of the SspB:iLID interaction.

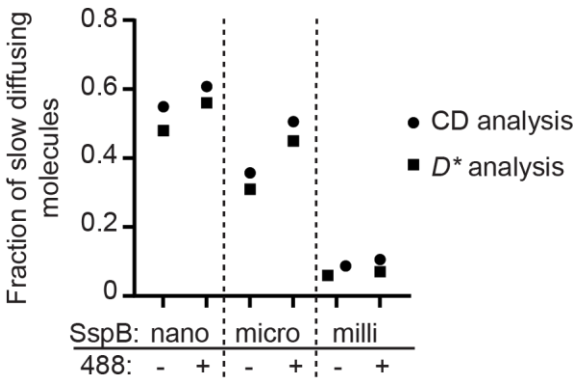

Figure 4.11. Fraction of slow diffusing molecules which stay bound for the duration of the trajectory in cumulative displacement (CD) analysis compared to fraction of slow diffusing molecules observed in apparent diffusion coefficient analysis (*D**). See main text figure captions for description of trajectory and cell numbers.

4.3 Conclusions

Here, we provide a quantitative analysis of the iLID optogenetic system in live K12 *E. coli* cells using 2D diffraction-limited imaging and 3D single-molecule tracking. We show that the iLID system enables efficient optogenetic manipulation of protein spatial distributions when used in conjunction with diffraction-limited imaging. Single-molecule tracking data acquired using high intensity 561 nm laser excitation leads to a substantial amount of SspB:iLID interaction even in the absence of optogenetic activation at 488 nm. This suggests that increased photon flux is somehow able to activate the iLID optogenetic response, even though the LOV2 domain absorption spectra suggest that wavelengths

greater than 500 nm should not be absorbed[112]. This conclusion is consistent with our observation that even low intensity 514 nm illumination is able to increase the SspB:iLID interaction. However, published LOV2 domain absorption spectra were collected using purified proteins[112]. It is possible that cellular contents, proximity to the membrane and imposed steric hindrance results in a shift in iLID conformational dynamics and thus a change in interaction with SspB. A similar effect has been seen in other model systems utilizing the iLID:SspB interaction[159,160]. This may explain the rare, transient binding events that we measured in single- molecule trajectory analyses. Our results highlight the importance of calibrating the effects of illumination conditions and cellular environment when the iLID system, or any optogenetic system, is used to modulate an SspB-tagged protein's spatial distribution.

A notable advantage of optogenetic systems, such as iLIDs, is that dimerization can be induced in real time using light. Optically-induced dimerization can be enabled much faster than chemically induced dimerization, which are diffusion-limited. We aim to combine optogenetic perturbation with single-molecule tracking to deplete cytosolic diffusive states that have been assigned to hetero-oligomeric protein complexes based on control experiments in genetically perturbed backgrounds. Although a pre-activated system dampens the magnitude of the optogenetic response that can be observed, highly sampled distributions obtained from tens of thousands of single-molecule trajectories, may allow for the observation of cytosolic diffusive states depletion with sufficient statistical power. Additionally, titration of protein expression can be used to incrementally sequester proteins of interest. Another alternative might be to use far-red excitable fluorophores for single-

molecule tracking. Based on the trends observed here we speculate that high intensity red and far-red light illumination will not activate the iLID system. Thus, single-molecule localization and tracking microscopy with red and far-red fluorophores could enable observations of large optogenetic responses, similar to those observed in diffraction-limited imaging.

4.4 Materials & Methods:

4.4.1 Bacterial strains and plasmids

Escherichia coli K12 (MG1655) strains were generated by introducing pACYC and pBAD vectors containing genes encoding the cytosolic prey protein, SspB, and the membrane-anchored bait protein, iLID, respectively. pACYC $SspB_{nano}$-Halo was derived from pACYC $SspB_{nano}$-mCherry (pFL109) which was a gift from Andreas Diepold. The construct was modified by removing mCherry from the plasmid via restriction digest and the *halo* coding sequence was ligated in its place, using XhoI and SalI cut sites. The plasmid containing the bait protein, pBad FLAG-iLID (pFL108), also a gift from the Diepold lab, was transformed into bacteria without any further modification.

4.4.2 Cell culture

E. coli cultures were inoculated from a freezer stock and grown overnight in LB media at 37° C and shaking at 225 rpm. Strains expressing from the pACYC and pBAD plasmids were grown in 30 µg/mL chloramphenicol and 100 µg/mL ampicillin, respectively. Overnight cultures were diluted to an OD_{600} of 0.05 in M9 minimal media and incubated at 37° C. Strains containing the pBAD plasmid were induced with 5.33 mM L-arabinose after 2 hours unless indicated otherwise. After an additional 1.5 hours of

growth, 1.5 mL of cell culture was aliquoted and stained with 1.5 µL of 500 µM JFX-549 dye. The cell suspension mixture was incubated at 37° C for 30 minutes and then washed four times with M9 minimal media. Cell pellets were resuspended in a final volume of 10 µL for use in imaging experiments.

E. coli cells were transformed with plasmids via heat shock of chemically competent cells. Transformed cells were selected for by growing on LB agar plates containing chloramphenicol, ampicillin (100 µg/mL), or a combination of both for co-expressing strains. Transformants were screened by performing a Western blot for FLAG or Halo proteins in pBAD and pACYC-containing strains, respectively. Strains which showed a clear band in Western blot experiments were used to make freezer stocks containing 15% glycerol.

4.4.3 Optical setup

Imaging of cells was performed on a home-built inverted fluorescence microscope as described previously[50]. The microscope was modified for use in optogenetics experiments by incorporation of an additional 488nm laser line (Coherent Genesis) for activation of the iLID system. Fluorescence images were collected in the "red" channel of the imaging system.

4.4.4 Epifluorescence imaging

Stained cells were mounted on a #1.5 coverslips (VWR) and immobilized using 1.5% agarose pad prepared in M9 minimal media. Halo-conjugated JFX549 was excited using 561 nm laser light at ~1 W/cm^2. Images were acquired at 5 frames/sec for 40 seconds

pre- and post-activation of the iLID optogenetics system. The iLID optogenetic system was activated using 488 nm laser light at ~4 mW/cm^2 continuously for 2 minutes prior to and then also during acquisition of post-activation images. Epifluorescence images shown in the figures represent averages of these image sequences. Brightfield images were acquired of the same field-of-view by illuminating cells with an LED, and taking a single 25 ms exposure.

4.4.5 SSIM analysis of Diffraction-limited images

Pre- and post- activation images were background subtracted. Outlines of cells were derived by using OUFTI[121] on inverted color to create a binary mask such that each cell was compared to itself before and after activation. The built-in Matlab (The MathWorks, Inc, Natick, Massachusetts) function ssim() was applied to the masked images with equal weighting of the comparison metrics, luminance, structure, and contrast, to assess the degree of image similarity. Cells with abnormal morphology (based on the associated brightfield image) were excluded from the analysis. Multiple fields of view were acquired for each condition, and the experiments were replicated twice.

4.4.6 Super-resolution fluorescence imaging

Fluorescent fiducial markers (Invitrogen) were added to cell suspensions and the cell suspension was then mounted on #1.5 glass coverslips. Cells were immobilized using solidified pads of 1.5% agarose in M9 minimal media. Halo-conjugated JFX-549 was excited into the blinking state by 561 nm laser light at ~2 kW/cm^2 at the sample. Images were acquired at 40 frames/sec in the presence or absence optogenetic activating 488 nm

light. Cells were activated using 488 nm laser light at ~4 mW/cm^2 continuously for 2 minutes prior to and during acquisition of post-activation images.

4.4.7 Data Processing

Raw data was processed in Matlab (The MathWorks, Inc, Natick, Massachusetts) using a modified version of easy-DHPSF software[50,120]. Fluorescent fiducial markers were used for sample drift correction. Single-molecule localizations were registered to phase contrast images using a two-step affine transformation in MATLAB as previously described[50]. Localizations outside of cells were discarded from further analysis using axial bounds and OUFTI-derived cell outlines which were generated from phase contrast images, as described above.

4.4.8 Single-molecule tracking analysis

To derive single-molecule displacements, localizations in subsequent frames were linked into trajectories. A maximum linking distance of 2.5 um was used for linking analysis, and multiple localizations which were present at the same time within a single cell were discarded to prevent misassignment of molecules.

The Mean Squared Displacement (MSD) for each trajectory was calculated using

$$\mathrm{MSD} = \frac{1}{(N-1)} \sum_{n=2}^{N} (x_n - x_{n-1})^2$$

where *x* is the 3D position at timepoint *n*, including up to 11 timepoints for calculating the mean over 10 displacements. The remainder of the trajectory was not used in the MSD

analysis to ensure multiple diffusive states were not averaged over. The MSD measurement was then used to calculate the apparent diffusion coefficient (D^*) according to:

$$D^* = \frac{\mathrm{MSD}}{2 \cdot m \cdot \Delta t}$$

where m is the dimensionality of the measurement (m=3 for the 3D trajectories reported here), and Δt is the camera exposure time used for imaging (Δt=25 ms under our conditions).

4.4.9 2D-cross section projection analysis

The vector describing the central axis of each cell was determined using the cell outline generated from OUFTI. The outline was segmented into sections along the cell length, and localizations from trajectories in each section were projected onto a 2D plane. The position of the central cell axis was adjusted to match the centroid of all localizations within the section. Positions of localizations from each cell were scaled to match the mean cell radius and mean cell length which was calculated from OUFTI outlines. The trajectories were classified as slow or fast diffusing using the threshold D^* = 0.15 μm^2/s which was determined by identifying a transition point from the first major change in slope in the CDF plot of apparent diffusion coefficients of data containing both iLID-associated and cytosolic diffusion (**Figure 4.2**).

4.4.10 Determination of residence times - t_{bound}

To identify diffusive state transitions in single-molecule trajectories, we developed a workflow to analyze displacement data over time (**Figure 4.10a and c**). First, we plotted the additive, or cumulative displacement (CD) as a function of time elapsed according to:

$$\mathrm{CD}(t) = \sum_{t=1}^{N} \sqrt{(x_t - x_{t-1})^2}$$

where *x* is the 3D position at timepoint *t*. The CD was calculated for each displacement, for the full trajectory length (N).

The instantaneous rate of displacement was estimated by finding the slope within a small, sliding window containing 3 displacements for the full length of the trajectory (**Figure 4.10d**). The size of the sliding window was chosen to be small enough such that switching events were not excessively averaged over, while being large enough to be somewhat insensitive to displacement size fluctuations. Each segment of the trajectory was then classified as bound or free by calculating its slope and comparing it to a threshold, which was chosen to match the upper-limit of the displacement sizes used in the membrane-bound simulation at 0.2 $\mu m^2/s$. Trajectories which contained consecutive segments of fast-slow-fast state assignments were used for further analysis because of the presence of an internal bound state. To be considered for analysis, the molecule must reside in each state for at least 2 segments (4 displacements) of the trajectory to ensure that the identified state change was a true diffusive state change and not due to random fluctuation. Each switching trajectory was ascribed a score (TS) by how well the slope of trajectory

segments matched simulated diffusion coefficient slopes derived for freely diffusing, cytosolic and membrane-bound molecules:

$$TS = \frac{1}{N_{seg} - 2} \sum_{i=1}^{N_{seg}} e^{-|m_i - m_s|}$$

where m_i is the slope fit to the experimental trajectory segment, and m_s is the slope derived from free cytosolic or membrane-bound simulated data, depending on the state assigned to the trajectory segment. N_{seg} refers to the number of segments in the trajectory. Switching trajectories were ranked by their TS, and the top-scoring trajectories (TS>~0.16) were inspected individually to verify that switching events occurred at the membrane of the cell. The residence time (t_{bound}) of bound molecules in these switching trajectories was calculated by determine the number of displacements the molecule was assigned to the bound state.

4.4.11 3D single-molecule trajectory simulation

Cytosolic trajectories were simulated as described previously.[49,50] Briefly, Monte Carlo simulations of Brownian motion at 5.5 μm^2/s were confined to the volume of a cylinder matching the dimensions of K12 *E. coli* (radius = 0.5 μm, length = 2.5 μm). Initial positions of molecules were randomly selected to uniformly fill the volume of the cell, and subsequent positions in the trajectory were selected at 100 ns intervals for a total of 125 ms. We simulated noisy, motion-blurred images of the single-molecule trajectories, integrating images over subsequent 25 ms time intervals, to match experimental camera

exposure times for a total of 6 images per single-molecule track. We simulated 1000 such trajectories. To best match data derived from experimental conditions, we analyzed the simulated images of trajectories in the same way described for experimental localization and tracking. Easy-DHPSF software was used to analyze the images and detect single-molecule localizations.

Membrane-bound trajectories were simulated for molecules diffusing at 0.2 $\mu m^2/s$. Initial positions were randomly chosen on the surface of a spherocylinder matching the dimensions of K12 *E. coli* (radius = 0.5 μm, length = 2.5 μm). Monte Carlo simulations of molecular motion were confined to the surface of the spherocylinder by translating displacements to changes in lateral position and elevation angle on the cylindrical surface or elevation and azimuthal angle on the hemispherical surface, such that the distance from the cell axis is always equal to the radius of the cell. Positions were updated at 100 ns intervals for a total of 125 ms. Images were generated and analyzed as described in the previous paragraph.

4.4.12 2D diffraction-limited image simulation

Trajectories of cytosolic and membrane-associated diffusing molecules were simulated as described above with the following modifications to match diffraction-limited imaging conditions. Positions were sampled every 1 μs for a total of 1.2 seconds. Molecule positions were sampled ever 200 ms, resulting in 6 localization positions (macro-positions) per track.

The three dimensional molecule macro-positions were used to generate conventional diffraction-limited 2D point-spread functions of isotropic emitters using a

vectorial light propagation model.[116] We modified the algorithm to omit the double helix phase mask and optical aberrations. In the simulation, the nominal focal plane was positioned at the center of the cell. A total of 10,000 trajectories were simulated for both cytosolic and membrane-bound molecules, providing 60,000 total emitter positions in each condition. Images obtained for each emitter were added to attain the total image. To attain mixed population images, trajectories were chosen at random from the total simulated trajectory population to reflect the specified membrane-associated molecule fraction.

CHAPTER 5:

SIGNIFICANCE &

FUTURE DIRECTIONS

5.1 Significance

Single-molecule microscopy has revolutionized cell imaging. It effectively bridges the gap between live-cell compatible, yet diffraction-limited fluorescence microscopy and fixed-cell or purified protein imaging with atomic-level resolution of X-ray crystallography and cryo-electron microscopy. SMLM has enabled resolution of static cellular structures [16,101,102,129,161-163]. The field is ever-growing since its inception in the 1990s and new advancements continue to push the field forward, including innovative labeling techniques[14], development of expansion microscopy (ExM) [164-166] in 2015, and MINFLUX microscopy in 2017[167].

Perhaps a more challenging extension of SMLM is resolving dynamic structures and protein complexes. Distinguishing different diffusive states and assigning them to biologically relevant complexes requires significant statistical power and biological experimental controls. Fitting of analytical equations[39-44] and Hidden Markov models[45,46,48], implementation of machine learning[168,169], and simulated curve fitting[49,103,119] are some examples of the statistical methods used for resolving diffusive states from tracking data. Further, perturbations of possible interactions are required for validating these assignments. However, manipulating these interactions through mutation or chemical treatment of cells often results in unforeseen complications[149,150]. Therefore, the use of a non-invasive, transient perturbation is advantageous.

Here, we explore the use of light-inducible dimerization as a means to transiently perturb protein spatial distribution[76], and thereby, diffusive behavior. I have benchmarked the performance of the iLID optogenetic system in both conventional, diffraction-limited imaging methods, and in 3D single-molecule tracking microscopy. In this way, I have

quantified dimerization of the iLID system in different imaging conditions and shown that the iLID system is sensitive to high photon flux at wavelengths that show minimal absorption in previously published results of *in vitro* assays. Further, I have extended the Gahlmann lab single-molecule analysis toolbox to include membrane-associated diffusion of molecules, and analysis of long trajectories which was integral for quantifying the dimerization response of the iLID system. Implementation of these analyses into our routine workflow will expand the systems that we can study.

5.2. Future Directions

The quantification that I have performed of iLID system dimerization opens the door to new analyses and asks questions that have not been previously addressed. To start, future work can focus on applying the iLID system to studying and verifying protein-protein interactions.

5.2.1. Distinguishing protein complexes using knocksideways assays

To date, our lab has focused on characterizing assembly of the virulence-associated bacterial type 3 secretion system (T3SS). T3SS-mediated infections are an integral mode of virulence of many pathogens[170-172] and result in over one million human deaths each year worldwide[173,174]. T3SSs consist of more than 20 different membrane-embedded and cytosolic proteins[173-175]. The most prominent feature of the T3SS injectisome is a long-hollow needle complex that spans both the inner and outer bacterial membranes and protrudes up to ~70 nm into the extracellular space (**Figure 5.1**). Upon host cell contact, the tip of the needle is stably anchored into the host cell membrane by a translocation pore, so that effector proteins (virulence factors that alter host cell biology) can be secreted directly into the host cell cytoplasm. A key feature of T3SS assembly and function is that

secretion substrate selectivity follows a strict temporal hierarchy: Proteins forming the needle are early secretion substrates, translocation pore proteins are middle secretion substrates, and effector proteins are late secretion substrates. While effector proteins differ among bacterial species, the structural proteins of the T3SS injectisomes are highly conserved, making T3SSs broadly relevant and widely applicable protein delivery machines[173,176]. There is evidence that suggests that the cytosolic proteins, SctK, SctQ and SctL, that are peripherally associated with the membrane-embedded structure are important for both assembling the full T3SS structure, and also for distinguishing between early, middle, and late secretion substrates[177,178]. Because conventional biochemical and imaging techniques lack native, live-cell conditions or do not have spatial or temporal resolution required to resolve fast diffusing protein complexes, it remains unknown how the cytosolic protein complex distinguishes between secretion substrates, and further, how the cytosolic complex assembles. Understanding assembly of the T3SS may increase the efficacy of rational design of antivirulence drugs, a need which is ever-growing due to increased anti-microbial drug resistance.

The Gahlmann lab has directly addressed the aforementioned challenges by leveraging the live-cell compatible, high spatio-temporal resolution of single-molecule localization and tracking microscopy. By tracking fluorescently labeled cytosolic T3SS proteins in different genetic backgrounds, we have identified distinct cytosolic complexes through rigorous statistical analyses in the enteropathogen model *Yersinia enterocolitica*[50,103]. Specifically, subcomplexes containing SctQLN and SctLN, in the absence of SctQ, have been identified and assigned to specific diffusive states using single-

molecule tracking analyses (**Figure 5.1**). For a complete discussion of how diffusive state are assigned to distinct protein complexes, refer to the introduction in Chapter 1.

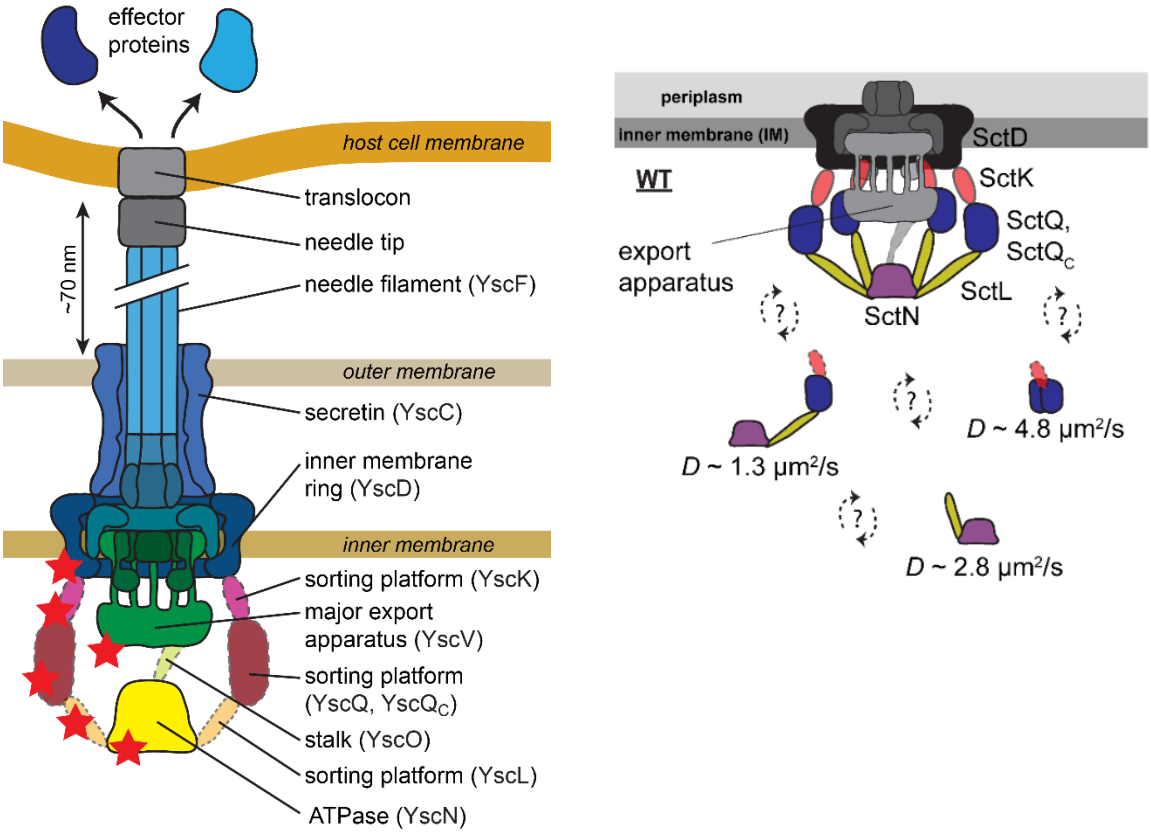

Figure 5.1. Structure and dynamic assembly of the Type 3 Secretion System. (left) Cross-section of the T3SS structure. Cytosolic proteins marked by red stars have been fluorescently tagged and are available for tracking analyses. Figure adapted from reference[179]. (right) The cytosolic T3SS proteins dynamically associate with the membrane-embedded injectisome[180]. Cytosolic protein complexes were assigned to distinct diffusive states using single-molecule tracking microscopy. Figure was reproduced from Prindle et al. (2022)[103].

An intuitive way to validate diffusive state assignments to specific protein complexes is to disrupt the putative complexes and measure changes in diffusion behavior. Our lab is currently identifying potential amino acid residues required for maintaining protein-protein interactions within the SctQNL complex. By performing diffusion analysis on interaction mutants, we expect to observe depletion, or a complete absence of, the diffusive state which describes the oligomerized complex. The work presented in this dissertation provides an alternative approach that allows for transient manipulation of protein spatial localization to ultimately change the diffusive behavior of the protein-of-interest non-invasively. Thus, one can deplete a diffusive state by disrupting the native spatial distribution of a protein-of-interest and sequestering, or "knocking sideways", the protein to another cellular compartment such as the cell membrane using light signals. Common light integrating systems, also called optogenetic systems, utilize light induced dimerization of two proteins as optically controlled switches. In knocksideways assays, one half of the dimer pair is localized to a specific cellular compartment using a localization signal, and the second half is used to genetically tag a protein-of interest. Upon light-stimulation at a wavelength appropriate for the specific optogenetic system, the dimer pair will oligomerize, and the tagged protein will be sequestered to the site of interaction.

I have shown that optimization of the iLID system is possible in bacteria through implementation of mutants that attenuate the binding affinity of the optogenetic dimer pair, and titration of relative protein expression. Thus, the iLID system may be a proper tool for validating the putative SctQNL and SctNL cytosolic complexes of the T3SS. I designed an experiment which applies the iLID system to the T3SS proteins, and directly tests if whether SctQ and SctL are interacting in cytosolic complexes. In this assay, SctQ is tagged

with the cytosolic optogenetic component, SspB, while the optogenetic binding complement, iLID, is localized to the bacterial inner membrane. After illumination with 488 nm light, iLID undergoes a conformational change and allows for binding of SspB, which will sequester the protein-of-interest cargo, SctQ, to the membrane. The Diepold lab, a close collaborator, has shown that blue-light dependent sequestration of SctQ to the membrane is possible using the iLID optogenetic system, and that SctQ sequestration to the iLID protein reduces the functionality of the T3SS (**Figure 5.2b** and **c**)[73]. This data supports previously published data which has shown that SctQ expression is required for secretion of proteins via the T3SS. In our experimental setup, SctL is labeled with a Halo tag and stained with a blinking dye. Single-molecule tracking of SctL will be performed in the presence and absence of the optogenetic activating wavelength (488 nm). We expect to see a change in the diffusive behavior of the binding partner, and depletion of the co-diffusive state at 1.3 $\mu m^2/s$ upon sequestration of SctQ to the membrane (**Figure 5.1**).

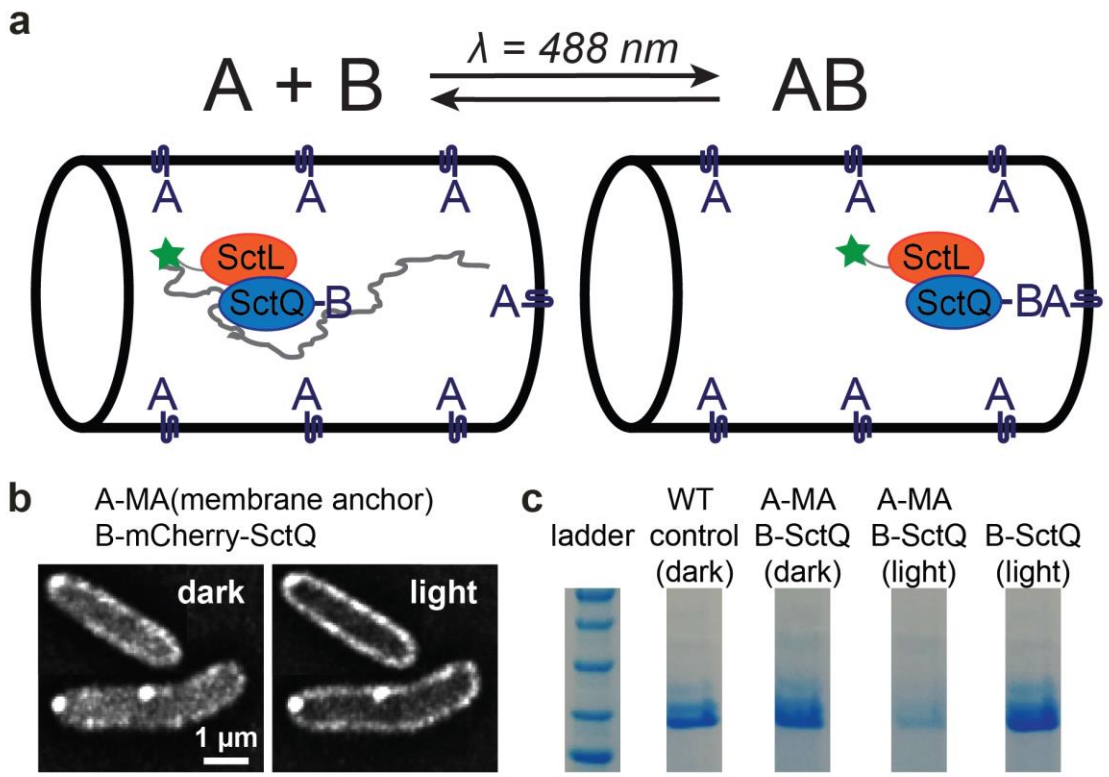

Figure 5.2. Knocksideways assay of T3SS proteins in single-molecule tracking experiments. a) Light inducible dimers are used to sequester proteins of interest. In the schematic "A" refers to the membrane-anchored iLID protein, which senses blue light, while "B" refers to the cytosolic optogenetic binding partner, SspB. SspB is used to tag a T3SS protein of interest, SctQ, which has been shown through our single-molecule tracking analyses to interact with SctL. Illumination of cells with 488 nm light induces a conformational change in the iLID protein which will sequester SspB-SctQ to MA-iLID at the membrane. Single-molecule tracking of fluorescently-labeled (green star) SctL will show a distinct shift in diffusion to the membrane if it indeed interacts with SctQ. **b**) SspB-mCherry-SctQ images before (dark) and after (light) blue-light illumination shows spatial redistribution of SctQ. **c**) SDS-PAGE *of Yersinia enterocolitica* supernatant after inducing

secretion in different genetic and light backgrounds. Decreased secretion is dependent on the blue-light and the expression of the membrane-anchored iLID protein ("A")[73].

I have made the strains required for these experiments (Table 1). In each strain, I chose to delete SctD which acts as a membraned-embedded scaffold for cytosolic protein binding to the injectisome (**Figure 5.1**)[181]. This is necessary because SctL shows >70% injectisome bound fraction in WT conditions at the cell membrane[103]. Therefore, it may be difficult to distinguish between iLID-associated and injectisome-associated molecules. While injectisome-bound SctL may show different diffusive behavior than SctL bound to SctQ-MA-iLID, it will make initial analyses easier to interpret. Further, I have made both $SspB_{nano}$-SctQ and $SspB_{micro}$-SctQ strains to allow for optimization of the knocksideways assay by changing the affinity of the interaction. All T3SS genes were tagged at endogenous sites, while MA-iLID will be expressed exogenously from the pBad plasmid, as with the experiments described in this dissertation.

Table 1. Genotype of strains to be used in knocksideways experiments.

ΔSctD;Halo-SctL;$SspB_{nano}$-SctQ
ΔSctD;Halo-SctL;$SspB_{nano}$-SctQ + pBad-MA-iLID
ΔSctD;Halo-SctL;$SspB_{micro}$-SctQ
ΔSctD;Halo-SctL;$SspB_{micro}$-SctQ + pBad-MA-iLID

For initial screening of the strains, I performed a Western blot for Halo-SctL and pBad-MA-ILID, which contains an N-terminal FLAG tag. I observed an interesting trend where $SspB_{micro}$-SctQ strains showed decreased expression of Halo-SctL compared to $SspB_{nano}$-SctQ. Each of these strains were derived from the same parent ΔSctD;Halo-SctL

strain and co-expressed MA-iLID, indicating a possible change in expression due to optogenetic sequestration, dependent on the affinity of the interaction (**Figure 5.3**). Further expression tests and controls need to be done to confirm this observation. The ΔSctD;Halo-SctL;$SspB_{nano}$-SctQ + pBad-MA-iLID strain is ready for use in single-molecule knocksideways assays based on expression levels observed in the Western blot, though extensive optimization of experimental parameters will likely need to be done. Initial efforts will likely include imaging of cells using different expression levels at steady state, and trends will be used for forming interaction models.

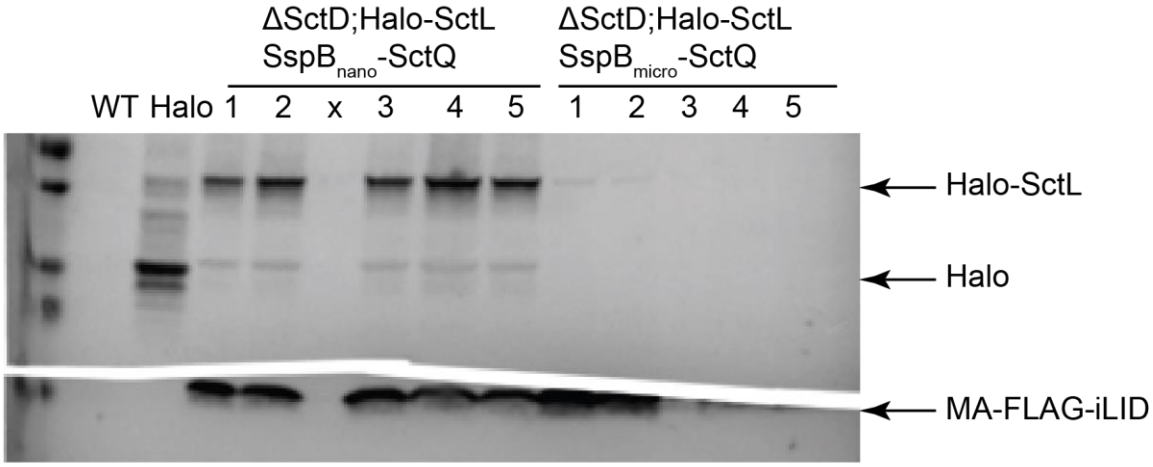

Figure 5.3. Western blot of *Yersinia* optogenetic strains. Top: α-Halo blot in strains expressing Halo-SctL from the endogenous promoter. The free Halo expressing strain in lane 2 exogenously expresses Halo from the pACYC plasmid. Bottom: α-FLAG blot for screening pBAD MA-FLAG-iLID plasmid uptake.

The method described above can be applied to any cytosolic protein which tolerates protein tags and can be used to distinguish possible interaction partners. Optogenetic systems are particularly attractive because the light signal is transient, and interaction

between binding partners is reversible. Therefore, optogenetic systems can truly shine when applied to systems that are important for maintaining cell viability which are also good targets for antimicrobial drugs. For example, peptidoglycan synthesis is required for maintaining osmotic pressure of bacteria, and ultimately guides cell morphogenesis and shape maintenance[182-184]. Though the peptidoglycan is synthesized within the periplasmic space, its synthesis is highly regulated within the cytosol. Therefore, it may be possible to use cytosolic optogenetic switches to dictate the position and timing of peptidoglycan synthesis within the periplasmic spaces.

5.2.2. Characterizing far-red wavelength sensitivity of iLID protein

Single-molecule tracking characterization of the iLID system showed that it can be activated at longer wavelengths than previously reported under high intensity conditions. To understand the bounds of this trend, we could perform diffraction-limited imaging experiments as performed in Chapter 4, where we image SspB-Halo using low-intensity 561 nm laser, then introduce high intensity 647 nm illumination, and characterize the fluorescence distribution after this perturbation. This is a reasonable extension because we have the required laser in the lab, and it could be incorporated into our current single-molecule microscope by adding optical elements required for far-red imaging. We expect that we would need much higher intensity 647 nm light to produce the same level of membrane sequestration as seen using 561 nm light. Given that this proves true, we could change our labeling system to use a 647 nm excitable dye, and perform single-molecule tracking experiments under these conditions. In this way, we could improve the dynamic range of the iLID optogenetic system under single-molecule fluorescence imaging conditions.

Previously published work which characterized the kinetics of the iLID interaction partners in minimal synthetic cells showed a diminished dynamic range of affinity in blue-light versus dark conditions (~4 fold)[159,160] compared to the range published in original fluorescence polarization in vitro assays[77]. The diminished range in affinity agrees with the analyses that I present in Chapter 4. The authors of the synthetic cell study suggest that steric hindrance due to membrane-anchoring of the iLID component could contribute to this result. Therefore, an interesting extension of the work presented here would be to investigate this claim by reconstituting the iLID protein in different membrane conditions (giant unilamellar vesicles, supported lipid bilayers, nanodiscs, etc.), and determining if this 1) effects the absorption range of the protein, or 2) removes a degree of freedom by limiting the orientations sampled by the protein, and allowing for a faster rate of association of its binding partner, SspB. In a parallel experiment, the linker length between the N-terminal transmembrane helix and iLID could be modulated as a way to increase the degrees of freedom in spatial sampling. While this work would likely require a collaboration to perform absorption measurements and binding assays, our lab could work on computationally modeling binding kinetics when a binding partner is restricted in movement at the membrane.

5.2.3. Bolster single-molecule trajectory analyses using cumulative displacement analysis

Lastly, the cumulative displacement analysis that I used to analyze SspB diffusion yielded some interesting results that could be applied to our current analysis framework. Traditional mean-squared-displacement (MSD) analyses compare the average squared displacement at increasing lag times, always comparing the position at time point (*t*) to the

original, starting position. For diffusion within the confines of a cell, the MSD will plateau as lag times increase because the maximum distance that a molecule can traverse is approximately the length of the cell. By instead considering the cumulative displacement, one can visualize the displacements within a trajectory as a linear relationship over time, without plateauing. I observed that the rate of displacement, or the slope of the cumulative displacement over time, showed a linear relationship that was dependent on how fast the molecule was moving (the diffusion coefficient), as well as the length and radius of the cell (**Figure 5.4**). As expected, decreasing the radius of the cell showed the largest decrease in displacement rate due to the increase in confinement. The change in slope may, perhaps, be marginal, but suggests that our fitting models which utilize simulated data at a specific cell geometry, may need to be adjusted when fitting data derived from bacteria with different dimensions than the average *Yersinia enterocolitica* cell. Further, cumulative displacement analysis could serve as another way to evaluate state assignment in our diffusion analysis.

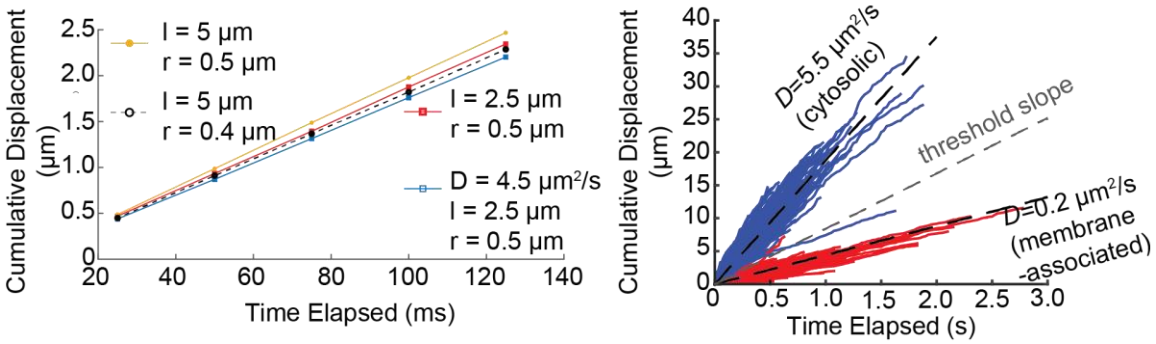

Figure 5.4. Cumulative displacement analysis of simulated trajectories shows dependence on cell radius and length. Left: simulated average cumulative displacement of N=1,000 molecules diffusing at 5.5 $\mu m^2/s$ (yellow, black, red lines) show a decrease

cumulative displacement slope when the cell radius is smaller (compare yellow versus black) or when the cell length is smaller (compare yellow versus red). Molecules diffusing at a slower rate of 4.5 $\mu m^2/s$ (blue) shows a characteristically smaller slope compared to a molecule diffusing at 5.5 $\mu m^2/s$ with the same cell dimensions (red). Each point is an average of 1,000 trajectories. Right: Experimental data which exhibits a fast, cytosolic diffusion population (blue), and a slow-membrane bound diffusion population (red), is described well by simulation molecule diffusion at 5.5 $\mu m^2/s$ and 0.2 $\mu m^2/s$, respectively, with the same cell geometry as experimentally observed for *E. coli* cells.

5.3. Conclusions

Single-molecule localization microscopy is a powerful tool that enables resolution of static and dynamic structures. Experimental validation of diffusion state assignment traditionally involves permanent disruption to the interactions or processes being studied. We propose using optogenetics as a transient way to disrupt interactions for experimental validation of diffusion state assignments. Here, we evaluate the iLID optogenetic system for its feasibility in single-molecule tracking experiments. Surprisingly, we found that increased photon flux of long wavelengths of light triggered the optogenetic response. In this chapter, I outline suggested experiments which not only extend our diffusion state assignment analysis, but also probes the photophysical behavior of the iLID protein itself. The analyses performed here offer an optimistic view for incorporating iLID into tracking experiments and for understanding light sensing protein domains.

REFERENCES

1 Lin, J.-S. & Lai, E.-M. 211-219 (Springer New York, 2017).

2 Lee, C. 401-406 (Humana Press, 2007).

3 Korasick, D. A. & Tanner, J. J. Determination of protein oligomeric structure from small-angle X-ray scattering. *Protein Science* **27**, 814-824, doi:10.1002/pro.3376 (2018).

4 Mertens, H. D. T. & Svergun, D. I. Combining NMR and small angle X-ray scattering for the study of biomolecular structure and dynamics. *Archives of biochemistry and biophysics* **628**, 33-41, doi:https://doi.org/10.1016/j.abb.2017.05.005 (2017).

5 Purslow, J. A., Khatiwada, B., Bayro, M. J. & Venditti, V. NMR Methods for Structural Characterization of Protein-Protein Complexes. *Frontiers in Molecular Biosciences* **7**, doi:10.3389/fmolb.2020.00009 (2020).

6 Tugarinov, V., Muhandiram, R., Ayed, A. & Kay, L. E. Four-Dimensional NMR Spectroscopy of a 723-Residue Protein: Chemical Shift Assignments and Secondary Structure of Malate Synthase G. *Journal of the American Chemical Society* **124**, 10025-10035, doi:10.1021/ja0205636 (2002).

7 Puthenveetil, R. & Vinogradova, O. Solution NMR: A powerful tool for structural and functional studies of membrane proteins in reconstituted environments. *Journal of Biological Chemistry* **294**, 15914-15931, doi:10.1074/jbc.rev119.009178 (2019).

8 Dafforn, T. R. So how do you know you have a macromolecular complex? *Acta Crystallographica Section D Biological Crystallography* **63**, 17-25, doi:10.1107/s0907444906047044 (2007).

9 Wiseman, T., Williston, S., Brandts, J. F. & Lin, L.-N. Rapid measurement of binding constants and heats of binding using a new titration calorimeter. *Analytical Biochemistry* **179**, 131-137, doi:https://doi.org/10.1016/0003-2697(89)90213-3 (1989).

10 Park, D. *et al.* Visualization of the type III secretion mediated Salmonella-host cell interface using cryo-electron tomography. *Elife* **7**, doi:10.7554/eLife.39514 (2018).

11 Villa, E., Schaffer, M., Plitzko, J. M. & Baumeister, W. Opening windows into the cell: focused-ion-beam milling for cryo-electron tomography. *Current Opinion in Structural Biology* **23**, 771-777, doi:10.1016/j.sbi.2013.08.006 (2013).

12 Wagner, F. R. *et al.* Preparing samples from whole cells using focused-ion-beam milling for cryo-electron tomography. *Nature Protocols* **15**, 2041-2070, doi:10.1038/s41596-020-0320-x (2020).

13 Xu, C. S. *et al.* Enhanced FIB-SEM systems for large-volume 3D imaging. *eLife* **6**, e25916, doi:10.7554/eLife.25916 (2017).

14 Achimovich, A. M., Ai, H. & Gahlmann, A. Enabling technologies in super-resolution fluorescence microscopy: reporters, labeling, and methods of measurement. *Current Opinion in Structural Biology* **58**, 224-232, doi:https://doi.org/10.1016/j.sbi.2019.05.001 (2019).

15 Aaron, J. S., Taylor, A. B. & Chew, T.-L. Image co-localization – co-occurrence versus correlation. *Journal of Cell Science* **131**, jcs211847, doi:10.1242/jcs.211847 (2018).

16 Szymborska, A. *et al.* Nuclear Pore Scaffold Structure Analyzed by Super-Resolution Microscopy and Particle Averaging. *Science* **341**, 655-658, doi:10.1126/science.1240672 (2013).
17 Thevathasan, J. V. *et al.* Nuclear pores as versatile reference standards for quantitative superresolution microscopy. *Nature Methods* **16**, 1045-1053, doi:10.1038/s41592-019-0574-9 (2019).
18 Malkusch, S. *et al.* Coordinate-based colocalization analysis of single-molecule localization microscopy data. *Histochemistry and cell biology*, doi:10.1007/s00418-011-0880-5 (2011).
19 Larson, J. D., Rodgers, M. L. & Hoskins, A. A. Visualizing cellular machines with colocalization single molecule microscopy. *Chem. Soc. Rev.* **43**, 1189-1200, doi:10.1039/c3cs60208g (2014).
20 Levet, F. *et al.* A tessellation-based colocalization analysis approach for single-molecule localization microscopy. *Nature communications* **10**, doi:10.1038/s41467-019-10007-4 (2019).
21 Wachsmuth, M. & Weisshart, K. 183-233 (Springer Berlin Heidelberg, 2007).
22 Phair, R. D. & Misteli, T. Kinetic modelling approaches to in vivo imaging. *Nature Reviews Molecular Cell Biology* **2**, 898-907, doi:10.1038/35103000 (2001).
23 Qian, J., Yao, B. & Wu, C. Fluorescence resonance energy transfer detection methods: Sensitized emission and acceptor bleaching. *Experimental and Therapeutic Medicine* **8**, 1375-1380, doi:10.3892/etm.2014.1928 (2014).
24 Zeug, A., Woehler, A., Neher, E. & Evgeni. Quantitative Intensity-Based FRET Approaches—A Comparative Snapshot. *Biophysical journal* **103**, 1821-1827, doi:10.1016/j.bpj.2012.09.031 (2012).
25 Okamoto, K. & Sako, Y. Recent advances in FRET for the study of protein interactions and dynamics. *Current Opinion in Structural Biology* **46**, 16-23, doi:10.1016/j.sbi.2017.03.010 (2017).
26 Petazzi, R. A., Aji, A. K. & Chiantia, S. 1-41 (Elsevier, 2020).
27 Einstein, A., Fürth, R., Cowper, A. D. & Dover, P. (1956).
28 Debye, P. J. W. *Polar Molecules*. (Dover publications, 1929).
29 Lavalette, D., Tétreau, C., Tourbez, M. & Blouquit, Y. Microscopic Viscosity and Rotational Diffusion of Proteins in a Macromolecular Environment. *Biophysical journal* **76**, 2744-2751, doi:10.1016/s0006-3495(99)77427-8 (1999).
30 Metzler, R. & Klafter, J. The random walk's guide to anomalous diffusion: a fractional dynamics approach. *Physics Reports* **339**, 1-77, doi:https://doi.org/10.1016/S0370-1573(00)00070-3 (2000).
31 Bruno, L., Levi, V., Brunstein, M. & Despósito, M. A. Transition to superdiffusive behavior in intracellular actin-based transport mediated by molecular motors. *Physical Review E* **80**, doi:10.1103/physreve.80.011912 (2009).
32 Stracy, M. *et al.* Transient non-specific DNA binding dominates the target search of bacterial DNA-binding proteins. *Molecular Cell* **81**, 1499-1514.e1496, doi:https://doi.org/10.1016/j.molcel.2021.01.039 (2021).
33 Mika, J. T. & Poolman, B. Macromolecule diffusion and confinement in prokaryotic cells. *Current Opinion in Biotechnology* **22**, 117-126, doi:https://doi.org/10.1016/j.copbio.2010.09.009 (2011).

34 Bellotto, N. *et al. Dependence of diffusion in Escherichia coli cytoplasm on protein size, environmental conditions and cell growth* (Cold Spring Harbor Laboratory, 2022).

35 Spitzer, J. From Water and Ions to Crowded Biomacromolecules: In Vivo Structuring of a Prokaryotic Cell. *Microbiol. Mol. Biol. Rev.* **75**, 491-506, doi:doi:10.1128/MMBR.00010-11 (2011).

36 Collet, C., Thomassin, J.-L., Francetic, O., Genevaux, P. & Tran Van Nhieu, G. Protein polarization driven by nucleoid exclusion of DnaK(HSP70)–substrate complexes. *Nature communications* **9**, doi:10.1038/s41467-018-04414-2 (2018).

37 Laloux, G. & Jacobs-Wagner, C. Spatiotemporal control of PopZ localization through cell cycle-coupled multimerization. *The Journal of cell biology* **201**, 827-841, doi:10.1083/jcb.201303036 (2013).

38 Elf, J. & Barkefors, I. Single-Molecule Kinetics in Living Cells. *Annu Rev Biochem* **88**, 635-659, doi:10.1146/annurev-biochem-013118-110801 (2019).

39 Stracy, M. *et al.* Single-molecule imaging of UvrA and UvrB recruitment to DNA lesions in living Escherichia coli. *Nature communications* **7**, 12568, doi:10.1038/ncomms12568 (2016).

40 Chen, T.-Y. *et al.* Concentration- and chromosome-organization-dependent regulator unbinding from DNA for transcription regulation in living cells. *Nature communications* **6**, 7445, doi:10.1038/ncomms8445 (2015).

41 Elf, J., Li, G. W. & Xie, X. S. Probing Transcription Factor Dynamics at the Single-Molecule Level in a Living Cell. *Science* **316**, 1191-1194, doi:10.1126/science.1141967 (2007).

42 Mueller, F., Stasevich, T. J., Mazza, D. & McNally, J. G. Quantifying transcription factor kinetics: At work or at play? *Critical reviews in biochemistry and molecular biology* **48**, 492-514, doi:10.3109/10409238.2013.833891 (2013).

43 Uphoff, S., Reyes-Lamothe, R., Garza de Leon, F., Sherratt, D. J. & Kapanidis, A. N. Single-molecule DNA repair in live bacteria. *Proceedings of the National Academy of Sciences of the United States of America* **110**, 8063-8068, doi:10.1073/pnas.1301804110 (2013).

44 Kuhn, T., Hettich, J., Davtyan, R. & Gebhardt, J. C. M. Single molecule tracking and analysis framework including theory-predicted parameter settings. *Scientific Reports* **11**, doi:10.1038/s41598-021-88802-7 (2021).

45 Das, R., Cairo, C. W. & Coombs, D. A Hidden Markov Model for Single Particle Tracks Quantifies Dynamic Interactions between LFA-1 and the Actin Cytoskeleton. *PLoS Computational Biology* **5**, e1000556, doi:10.1371/journal.pcbi.1000556 (2009).

46 Chung, I. *et al.* Spatial control of EGF receptor activation by reversible dimerization on living cells. *Nature* **464**, 783-787, doi:10.1038/nature08827 (2010).

47 Heckert, A., Dahal, L., Tjian, R. & Darzacq, X. *Recovering mixtures of fast diffusing states from short single particle trajectories* (Cold Spring Harbor Laboratory, 2021).

48 Persson, F., Lindén, M., Unoson, C. & Elf, J. Extracting intracellular diffusive states and transition rates from single-molecule tracking data. *Nature Methods* **10**, 265-269, doi:10.1038/nmeth.2367 (2013).

49 Rocha, J., Corbitt, J., Yan, T., Richardson, C. & Gahlmann, A. Resolving Cytosolic Diffusive States in Bacteria by Single-Molecule Tracking. *Biophysical journal* **116**, 1970-1983, doi:https://doi.org/10.1016/j.bpj.2019.03.039 (2019).

50 Rocha, J. M. *et al.* Single-molecule tracking in live Yersinia enterocolitica reveals distinct cytosolic complexes of injectisome subunits. *Integrative Biology* **10**, 502-515, doi:10.1039/c8ib00075a (2018).

51 Chen, T. Y. *et al.* Quantifying Multistate Cytoplasmic Molecular Diffusion in Bacterial Cells via Inverse Transform of Confined Displacement Distribution. *The journal of physical chemistry. B* **119**, 14451-14459, doi:10.1021/acs.jpcb.5b08654 (2015).

52 Oswald, F., Varadarajan, A., Lill, H., Peterman, E. J. & Bollen, Y. J. MreB-Dependent Organization of the E. coli Cytoplasmic Membrane Controls Membrane Protein Diffusion. *Biophysical journal* **110**, 1139-1149, doi:10.1016/j.bpj.2016.01.010 (2016).

53 Oswald, F., E, L. M. B., Bollen, Y. J. & Peterman, E. J. Imaging and quantification of trans-membrane protein diffusion in living bacteria. *Phys Chem Chem Phys* **16**, 12625-12634, doi:10.1039/c4cp00299g (2014).

54 Ernst, O. P. *et al.* Microbial and Animal Rhodopsins: Structures, Functions, and Molecular Mechanisms. *Chemical Reviews* **114**, 126-163, doi:10.1021/cr4003769 (2014).

55 Levskaya, A., Weiner, O. D., Lim, W. A. & Voigt, C. A. Spatiotemporal control of cell signalling using a light-switchable protein interaction. *Nature* **461**, 997-1001, doi:10.1038/nature08446 (2009).

56 Chaves, I. *et al.* The Cryptochromes: Blue Light Photoreceptors in Plants and Animals. *Annual Review of Plant Biology* **62**, 335-364, doi:10.1146/annurev-arplant-042110-103759 (2011).

57 Gomelsky, M. & Klug, G. BLUF: a novel FAD-binding domain involved in sensory transduction in microorganisms. *Trends in Biochemical Sciences* **27**, 497-500, doi:https://doi.org/10.1016/S0968-0004(02)02181-3 (2002).

58 Möglich, A., Yang, X., Ayers, R. A. & Moffat, K. Structure and Function of Plant Photoreceptors. *Annual Review of Plant Biology* **61**, 21-47, doi:10.1146/annurev-arplant-042809-112259 (2010).

59 Chen, M., Chory, J. & Fankhauser, C. Light Signal Transduction in Higher Plants. *Annu. Rev. Genet.* **38**, 87-117, doi:10.1146/annurev.genet.38.072902.092259 (2004).

60 Ortiz-Guerrero, J. M., Polanco, M. C., Murillo, F. J., Padmanabhan, S. & Elias-Arnanz, M. Light-dependent gene regulation by a coenzyme B12-based photoreceptor. *Proc Natl Acad Sci U S A* **108**, 7565-7570, doi:10.1073/pnas.1018972108 (2011).

61 Losi, A. & Gärtner, W. The Evolution of Flavin-Binding Photoreceptors: An Ancient Chromophore Serving Trendy Blue-Light Sensors. *Annual Review of Plant Biology* **63**, 49-72, doi:10.1146/annurev-arplant-042811-105538 (2012).

62 Kottke, T., Xie, A., Larsen, D. S. & Hoff, W. D. Photoreceptors Take Charge: Emerging Principles for Light Sensing. *Annual Review of Biophysics* **47**, 291-313, doi:10.1146/annurev-biophys-070317-033047 (2018).

63 Palczewski, K. G Protein–Coupled Receptor Rhodopsin. *Annual Review of Biochemistry* **75**, 743-767, doi:10.1146/annurev.biochem.75.103004.142743 (2006).
64 Klare, J. P., Chizhov, I. & Engelhard, M. 73-122 (Springer Berlin Heidelberg).
65 Deisseroth, K. Optogenetics: 10 years of microbial opsins in neuroscience. *Nature Neuroscience* **18**, 1213-1225, doi:10.1038/nn.4091 (2015).
66 Kim, C. K., Adhikari, A. & Deisseroth, K. Integration of optogenetics with complementary methodologies in systems neuroscience. *Nature Reviews Neuroscience* **18**, 222-235, doi:10.1038/nrn.2017.15 (2017).
67 Yawo, H., Kandori, H., Koizumi, A. & Kageyama, R.
68 Entcheva, E. & Kay, M. W. Cardiac optogenetics: a decade of enlightenment. *Nature Reviews Cardiology* **18**, 349-367, doi:10.1038/s41569-020-00478-0 (2021).
69 Sung, Y.-L., Wang, T.-W., Lin, T.-T. & Lin, S.-F. Optogenetics in cardiology: methodology and future applications. *International Journal of Arrhythmia* **23**, doi:10.1186/s42444-022-00060-4 (2022).
70 Kramer, M. M., Lataster, L., Weber, W. & Radziwill, G. Optogenetic Approaches for the Spatiotemporal Control of Signal Transduction Pathways. *International Journal of Molecular Sciences* **22**, 5300, doi:10.3390/ijms22105300 (2021).
71 Leopold, A. V. & Verkhusha, V. V. Light control of RTK activity: from technology development to translational research. *Chemical science* **11**, 10019-10034, doi:10.1039/d0sc03570j (2020).
72 Leyden, F. *et al.* Rac1 activation can generate untemplated, lamellar membrane ruffles. *BMC Biology* **19**, doi:10.1186/s12915-021-00997-3 (2021).
73 Lindner, F., Milne-Davies, B., Langenfeld, K., Stiewe, T. & Diepold, A. LITESEC-T3SS - Light-controlled protein delivery into eukaryotic cells with high spatial and temporal resolution. *Nature communications* **11**, 2381, doi:10.1038/s41467-020-16169-w (2020).
74 Inglés-Prieto, Á. *et al.* Light-assisted small-molecule screening against protein kinases. *Nature chemical biology* **11**, 952-954, doi:10.1038/nchembio.1933 (2015).
75 Khamo, J. S., Krishnamurthy, V. V., Sharum, S. R., Mondal, P. & Zhang, K. Applications of Optobiology in Intact Cells and Multicellular Organisms. *J Mol Biol* **429**, 2999-3017, doi:10.1016/j.jmb.2017.08.015 (2017).
76 Benedetti, L. *et al.* Light-activated protein interaction with high spatial subcellular confinement. *Proc Natl Acad Sci U S A* **115**, E2238-E2245, doi:10.1073/pnas.1713845115 (2018).
77 Guntas, G. *et al.* Engineering an improved light-induced dimer (iLID) for controlling the localization and activity of signaling proteins. *Proc Natl Acad Sci U S A* **112**, 112-117, doi:10.1073/pnas.1417910112 (2015).
78 Zimmerman, S. P. *et al.* Tuning the Binding Affinities and Reversion Kinetics of a Light Inducible Dimer Allows Control of Transmembrane Protein Localization. *Biochemistry* **55**, 5264-5271, doi:10.1021/acs.biochem.6b00529 (2016).
79 Harper, S. M. Structural Basis of a Phototropin Light Switch. *Science (American Association for the Advancement of Science)* **301**, 1541-1544.
80 Zayner, J. P., Antoniou, C. & Sosnick, T. R. The Amino-Terminal Helix Modulates Light-Activated Conformational Changes in AsLOV2. *J. Mol. Biol.* **419**, 61-74, doi:10.1016/j.jmb.2012.02.037 (2012).

81 Wittmann, T., Dema, A. & Van Haren, J. Lights, cytoskeleton, action: Optogenetic control of cell dynamics. *Current Opinion in Cell Biology* **66**, 1-10, doi:10.1016/j.ceb.2020.03.003 (2020).

82 Abbe, E. Beiträge zur Theorie des Mikroskops und der mikroskopischen Wahrnehmung. *Archiv für mikroskopische Anatomie* **9**, 413-418, doi:10.1007/BF02956173 (1873).

83 Liu, W. *et al.* Breaking the Axial Diffraction Limit: A Guide to Axial Super-Resolution Fluorescence Microscopy. *Laser & Photonics Reviews* **12**, 1700333, doi:10.1002/lpor.201700333 (2018).

84 Rottenfusser, R. W., Erin E.; Davidson, Michael W. . *Numerical aperture and resolution*, <https://www.zeiss.com/microscopy/int/solutions/reference/basic-microscopy/numerical-aperture-and-resolution.html> (

85 Hell, S. W. & Wichmann, J. Breaking the diffraction resolution limit by stimulated-emission - stimulated-emission-depletion fluorescence microscopy. *Optics Letters* **19**, 780-782 (1994).

86 Gustafsson, M. G. L. Surpassing the lateral resolution limit by a factor of two using structured illumination microscopy. *Journal of Microscopy* **198**, 82-87, doi:doi:10.1046/j.1365-2818.2000.00710.x (2000).

87 Lelek, M. *et al.* Single-molecule localization microscopy. *Nature Reviews Methods Primers* **1**, doi:10.1038/s43586-021-00038-x (2021).

88 Hess, S. T., Girirajan, T. P. K. & Mason, M. D. Ultra-high resolution imaging by fluorescence photoactivation localization microscopy. *Biophysical journal* **91**, 4258-4272, doi:10.1529/biophysj.106.091116 (2006).

89 Rust, M. J., Bates, M. & Zhuang, X. W. Sub-diffraction-limit imaging by stochastic optical reconstruction microscopy (STORM). *Nature Methods* **3**, 793-795, doi:10.1038/nmeth929 (2006).

90 Heilemann, M. *et al.* Subdiffraction-resolution fluorescence imaging with conventional fluorescent probes. *Angewandte Chemie International Edition* **47**, 6172-6176, doi:10.1002/anie.200802376 (2008).

91 Biteen, J. S. *et al.* Super-resolution imaging in live *Caulobacter crescentus* cells using photoswitchable EYFP. *Nature Methods* **5**, 947-949, doi:10.1038/nmeth.1258 (2008).

92 van de Linde, S., Sauer, M. & Heilemann, M. Subdiffraction-resolution fluorescence imaging of proteins in the mitochondrial inner membrane with photoswitchable fluorophores. *Journal of Structural Biology* **164**, 250-254, doi:10.1016/j.jsb.2008.08.002 (2008).

93 Sharonov, A. & Hochstrasser, R. M. Wide-field subdiffraction imaging by accumulated binding of diffusing probes. *Proceedings of the National Academy of Sciences* **103**, 18911-18916, doi:10.1073/pnas.0609643104 (2006).

94 Schnitzbauer, J., Strauss, M. T., Schlichthaerle, T., Schueder, F. & Jungmann, R. Super-resolution microscopy with DNA-PAINT. *Nature Protocols* **12**, 1198-1228, doi:10.1038/nprot.2017.024 (2017).

95 Hajj, B., El Beheiry, M., Izeddin, I., Darzacq, X. & Dahan, M. Accessing the third dimension in localization-based super-resolution microscopy. *Phys. Chem. Chem. Phys.* **16**, 16340-16348, doi:10.1039/c4cp01380h (2014).

96 Ram, S., Prabhat, P., Chao, J., Ward, E. S. & Ober, R. J. High Accuracy 3D Quantum Dot Tracking with Multifocal Plane Microscopy for the Study of Fast Intracellular Dynamics in Live Cells. *Biophysical journal* **95**, 6025-6043, doi:10.1529/biophysj.108.140392 (2008).

97 Shtengel, G. *et al.* Interferometric fluorescent super-resolution microscopy resolves 3D cellular ultrastructure. *Proceedings of the National Academy of Sciences of the United States of America* **106**, 3125-3130, doi:10.1073/pnas.0813131106 (2009).

98 Jia, S., Vaughan, J. C. & Zhuang, X. Isotropic three-dimensional super-resolution imaging with a self-bending point spread function. *Nature Photonics* **8**, 302 (2014).

99 Kao, H. P. & Verkman, A. S. Tracking of single fluorescent particles in three dimensions: use of cylindrical optics to encode particle position. *Biophysical journal* **67**, 1291-1300, doi:https://doi.org/10.1016/S0006-3495(94)80601-0 (1994).

100 Pavani, S. R. P. *et al.* Three-dimensional, single-molecule fluorescence imaging beyond the diffraction limit by using a double-helix point spread function. *Proceedings of the National Academy of Sciences of the United States of America* **106**, 2995-2999, doi:10.1073/pnas.0900245106 (2009).

101 Gahlmann, A. & Moerner, W. E. Exploring bacterial cell biology with single-molecule tracking and super-resolution imaging. *Nature Reviews Microbiology* **12**, 9-22, doi:10.1038/nrmicro3154 (2014).

102 Gahlmann, A. *et al.* Quantitative Multicolor Subdiffraction Imaging of Bacterial Protein Ultrastructures in Three Dimensions. *Nano Letters* **13**, 987-993, doi:10.1021/nl304071h (2013).

103 Prindle, J. R., Rocha, J., Wang, Y., Diepold, A. & Gahlmann, A. Distinct complexes containing the cytosolic type III secretion system ATPase resolved by 3D single-molecule tracking in live Yersinia enterocolitica. *bioRxiv*, 2022.2004.2025.488798, doi:10.1101/2022.04.25.488798 (2022).

104 Thompson, R. E., Larson, D. R. & Webb, W. W. Precise Nanometer Localization Analysis for Individual Fluorescent Probes. *Biophysical journal* **82**, 2775-2783, doi:https://doi.org/10.1016/S0006-3495(02)75618-X (2002).

105 Jradi, F. M. & Lavis, L. D. Chemistry of Photosensitive Fluorophores for Single-Molecule Localization Microscopy. *ACS Chemical Biology* **14**, 1077-1090, doi:10.1021/acschembio.9b00197 (2019).

106 Tanenbaum, M. E., Gilbert, L. A., Qi, L. S., Weissman, J. S. & Vale, R. D. A protein-tagging system for signal amplification in gene expression and fluorescence imaging. *Cell* **159**, 635-646, doi:10.1016/j.cell.2014.09.039 (2014).

107 Los, G. V. *et al.* HaloTag: A Novel Protein Labeling Technology for Cell Imaging and Protein Analysis. *ACS Chemical Biology* **3**, 373-382, doi:10.1021/cb800025k (2008).

108 Wang, L., Brock, A., Herberich, B. & Schultz, P. G. Expanding the Genetic Code of Escherichia coli. *Science* **292**, 498-500, doi:doi:10.1126/science.1060077 (2001).

109 Lang, K. & Chin, J. W. Cellular incorporation of unnatural amino acids and bioorthogonal labeling of proteins. *Chemical Reviews (Washington, D. C.)* **114**, 4764-4806, doi:10.1021/cr400355w (2014).

110 Lang, K. *et al.* Genetically encoded norbornene directs site-specific cellular protein labelling via a rapid bioorthogonal reaction. *Nature chemistry* **4**, 298-304, doi:10.1038/nchem.1250 (2012).

111 Lang, K. *et al.* Genetic Encoding of Bicyclononynes andtrans-Cyclooctenes for Site-Specific Protein Labeling *in vitro* and in Live Mammalian Cells via Rapid Fluorogenic Diels–Alder Reactions. *Journal of the American Chemical Society* **134**, 10317-10320, doi:10.1021/ja302832g (2012).

112 Swartz, T. E. *et al.* The Photocycle of a Flavin-binding Domain of the Blue Light Photoreceptor Phototropin. *Journal of Biological Chemistry* **276**, 36493-36500, doi:10.1074/jbc.m103114200 (2001).

113 Harper, S. M., Neil, L. C. & Gardner, K. H. Structural Basis of a Phototropin Light Switch. *Science* **301**, 1541-1544, doi:doi:10.1126/science.1086810 (2003).

114 Vojnovic, I., Winkelmeier, J. & Endesfelder, U. Visualizing the inner life of microbes: practices of multi-color single-molecule localization microscopy in microbiology. *Biochem Soc Trans*, doi:10.1042/BST20180399 (2019).

115 Weissman, T. A. & Pan, Y. A. Brainbow: New Resources and Emerging Biological Applications for Multicolor Genetic Labeling and Analysis. *Genetics* **199**, 293-306, doi:10.1534/genetics.114.172510 (2015).

116 Yan, T., Richardson, C. J., Zhang, M. & Gahlmann, A. Computational correction of spatially variant optical aberrations in 3D single-molecule localization microscopy. *Optics express* **27**, 12582-12599 (2019).

117 Losi, A., Gardner, K. H. & Möglich, A. Blue-Light Receptors for Optogenetics. *Chemical Reviews* **118**, 10659-10709, doi:10.1021/acs.chemrev.8b00163 (2018).

118 Yan, T. *Protein diffusion analysis and aberration correction in single molecule localization microscopy* Doctor of Philosophy thesis, University of Virginia, (2021).

119 Rocha, J. M. *Dynamic Assembly of the Type-3 Secretion System in Yersinia enterocolitica Probed by Super-Resolution Fluorescence Imaging* Doctor of Philosophy thesis, Graduate School of Arts and Sciences, University of Virginia, (2021).

120 Lew, M., Von Diezmann, A. R. S. & Moerner, W. E. Easy-DHPSF open-source software for three-dimensional localization of single molecules with precision beyond the optical diffraction limit. *Protoc. Exch.* (2013).

121 Paintdakhi, A. *et al.* Oufti: An integrated software package for high-accuracy, high-throughput quantitative microscopy analysis. *Molecular microbiology* **99**, 767-777, doi:10.1111/mmi.13264 (2016).

122 Kastantin, M., Langdon, B. B., Chang, E. L. & Schwartz, D. K. Single-Molecule Resolution of Interfacial Fibrinogen Behavior: Effects of Oligomer Populations and Surface Chemistry. *Journal of the American Chemical Society* **133**, 4975-4983, doi:10.1021/ja110663u (2011).

123 Loffreda, A. *et al.* Live-cell p53 single-molecule binding is modulated by C-terminal acetylation and correlates with transcriptional activity. *Nature communications* **8**, doi:10.1038/s41467-017-00398-7 (2017).

124 Presman, D. M. *et al.* Quantifying transcription factor binding dynamics at the single-molecule level in live cells. *Methods*, doi:10.1016/j.ymeth.2017.03.014 (2017).

125 Xie, X. S., Choi, P. J., Li, G.-W., Lee, N. K. & Lia, G. Single-Molecule Approach to Molecular Biology in Living Bacterial Cells. *Annual Review of Biophysics* **37**, 417-444, doi:10.1146/annurev.biophys.37.092607.174640 (2008).

126 Hulme, E. C. & Trevethick, M. A. Ligand binding assays at equilibrium: validation and interpretation. *British Journal of Pharmacology* **161**, 1219-1237, doi:10.1111/j.1476-5381.2009.00604.x (2010).

127 Grimm, J. B. *et al.* A General Method to Improve Fluorophores Using Deuterated Auxochromes. *JACS Au* **1**, 690-696, doi:10.1021/jacsau.1c00006 (2021).

128 Achimovich, A. M., Yan, T. & Gahlmann, A. *Dimerization of iLID Optogenetic Proteins Observed Using 3D Single-Molecule Tracking in Live Bacterial Cells* (bioRxiv, 2022).

129 Sieben, C., Banterle, N., Douglass, K. M., Gönczy, P. & Manley, S. Multicolor single-particle reconstruction of protein complexes. *Nature Methods* **15**, 777-780, doi:10.1038/s41592-018-0140-x (2018).

130 Magde, D., Elson, E. & Webb, W. W. Thermodynamic Fluctuations in a Reacting System—Measurement by Fluorescence Correlation Spectroscopy. *Phys. Rev. Lett.* **29**, 705-708, doi:10.1103/physrevlett.29.705 (1972).

131 Axelrod, D. K., D. E.; Schlessinger J.; Elson, E.; Webb, W.W. Mobility measurement by analysis of fluorescence photobleaching recovery kinetics. *Biophysical journal* **16**, 1055-1069, doi:https://doi.org/10.1016/S0006-3495(76)85755-4 (1976).

132 Koppel, D. E. A., D.; Schlessinger, J.; Elson, E. L.; Webb, W. W. . Dynamics of fluorescence marker concentration as a probe of mobility. *Biophysical journal* **16**, 1315-1329 (1976).

133 Wachsmuth, M. Molecular diffusion and binding analyzed with FRAP. *Protoplasma* **251**, 373-382, doi:10.1007/s00709-013-0604-x (2014).

134 Muller, K. P. *et al.* Multiscale analysis of dynamics and interactions of heterochromatin protein 1 by fluorescence fluctuation microscopy. *Biophysical journal* **97**, 2876-2885, doi:10.1016/j.bpj.2009.08.057 (2009).

135 Forster, T. Energiewanderung und fluoreszenz. *Naturwissenschaften* **33**, 166-175 (1946).

136 Elf, J. & Barkefors, I. Single-Molecule Kinetics in Living Cells. *Annual Review of Biochemistry* **88**, 635-659, doi:10.1146/annurev-biochem-013118-110801 (2019).

137 Karslake, J. D. *et al.* SMAUG: Analyzing single-molecule tracks with nonparametric Bayesian statistics. *Methods* **193**, 16-26, doi:10.1016/j.ymeth.2020.03.008 (2021).

138 Hansen, A. S. *et al.* Robust model-based analysis of single-particle tracking experiments with Spot-On. *Elife* **7**, doi:10.7554/eLife.33125 (2018).

139 Monnier, N. *et al.* Inferring transient particle transport dynamics in live cells. *Nat Methods* **12**, 838-840, doi:10.1038/nmeth.3483 (2015).

140 Michalet, X. & Berglund, A. J. Optimal diffusion coefficient estimation in single-particle tracking. *Physical Review E* **85**, doi:10.1103/PhysRevE.85.061916 (2012).

141 Au - Uphoff, S., Au - Sherratt, D. J. & Au - Kapanidis, A. N. Visualizing Protein-DNA Interactions in Live Bacterial Cells Using Photoactivated Single-molecule Tracking. *JoVE*, e51177, doi:doi:10.3791/51177 (2014).

142 Badrinarayanan, A., Reyes-Lamothe, R., Uphoff, S., Leake, M. C. & Sherratt, D. J. *In Vivo* Architecture and Action of Bacterial Structural Maintenance of Chromosome Proteins. *Science* **338**, 528-531, doi:10.1126/science.1227126 (2012).

143 Uphoff, S. *et al.* Stochastic activation of a DNA damage response causes cell-to-cell mutation rate variation. *Science* **351**, 1094-1097, doi:10.1126/science.aac9786 (2016).

144 Liao, Y., Schroeder, J. W., Gao, B., Simmons, L. A. & Biteen, J. S. Single-molecule motions and interactions in live cells reveal target search dynamics in mismatch repair. *Proc Natl Acad Sci U S A* **112**, E6898-6906, doi:10.1073/pnas.1507386112 (2015).

145 Liao, Y., Li, Y., Schroeder, J. W., Simmons, L. A. & Biteen, J. S. Single-Molecule DNA Polymerase Dynamics at a Bacterial Replisome in Live Cells. *Biophysical journal* **111**, 2562-2569, doi:10.1016/j.bpj.2016.11.006 (2016).

146 Calkins, A. L. *et al.* Independent Promoter Recognition by TcpP Precedes Cooperative Promoter Activation by TcpP and ToxR. *mBio* **12**, e0221321, doi:10.1128/mBio.02213-21 (2021).

147 Li, Y., Schroeder, J. W., Simmons, L. A. & Biteen, J. S. Visualizing bacterial DNA replication and repair with molecular resolution. *Curr Opin Microbiol* **43**, 38-45, doi:10.1016/j.mib.2017.11.009 (2017).

148 Li, Y., Chen, Z., Matthews, L. A., Simmons, L. A. & Biteen, J. S. Dynamic Exchange of Two Essential DNA Polymerases during Replication and after Fork Arrest. *Biophysical journal* **116**, 684-693, doi:10.1016/j.bpj.2019.01.008 (2019).

149 Peters, J. M. *et al.* A Comprehensive, CRISPR-based Functional Analysis of Essential Genes in Bacteria. *Cell* **165**, 1493-1506, doi:10.1016/j.cell.2016.05.003 (2016).

150 Ye, Y.-N., Hua, Z.-G., Huang, J., Rao, N. & Guo, F.-B. CEG: a database of essential gene clusters. *BMC Genomics* **14**, 769, doi:10.1186/1471-2164-14-769 (2013).

151 Robinson, M. S. & Hirst, J. Rapid inactivation of proteins by knocksideways. *Curr Protoc Cell Biol* **61**, 15 20 11-17, doi:10.1002/0471143030.cb1520s61 (2013).

152 Lindner, F., Gahlmann, A. & Diepold, A. Optogenetic control of protein translocation: Protein secretion and translocation into eukaryotic cells with high spatial and temporal resolution by light-controlled activation of the bacterial type III secretion system. European Patent Application 19166308 patent (2019).

153 De Geyter, J., Smets, D., Karamanou, S. & Economou, A. 337-366 (Springer International Publishing, 2019).

154 Cline, K. Mechanistic Aspects of Folded Protein Transport by the Twin Arginine Translocase (Tat). *Journal of Biological Chemistry* **290**, 16530-16538, doi:10.1074/jbc.r114.626820 (2015).

155 Wang, Z., Simoncelli, E. P. & Bovik, A. C. (IEEE, 2003).

156 Nijenhuis, W., Van Grinsven, M. M. P. & Kapitein, L. C. An optimized toolbox for the optogenetic control of intracellular transport. *J. Cell Biol.* **219**, doi:10.1083/jcb.201907149 (2020).

157 García-Fruitós, E. *et al.* Aggregation as bacterial inclusion bodies does not imply inactivation of enzymes and fluorescent proteins. *Microbial Cell Factories* **4**, 27, doi:10.1186/1475-2859-4-27 (2005).

158 Rinas, U. *et al.* Bacterial Inclusion Bodies: Discovering Their Better Half. *Trends in Biochemical Sciences* **42**, 726-737, doi:10.1016/j.tibs.2017.01.005 (2017).
159 Bartelt, S. M. *et al.* Dynamic blue light-switchable protein patterns on giant unilamellar vesicles. *Chemical communications* **54**, 948-951, doi:10.1039/c7cc08758f (2018).
160 Bartelt, S. M., Steinkühler, J., Dimova, R. & Wegner, S. V. Light-Guided Motility of a Minimal Synthetic Cell. *Nano Letters* **18**, 7268-7274, doi:10.1021/acs.nanolett.8b03469 (2018).
161 Lampe, A., Haucke, V., Sigrist, S. J., Heilemann, M. & Schmoranzer, J. Multi-colour direct STORM with red emitting carbocyanines. *Biology of the cell / under the auspices of the European Cell Biology Organization* **104**, 229-237, doi:10.1111/boc.201100011 (2012).
162 Loschberger, A. *et al.* Super-resolution imaging visualizes the eightfold symmetry of gp210 proteins around the nuclear pore complex and resolves the central channel with nanometer resolution. *Journal of Cell Science* **125**, 570-575, doi:10.1242/jcs.098822 (2012).
163 Sauer, M. & Heilemann, M. Single-Molecule Localization Microscopy in Eukaryotes. *Chem Rev*, doi:10.1021/acs.chemrev.6b00667 (2017).
164 Chen, F., Tillberg, P. W. & Boyden, E. S. Expansion microscopy. *Science* **347**, 543-548, doi:doi:10.1126/science.1260088 (2015).
165 Tillberg, P. W. *et al.* Protein-retention expansion microscopy of cells and tissues labeled using standard fluorescent proteins and antibodies. *Nat Biotechnol* **34**, 987-992, doi:10.1038/nbt.3625 (2016).
166 Zwettler, F. U. *et al.* Molecular resolution imaging by post-labeling expansion single-molecule localization microscopy (Ex-SMLM). *Nature communications* **11**, doi:10.1038/s41467-020-17086-8 (2020).
167 Balzarotti, F. *et al.* Nanometer resolution imaging and tracking of fluorescent molecules with minimal photon fluxes. *Science* **355**, 606-612, doi:10.1126/science.aak9913 (2017).
168 Kapadia, N., El-Hajj, Z. W. & Reyes-Lamothe, R. Bound2Learn: a machine learning approach for classification of DNA-bound proteins from single-molecule tracking experiments. *Nucleic Acids Research* **49**, e79-e79, doi:10.1093/nar/gkab186 (2021).
169 Muñoz-Gil, G., Garcia-March, M. A., Manzo, C., Martín-Guerrero, J. D. & Lewenstein, M. Single trajectory characterization via machine learning. *New Journal of Physics* **22**, 013010, doi:10.1088/1367-2630/ab6065 (2020).
170 Boyd, A. P., Lambermont, I. & Cornelis, G. R. Competition between the Yops of Yersinia enterocolitica for delivery into eukaryotic cells: Role of the SycE chaperone binding domain of YopE. *Journal of Bacteriology* **182**, 4811-4821, doi:10.1128/jb.182.17.4811-4821.2000 (2000).
171 Diepold, A. & Armitage, J. P. Type III secretion systems: the bacterial flagellum and the injectisome. *Philosophical transactions of the Royal Society of London. Series B, Biological sciences* **370**, doi:10.1098/rstb.2015.0020 (2015).
172 Costa, T. R. *et al.* Secretion systems in Gram-negative bacteria: structural and mechanistic insights. *Nat Rev Microbiol* **13**, 343-359, doi:10.1038/nrmicro3456 (2015).

173 Cornelis, G. R. The type III secretion injectisome. *Nat Rev Microbiol* **4**, 811-825, doi:10.1038/nrmicro1526 (2006).

174 Buttner, D. Protein export according to schedule: architecture, assembly, and regulation of type III secretion systems from plant- and animal-pathogenic bacteria. *Microbiology and molecular biology reviews : MMBR* **76**, 262-310, doi:10.1128/MMBR.05017-11 (2012).

175 Portaliou, A. G., Tsolis, K. C., Loos, M. S., Zorzini, V. & Economou, A. Type III Secretion: Building and Operating a Remarkable Nanomachine. *Trends Biochem Sci* **41**, 175-189, doi:10.1016/j.tibs.2015.09.005 (2016).

176 Ittig, S. J. *et al.* A bacterial type III secretion-based protein delivery tool for broad applications in cell biology. *The Journal of cell biology* **211**, 913-931, doi:10.1083/jcb.201502074 (2015).

177 Lara-Tejero, M., Kato, J., Wagner, S., Liu, X. & Galan, J. E. A Sorting Platform Determines the Order of Protein Secretion in Bacterial Type III Systems. *Science* **331**, 1188-1191, doi:10.1126/science.1201476 (2011).

178 Johnson, S. & Blocker, A. Characterization of soluble complexes of the Shigella flexneri type III secretion system ATPase. *FEMS microbiology letters* **286**, 274-278, doi:10.1111/j.1574-6968.2008.01284.x (2008).

179 Diepold, A. *et al.* A dynamic and adaptive network of cytosolic interactions governs protein export by the T3SS injectisome. *Nature communications* **8**, 15940, doi:10.1038/ncomms15940 (2017).

180 Diepold, A., Kudryashev, M., Delalez, N. J., Berry, R. M. & Armitage, J. P. Composition, formation, and regulation of the cytosolic c-ring, a dynamic component of the type III secretion injectisome. *PLoS Biol* **13**, e1002039, doi:10.1371/journal.pbio.1002039 (2015).

181 Lara-Tejero, M. The Type III Secretion System Sorting Platform. *Curr Top Microbiol Immunol*, doi:10.1007/82_2019_167 (2019).

182 Vollmer, W. in *Molecular Medical Microbiology (Second Edition)* (eds Yi-Wei Tang *et al.*) 105-124 (Academic Press, 2015).

183 Vollmer, W., Blanot, D. & de Pedro, M. A. Peptidoglycan structure and architecture. *Fems Microbiology Reviews* **32**, 149-167, doi:10.1111/j.1574-6976.2007.00094.x (2008).

184 Schleifer, K. H. & Kandler, O. Peptidoglycan types of bacterial cell walls and their taxonomic implications. *Bacteriological Reviews* **36**, 407-477, doi:doi:10.1128/br.36.4.407-477.1972 (1972).